EXAMINING THE GROWTH AND EVOLUTION OF MAGNETIC FIELDS IN CLUSTERS OF GALAXIES: A NUMERICAL PERSPECTIVE

BY

PAUL M. SUTTER

DISSERTATION

Submitted in partial fulfillment of the requirements
for the degree of Doctor of Philosophy in Physics
in the Graduate College of the
University of Illinois at Urbana-Champaign, 2011

Urbana, Illinois

Doctoral Committee:

Associate Professor Brian Fields, Chair
Associate Professor Paul M. Ricker, Director of Research
Professor Charles Gammie
Adjunct Professor Joseph Mohr

Abstract

Magnetic fields are ubiquitous in galaxy cluster atmospheres and have a variety of astrophysical and cosmological consequences. Magnetic fields can contribute to the pressure support of clusters, affect thermal conduction, and modify the evolution of bubbles driven by active galactic nuclei. However, we currently do not fully understand the origin and evolution of these fields throughout cosmic time. Furthermore, we do not have a general understanding of the relationship between magnetic field strength and topology and other cluster properties, such as mass and X-ray luminosity. We can now begin to answer some of these questions using large-scale cosmological magnetohydrodynamic (MHD) simulations of the formation of galaxy clusters including the seeding and growth of magnetic fields.

Using large-scale cosmological simulations with the FLASH code combined with a simplified model of the acceleration of cosmic rays responsible for the generation of radio halos, we find that the galaxy cluster frequency distribution and expected number counts of radio halos from upcoming low-frequency surveys are strongly dependent on the strength of magnetic fields. Thus, a more complete understanding of the origin and evolution of magnetic fields is necessary to understand and constrain models of diffuse synchrotron emission from clusters.

One favored model for generating magnetic fields is through the amplification of weak seed fields in active galactic nuclei (AGN) accretion disks and their subsequent injection into cluster atmospheres via AGN-driven jets and bubbles. However, current large-scale cosmological simulations cannot directly include the physical processes associated with the accretion and feedback processes of AGN or the seeding and merging of the associated SMBHs. Thus, we must include these effects as subgrid models. In order to carefully study the growth of magnetic fields in clusters via AGN-driven outflows, we present a systematic study of SMBH and AGN subgrid models. Using dark-matter only cosmological simulations, we find that many important quantities, such as the relationship between SMBH mass and galactic bulge velocity dispersion and the merger rate

of black holes, are highly sensitive to the subgrid model assumptions of SMBHs. In addition, using MHD calculations of an isolated cluster, we find that magnetic field strengths, extent, topology, and relationship to other gas quantities such as temperature and density are also highly dependent on the chosen model of accretion and feedback.

We use these systematic studies of SMBHs and AGN inform and constrain our choice of subgrid models, and we use those results to outline a fully cosmological MHD simulation to study the injection and growth of magnetic fields in clusters of galaxies. This simulation will be the first to study the birth and evolution of magnetic fields using a fully closed accretion-feedback cycle, with as few assumptions as possible and a clearer understanding of the effects of the various parameter choices.

To GB.

Acknowledgments

I am forever indebted to my advisor, Paul Ricker, for his instruction, friendship, and patient guidance.

I would like to thank the Krell Institute for their financial support via the DOE Computational Science Graduate Fellowship (DE-FG02-97ER25308) and their community of friends and colleagues.

The software used in this work was in part developed by the DOE-supported ASC/Alliance Center for Astrophysical Thermonuclear Flashes at the University of Chicago.

This research used resources of the National Center for Computational Sciences at Oak Ridge National Laboratory under the AST100, AST019, and AST026 Director's Discretionary allocations. The computing resources used are supported by the Office of Science of the US Department of Energy under contract no. DE-AC05-00OR22725. Additional computing resources were supplied by an allocation provided by the National Science Foundation (TG-AST040034N) on Kraken at the National Institute for Computational Sciences.

Both professionally and personally I would like to thank (in no particular order) James Lee, Hsiang-Yi (Karen) Yang, Anshu Dubey, Klaus Weide, Bronson Messer, Rebecca Hartman-Baker, Judy Hill, Tom Peterka, Alexander Knebe, Zarija Lukic, Dave Pugmire, Gary Foreman, Salman Habib, Katrin Heitman, Hao Xu, Hui Li, Dan Whalen, Ben Wandelt, Luke Olson, Greg Huey, Hal Finkel, and many many others for useful and interesting conversations, discussions, questions, critiques, tips, tweaks, edits, shortcuts, insights, ideas, help, reminders, directions, and comments.

I also gratefully thank my committee members: Brian Fields, Charles Gammie, and Joseph Mohr.

Of course, this process would have been much less bearable without the constant comfort and reassurances of my ever-patient and understanding wife, family, and friends.

Table of Contents

List of Tables

List of Figures

List of Abbreviations

AGN	Active galactic nuclei
AMR	Adaptive mesh refinement
BH	Black hole
BHAR	Black hole accretion rate
CDM	Cold dark matter
CMB	Cosmic microwave background
CR	Cosmic ray
HF	Halo finder
ICM	Intracluster medium
FOF	Friends-of-friends
LOFAR	LOw Frequency ARray
MHD	Magnetohydrodynamics
RM	Rotation measure
SKA	Square Kilometer Array
SO	Spherical overdensity
SPH	Smoothed-particle hydrodynamics
SMBH	Supermassive black hole

List of Symbols

a	Scale factor
$\mathbf{B}$	Magnetic field (vector)
h	Hubble parameter
Φ	Gravitational potential
ρ	Density
p	Pressure
$M_\odot$	Solar mass
T	Temperature
$\mathbf{v}$	Velocity (vector)
z	Redshift

Chapter 1

Introduction

1.1 The observed universe

Multiple independent lines of evidence, including fluctuations in the cosmic microwave background (e.g., Komatsu et al. 2011), the large-scale matter distribution (e.g., Percival et al. 2001), and distance measurements to Type Ia supernovae (Perlmutter et al. 1999; Riess et al. 1998), indicate that the universe arose from a hot, dense state roughly 13.7 billion years ago and is currently comprised of roughly 4% baryonic matter, 20% dark matter, which is most likely a form of massive, non-relativistic, weakly-interacting particles, and 70% dark energy, which drives the current accelerating expansion of the universe. Neutrinos and radiation make up the negligible remainder at the present day. Structures in the universe most likely arose from quantum mechanical random fluctuations in the vacuum that expanded to macroscopic scales during the inflationary epoch, a period in the early universe of rapid expansion (Guth 1981; Linde 1982; Albrecht et al. 1982). This basic model of our universe is known as the Concordance Model, or ΛCDM, for dark energy plus cold (i.e., non-relativistic) dark matter. A full discussion of this framework and the following derivations can be found in any cosmology textbook, such as Peebles (1993) and Peacock (1999).

We characterize the evolution of the universe via the Friedman-Lemaître-Robertson-Walker metric by assuming space is homogeneous and isotropic. An infinitesimal spacetime interval $d\tau$ in this metric is given by:

$$-c^2 d\tau^2 = -c^2 dt^2 + a(t)^2 d\Sigma^2, \tag{1.1}$$

where c is the speed of light, dt if an infinitesimal time interval, $d\Sigma$ is an infinitesimal distance element in a three-dimensional space of constant curvature, and $a(t)$ is the scale factor, which describes the expansion of space with time. We shall define the scale factor at the present day as $a_0 \equiv a(t_0) = 1$. Note that here and throughout this manuscript, a subscript of 0 will indicate present-day values, unless otherwise noted.

Using this metric in the Einstein field equations we may derive an equation for the expansion rate as a function of time in terms of the energy content of the universe:

$$\left(\frac{\dot{a}}{a}\right)^2 = H_0^2 \left(\frac{\Omega_{\mathrm{m},0}}{a^3} + \Omega_{\Lambda,0}\right). \tag{1.2}$$

Here we have assumed zero spatial curvature and a negligible contribution from radiation. If we define the Hubble parameter as $H \equiv \dot{a}(t)/a(t)$, then H_0 represents the present-day value of 70 km s^{-1} Mpc^{-1}. Here we have written the energy density of the universe in terms of the density parameters, namely

$$\begin{aligned} \Omega_{\mathrm{m}} &= \frac{\rho_{\mathrm{m}}}{\rho_{\mathrm{crit}}} \\ \Omega_{\Lambda} &= \frac{\rho_{\Lambda}}{\rho_{\mathrm{crit}}}, \end{aligned}$$

for matter and dark energy, respectively. These quantities are defined in terms of the critical density, ρ_{crit}, which is

$$\rho_{\mathrm{crit}} = \frac{3H^2}{8\pi G}, \tag{1.3}$$

where G is Newton's constant. A spatially flat (zero curvature) universe has a total density equal to $\rho_{\mathrm{crit}} = 1$. In this case, $\Omega_{\mathrm{m}} + \Omega_{\Lambda} = 1$.

For convenience we shall define several useful parameters, such as

$$h \equiv \frac{H_0}{70 \text{ km s}^{-1} \text{ Mpc}^{-1}}, \tag{1.4}$$

$h_{70} \equiv h/0.7$, and $h_{50} \equiv h/0.5$. Unless otherwise noted, quantities will be given in a reference frame comoving with the expansion of the universe in which the position vector $\mathbf{x}$ is given by

$$\mathbf{x} = \frac{\mathbf{r}}{a}, \tag{1.5}$$

where $\mathbf{r}$ is a proper position vector. Finally, the cosmological redshift is related to the scale factor by

$$z(t) = \frac{1}{1 + a(t)}. \tag{1.6}$$

1.2 Galaxy clusters: cosmology and astrophysics

This work will focus on clusters of galaxies. With masses in the range of $10^{14} - 10^{15}\ M_{\odot}$ and radii from $2 - 10$ Mpc, these are the largest gravitationally-bound objects in the universe (Voit 2005). In the ΛCDM paradigm, structure evolves in a hierarchical fashion with smaller objects accumulating to form larger ones that tend to form at the intersection of the rope-like structures known as filaments (Baugh 2006). Clusters of galaxies have formed relatively recently,

with the farthest known cluster at $z = 1.46$ (Collins et al. 2009), and they have only lately decoupled from the cosmic expansion. Thus, they offer especially important insights into the cosmos as a whole. In particular, they are potentially a key probe of dark energy (Albrecht et al. 2006). However, clusters are complex objects, and a detailed understanding of their astrophysical characteristics is necessary to enhance their usefulness in cosmology.

Simple hydrostatic equilibrium arguments based on the observed X-ray temperatures of clusters indicate that they consist primarily ($\sim$ 85%) of non-baryonic dark matter (e.g., see cluster surveys such as Bohringer et al. 2004). N-body simulations indicate that the dark matter in clusters follow a universal profile (Navarro et al. 1996):

$$\rho(r) = \frac{\rho_0}{r/R_s \left(1 + r/R_s\right)^2}, \tag{1.7}$$

where ρ_0 and R_s are scaling parameters which vary with each halo. The two asymptotic radial scalings ($\propto r^{-1}$ and $\propto r^{-3}$) result from the two stages of cluster growth: initial formation of the cluster and the steady slow accretion of material after it forms. While this relationship may not hold for recently-merged systems, it is in surprisingly good agreement with observations (Umetsu et al. 2011).

The remaining $\sim 15\%$ of the mass of galaxy clusters consists of the diffuse, hot ($> 10^7$ K) gas of the intracluster medium (ICM). This hot gas emits X-rays in the form of *bremsstrahlung* radiation. Observations of multiple clusters with instruments such as the Chandra X-ray Observatory (Weisskopf et al. 2002) indicate that the surface brightness profile $S(R)$ of most clusters follows the so-called β-model (Jones & Forman 1984):

$$S(R) = S_0 \left(1 + (R/r_c)^2\right)^{-3\beta+0.5}, \tag{1.8}$$

where r_c is the core radius of the observed profile. The parameter β is defined by

$$\beta \equiv \mu m_p \sigma^2 / kT, \tag{1.9}$$

where μ is the mean molecular weight, m_p is the proton mass, and σ and T are the velocity dispersion and temperature of the gas, respectively. The β-model assumes that clusters are isothermal and are in hydrostatic equilibrium. The X-ray temperature scales with cluster mass as a power law at temperatures below 1 keV (Reiprich & Boehringer 2002). The ICM can cool radiatively from atomic line emission; however, simple estimates of the amount of cooling predict cluster cores with temperatures far lower than observed (David et al. 2001). Also, cooling should be stronger in the higher-density cores, forcing gas to flow inwards, but again observations demonstrate that these cooling flows are far weaker than anticipated (Bohringer et al. 2002; Peterson et al. 2003). Several mechanisms have been proposed to heat the ICM, including feedback

from active galactic nuclei (AGN) (McNamara & Nulsen 2007) and sloshing of material after mergers (e.g., ZuHone et al. 2010).

Visible galaxies make up only an almost-negligible fraction ($\sim$ 5%) of a cluster's mass (Zwicky 1933; Bahcall 1977). However, they may contribute to the turbulence of the ICM due to their wakes as the move about inside a cluster (Subramanian et al. 2006; Kim 2007), and outflows driven by supernovae contribute metals to the cluster atmosphere (Schindler et al. 2005; Kapferer et al. 2006) and possibly magnetic fields (Bertone et al. 2006).

The key cluster quantity used for cosmological purposes is the total cluster mass. The frequency distribution of clusters as a function of mass, known as the mass function, is sensitive to several cosmological parameters, including the total matter fraction of the universe $\Omega_{\rm m}$, the the variance of matter density within a sphere of 8 h^{-1} Mpc (σ_8), and the properties of dark energy (White 2002). For a given cosmology, Press & Schechter (1974) derived an analytical expression for the mass function, and this mass function is in broad agreement with mass functions derived from large-scale cosmological simulations (White 2002).

Future surveys such as the Dark Energy Survey will extend these observations to higher redshift and larger volumes (Annis et al. 2005). However, since most of the cluster mass resides in the form of invisible dark matter, the determination of mass is highly sensitive to the underlying cluster astrophysics. Numerous techniques have been developed to relate cluster mass to observables, such as estimates derived from hydrostatic equilibrium (Evrard et al. 1996; Vikhlinin et al. 2009), and there are efforts underway to directly measure the mass of many clusters using weak (Bartelmann & Schneider 2001; Scoville et al. 2007) and strong gravitational lensing (Bartelmann 2003).

1.3 Magnetic fields in clusters

1.3.1 Observational evidence

Diffuse radio sources

Radio observations (10 MHz - 1.4 GHz) of many clusters reveal diffuse, large-scale synchrotron sources not associated with individual galaxies (e.g., Brunetti et al. 2008). These sources are divided into three categories: giant radio halos, radio relics, and radio mini-halos. Examples of these three types of sources are shown in Figure 1.3.1. To generate these radio features, nonthermal high-energy electrons ("cosmic rays") must either be injected into the ICM and accelerated (Jaffe 1977) or produced as secondary particles in proton-proton collisions (Dennison 1980). Regardless of their origins, the cosmic rays which produce the synchrotron emission require the presence of large-scale magnetic fields within the cluster atmosphere. These magnetic fields have a complex relationship with the turbulent properties of the ICM. Gas flows within galaxy

clusters are mildly supersonic, with Mach numbers $M < 10$, while accretion shocks outside clusters can have $M > 10^3$ (Miniati 2003; Ryu et al. 2003; Skillman et al. 2008). The plasma beta parameter (ratio of gas to magnetic pressure) in the ICM is typically > 1.

Giant radio halos are ∼Mpc-scale features with steep (spectral index $\alpha \sim 1.2$) radio spectra not associated with any individual galaxy (Schlickeiser et al. 1987). Radio halos are relatively rare: they are only associated with about one third of the most massive halos ($> 10^{15}$ $M_\odot$) (Feretti et al. 2004). Additionally, they are only associated with merging clusters (Brunetti et al. 2009). First discovered over 60 years ago (Large et al. 1959), by the present day only a few dozen radio halos are known (Cassano et al. 2006). The radio powers of these halos are tightly correlated with cluster X-ray luminosity (e.g., Liang et al. 2000; Bacchi et al. 2003; Cassano et al. 2007). Assuming equipartition between magnetic field energy density and the energy of cosmic rays leads to an estimate for cluster magnetic field strengths of $0.1-1\mu$G (Carilli & Taylor 2002; Pfrommer & Enß lin 2004). In order to power these giant halos, the magnetic fields must be present throughout the entire cluster atmosphere.

Radio relics are elongated, strongly polarized radio structures found on the periphery of clusters. Due to their low surface brightness, they are only known in roughly two dozen clusters (Ferrari et al. 2008). Like giant halos, they are not associated with any individual galaxies. These sources most likely originate from shock fronts associated with recent cluster mergers: as the shock front brakes at the edge of the cluster gravitational potential, cosmic rays are accelerated via first-order Fermi processes, producing the synchrotron emission (Enß lin et al. 1998; Giacintucci et al. 2008). Some observed clusters host both halos and relics, indicating separate mechanisms for their generation (Brown et al. 2011). Estimates of the magnetic field required to produce these features range from $0.4 - 2.7$ μG (Enß lin et al. 1998).

Radio mini-halos show characteristics similar to giant halos, but as their name implies, they only extend throughout the cores of clusters (Keshet & Loeb 2010). Unlike the giant halos, which are connected to recently-merged and therefore highly turbulent massive clusters, mini-halos are linked to relaxed, cool-core clusters (Gitti et al. 2002). Magnetic field estimates from these observations range from $0.5-5$ μG in the cores of these clusters (Keshet & Loeb 2010; Bonafede et al. 2011).

Rotation measure

As polarized light passes through a magnetized plasma it will experience different indices of refraction for different axes depending on the local orientation of the magnetic field. If the light from a background source passes through a length L of the ICM, its plane of polarization will rotate by $\Delta\chi = \mathrm{RM}\ \lambda^2$, where λ is the wavelength and RM is the integrated net effect of the magnetic field,

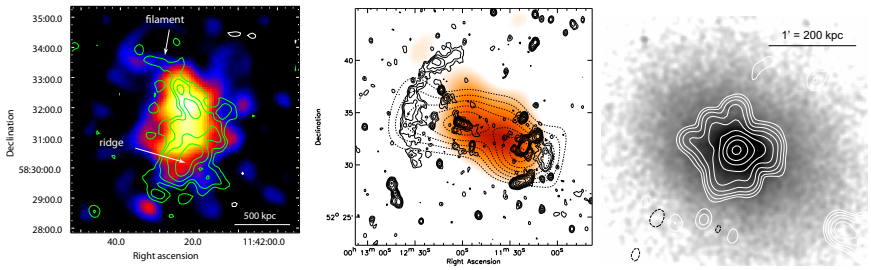

(a) (b) (c)

Figure 1.1: Various radio observations (contours) overlaid on X-ray images. Shown are a) the giant radio halo of Abell 521 (Giacintucci et al. 2008), b) the radio relic of ZwCl 0008.8+5215 (van Weeren et al. 2011), and c) the radio mini-halo of RXCJ 1504.10248 (Venturi et al. 2011).

the rotation measure:

$$\mathrm{RM} = 812 \int_0^L n_e \mathbf{B} \cdot d\mathbf{l} \text{ radians m}^{-2}. \tag{1.10}$$

In the above equation, $\mathbf{B}$ is the magnetic field in μG, n_e is the electron density, and $\mathbf{l}$ is the direction of propagation in kpc.

We can measure the RM of a portion of a cluster's atmosphere by using multifrequency radio observations of polarized background sources behind clusters compared to observations of similar sources with radiation that does not pass through clusters (Simard-Normandin et al. 1981; Clarke et al. 2001). Some clusters, such as Cygnus A (shown in Figure 1.3.1) , have lobe and jet structures that are thoroughly mapped. Due to the nature of the RM, we can only estimate the portion of the magnetic field along the line of sight. Given these constraints and assumptions about the underlying electron densities, RM measurements indicate magnetic fields of strengths $1-5$ μG, with those in some cool cores up to $10-20$ μG (Carilli & Taylor 2002). Note that these derived magnetic fields are much stronger than those estimated from diffuse radio emissions, and this inconsistency is not fully understood. Additionally, there is some evidence of a relationship between rotation measure strength and the cooling flow rate near the centers of relaxed clusters (Feretti et al. 1999).

Since RM measurements are based on observations of multiple point sources, we can use these to determine the spatial distribution and characteristics of the magnetic fields. The fields do not appear to be ordered, but are randomly tangled with auto-correlation lengths of $5-20$ kpc, with some large ($\sim$ 100kpc) structures found near cluster cores (e.g., Dreher et al. 1987). Also, some clusters exhibit "bands" of alternating high- and low-rotation measure, indicating some radial dependence on the magnetic field strength and topology (Taylor & Perley 1993). Simulations used to reproduce observed clusters indicate rich magnetic topology: filaments, loops, and multiple entanglements (Falceta-Gonçalves et al. 2010b). RM observations have also demonstrated that although most clusters to

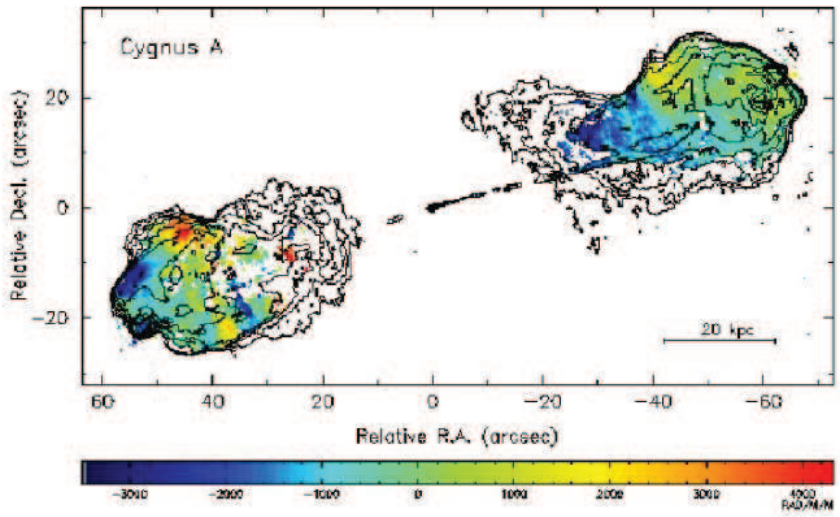

Figure 1.2: Rotation measure observations of Cygnus A (adapted from Dreher et al. 1987).

do not host a radio halo, all clusters observed with RM do contain cluster-wide magnetic fields.

1.3.2 Roles in cluster physics

The presence of magnetic fields has a variety of consequences for the ongoing astrophysical processes operating in the cluster atmosphere. Simply the presence of magnetic fields adds a source of non-thermal pressure support. This support is highly variable: up to $\sim 20\%$ in some clusters but negligible in others (Dolag & Schindler 2000). Also, as we have seen above, the presence of magnetic fields allows the production of high energy protons and electrons in outflow- and merger-driven shocks. This nonthermal particle population, besides producing radio synchrotron emission, provides an additional source of pressure support (Miniati et al. 2001; Pfrommer et al. 2007; Skillman et al. 2008; Brunetti et al. 2007).

Magnetic fields can also modify the transport properties of the ICM, making them key to the unsettled question of the level of turbulence in the intracluster medium (Shukurov et al. 2006). Tangled magnetic fields on scales $\ll 1$ kpc should suppress the free streaming of thermal electrons, which would otherwise have a Coulomb mean free path of several kpc (Sarazin 1988). However, recent theoretical work on electron transport in low-density plasmas suggests that the degree of suppression depends on the magnetic field topology and may be much smaller (e.g., Narayan & Medvedev 2001; Chandran & Maron 2004). The same mechanism may allow protons to diffusively transport momentum, giving rise to viscosity, which would suppress the development of ICM turbulence.

One possible way to suppress the extreme cooling of cluster cores is through thermal conduction (Bregman & David 1988). However, there is a strong interconnection between cooling flows and magnetic fields. For example, turbulence due to galaxy mixing can stir and randomize fields, and these randomized fields may suppress conduction (Ruszkowski & Oh 2010). Heat-flux-driven buoyancy instability can re-arrange magnetic fields to be perpendicular to the temperature gradient, suppressing thermal conduction (Parrish et al. 2009), but it takes of order a dynamical time for the fields to re-arrange, and significant heating of the core may take place in the meantime (Bogdanović et al. 2009). However, strong enough convection may in turn suppress the impact of magnetic fields (Mikellides et al. 2011). Thus, the role of heat conduction in the ICM is heavily dependent upon the strength, radial dependence, and topological configuration of magnetic fields.

High-resolution X-ray observations of nearby cold core clusters show that AGN can play a significant role in disturbing and heating the ICM (e.g., McNamara et al. 2000). The magnetized, relativistic jets produced by these AGN propagate out into the ICM, where they slow and reach approximate pressure equilibrium. Their subsequent evolution as "bubbles" appears to be driven by the buoyancy of the relativistic plasma they contain. Simulations of magnetically supported AGN bubbles (Robinson et al. 2004; Jones & De Young 2005; Ruszkowski et al. 2007; Xu et al. 2008a; Gourgouliatos et al. 2010) show that magnetic fields can prevent the development of instabilities that would otherwise destroy these bubbles before they rise more than a few times 10 kpc; thus the location at which these bubbles deposit their energy is sensitive to the strength and configuration of the magnetic field.

1.3.3 Implications for cosmology & future observations

Cosmological constraints based on galaxy clusters rely on the statistics of their positions, masses, and gas fractions. It is therefore necessary to accurately infer these properties from cluster observations. Because magnetic fields play such an important role in distributing gas and nonthermal particles throughout a cluster, they affect the linkage between X-ray and microwave (and to a lesser extent optical) observables and the gas mass (Dolag & Schindler 2000). They also play a direct role in producing diffuse radio emission. Several large cluster surveys, such as the Dark Energy Survey, in different wavebands now aim to measure these properties with very high precision in order to constrain the properties of dark energy (Annis et al. 2005). An improved understanding of the origin and development of cluster magnetic fields will be crucial to this undertaking.

Upcoming surveys, such as the LO Frequency ARray (LOFAR) (Rottgering 2003), the Extended Very Large Array (EVLSA) (Dougherty & Perley 2011), and the Square Kilometer Array (SKA) and its precurser the Australian SKA

Pathfinder (ASKAP) (Krause et al. 2009) will examine many currently unanswered questions about magnetic fields: when they first form, where they dominate, and how they relate to other cluster properties. Detailed RM observations will provide a wealth of new data on the configurations of magnetic fields within clusters (Beck 2009). This wealth of data can only be fully understood through analytical and numerical studies, and only by combining these approaches can we gain a full understanding of magnetic fields and the roles they play. In Chapter 2 we will more closely examine the link between cluster magnetic fields and radio halo properties and the consequences for future observational missions.

1.3.4 Potential origins

Since magnetic fields appear to be ubiquitous throughout the universe at a variety of scales and detections via large RM measurements indicate the presence of magnetic fields at redshift $z = 2$ (Athreya et al. 1998), it is natural to suppose a primordial, cosmological origin for them. However, the production of magnetic fields in the early universe usually requires exotic processes; some proposed mechanisms include turbulence by bubbles during the electroweak phase transition (Baym et al. 1996), electromagnetic processes during inflation (Bamba et al. 2008), turbulence due to cosmic strings (Battefeld et al. 2008), and formation during the preheating phase of electroweak symmetry breaking (Díaz-Gil et al. 2008).

However, strong magnetic fields in the early universe have many observational consequences. They can distort the locations of acoustic peaks in the CMB (Adams 1996), alter the production of light elements during the era of Big Bang Nucleosynthesis (Grasso & Rubinstein 1995), and affect the polarization of the CMB (Giovannini 2009). From these observations, magnetic fields in the early universe must be weaker than a nanogauss (Barrow et al. 1997; Blasi et al. 1999). Also, it may be difficult to sustain magnetic fields during the radiation-dominated era due to very high diffusion rates (Lesch & Birk 1998).

These constraints and limitations combined with the exotic nature of the underlying generation mechanisms motivate models based on relatively recent (i.e., post-recombination) astrophysical processes. Here, weak fields are generated at small scales and amplified and ejected into the surrounding medium. Again, many processes have been proposed, but most involve shock fronts propagating during the era of reionization. One scenario for the origin of magnetic fields in the ICM is the Biermann battery mechanism, whereby seed fields of strength $\sim 10^{-18}$ G are produced by baroclinic terms in the induction equation at oblique shocks (Biermann 1950; Widrow 2002). An alternative mechanism involves the Weibel Instability (Medvedev et al. 2006). Simulations of the battery mechanism have confirmed the ability of the first generation of stars to magnetize the surrounding medium to $10^{-18} - 10^{-12}$ G (Gnedin et al. 2000; Langer et al. 2005; Xu et al. 2008b).

Whether the seed fields arise during the early universe or during its later evolution, the produced seed fields are very weak and must be amplified to the observed values in clusters. However, the alternative hypotheses may be distinguishable by studying the filamentary structure between clusters: since early-universe mechanisms will magnetize the universe prior to substantial structure formation, the magnetic fields will be distributed over all structures with $\rho^{2/3}$ scaling, whereas dynamo-based magnetic fields will follow the evolution of gravitationally bound structures (Ryu et al. 1998; Brüggen et al. 2005), and hence these fields may not be present in more diffusive structures and be much stronger than expected in cluster cores.

These weak fields can be amplified and extended by a variety of mechanisms in clusters. Some stretching and amplification can be achieved during cluster mergers (Roettiger et al. 1999; Dolag et al. 2002; Takizawa 2008). Figure 1.3.4 illustrates this by showing the amplification of magnetic fields due to structure formation effects as a function of density. Also, amplification via gravitational collapse can be stronger than expected from adiabatic arguments because of the anisotropic nature of the collapse (King & Coles 2005). Even so, it is difficult to explain the presence of μG fields within the entire cluster volume (Dolag et al. 2006). Dynamo processes operating in the ICM can amplify and sustain the cluster magnetic fields (Xu et al. 2009; Ruzmaikin et al. 1989). Turbulence from AGN can amplify fields in cores (Dubois & Teyssier 2008) and galaxy motions can amplify fields in the outer cluster atmosphere (Subramanian et al. 2006). These processes can easily amplify a somewhat weaker field ($\sim 10^{-9}$ G) to the observed values.

However, the above cluster-scale processes require pre-existing fields in smaller groups and galaxies. There is still a significant gap between the predicted seed fields ($\sim 10^{-18}$ G) and the fields required to participate in cluster-scale processes ($\sim 10^{-12} - 10^{-9}$ G). Dynamo processes must be invoked to significantly amplify the fields to the observed values. While galactic disks can act as $\alpha - \Omega$ dynamos (Kulsrud & Zweibel 2008), to achieve the measured field strengths the dynamo must operate with a much shorter characteristic timescale.

Due to their short dynamical timescales and frequent occurrence, stars are one of the most promising dynamo sources (Rees 1987). However, by themselves stellar dynamos cannot produce the kpc-scale correlations seen in the ICM magnetic field. The magnetic fields generated in stars must be expelled into the ICM, and it is much more difficult to include these processes in the cosmological simulations that we will invoke in this work. Many mechanisms are available, including galactic winds (Donnert et al. 2009), quasar outflows (Furlanetto & Loeb 2001), and bubbles blown by active galactic nuclei (Liu et al. 2008b,a). AGN are accretion disk and jet systems associated with the supermassive black holes found in galaxy centers (Osterbrock 1989). AGN are especially attractive since they expel more than enough energy to magnetize the cluster volume (10^{61} ergs) (Colgate & Li 2000) and the jets which power the bubbles are nat-

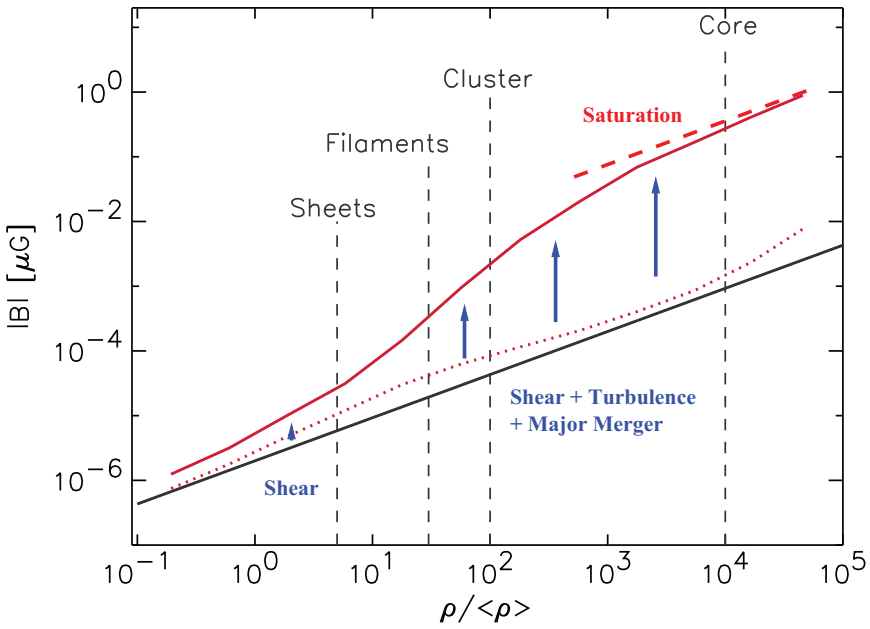

Figure 1.3: Amplification of magnetic fields due to structure formation (adapted from Dolag et al. (2006)). Shown is the strength of magnetic fields versus overdensity. The black line represents pure adiabatic compression, while the red line shows the effects of the indicated cluster processes.

ural carriers of magnetic flux (Daly & Loeb 1990). Indeed, RM observations detect strong magnetic fields in AGN-driven jets (Contopoulos et al. 2009).

1.4 Active galactic nuclei

Since active galactic nuclei may play such an important role in the growth and evolution of magnetic fields in clusters, we will discuss them in more detail.

It is thought that every galaxy may a supermassive black hole (SMBH) at its center (Ho 1999). These black holes have masses at least $10^6\ M_\odot$. As gas accretes onto the black hole, dynamo actions create a strong magnetic field (Khanna & Camenzind 1996), and these fields can launch magnetically-collimated jets (Koide et al. 1999). These jets are extremely powerful, up to 10^{61} ergs (e.g., Abdo & Collaboration 2010), and can extend up to several kpc out of the host galaxy and into the intracluster medium (Colbert et al. 1996). These systems of accretion disks and jet feedback are known as active galactic nuclei (AGN).

AGN activity is observed at very high redshift (Fan 2006) and is strongly associated with galaxy merging activity (Hopkins et al. 2005a). The strength of AGN ejections is thought to be regulated by feedback mechanisms: as the gas in cluster cores cools via atomic line emission and accretes onto the central

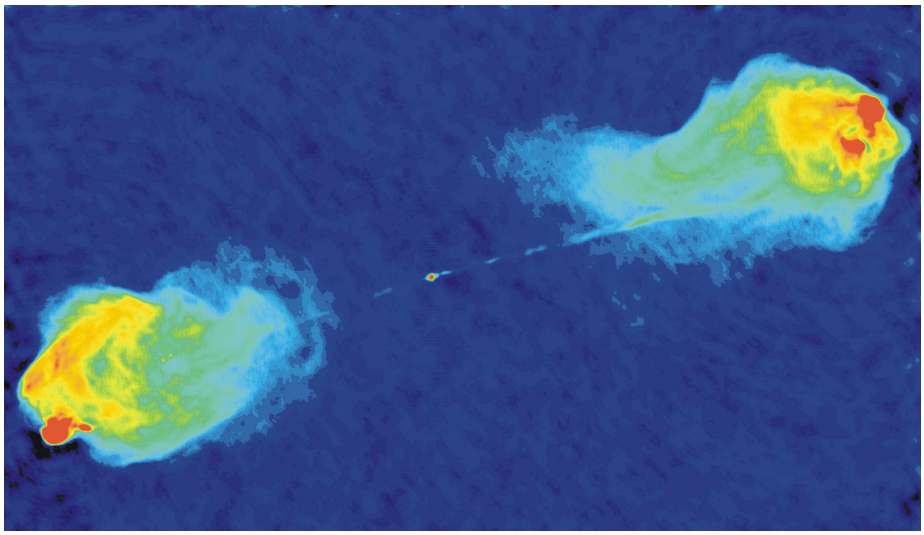

Figure 1.4: An AGN-blown bubble (Perley et al. 1984).

SMBH, it can trigger a strong ejection episode, which heats the ICM gas and drives it away from the core, thereby lowering the accretion rate and reducing the strength of any outflowing jets (e.g., Somerville et al. 2008). The process can then repeat, but the duty cycles of such activity are not well constrained (e.g., Dunn & Fabian 2006; Ciotti & Ostriker 2007). Note that as much as 90% of the present-day mass of SMBHs is due to gas accretion (Hopkins et al. 2006). The accretion rate $\dot{M}$ remains relatively strong; to account for present day masses the rate needs to be close to the Eddington limit (Kollmeier et al. 2006).

This AGN-driven feedback is considered a strong candidate to solve the cooling catastrophe problem described above (McNamara & Nulsen 2007). As Figure 1.4 shows, jets can inflate large ($\sim$ 100 kpc) bubbles which rise into the ICM and eventually disperse (Voit & Donahue 2005), distributing heat throughout the cluster core to several hundred kpc (Mittal et al. 2009). Also, self-regulating mechanisms are the only known way of producing the known relation between SMBH mass and galaxy bulge velocity dispersion (Gültekin et al. 2009).

1.5 Simulating the origins of magnetic fields

In order to accurately study the above scenarios in a truly cosmological context, we must turn to numerical simulation. We must evolve the underlying dark matter as large-scale structure develops. We must solve for the magnetic fields and the hydrodynamics of the intracluster medium. In addition, we must include the mechanisms for generating and sustaining magnetic fields for the chosen model. In order to capture the relationship between magnetic fields and other cluster properties, we must simulate large cosmological volumes at high

resolution. Below, we will discuss the ingredients necessary to perform these simulations and various approaches taken, followed by a general description of our simulation code, FLASH.

1.5.1 Dark matter

The most basic component of any cosmological simulation is the dark matter. Since the dark matter can be treated as a pressureless fluid, simulations typically sample some portion of its phase space and solve for its Newtonian equation of motion in an expanding universe (Bertschinger 1998):

$$\dot{\mathbf{v}} + 2\frac{\dot{a}}{a}\mathbf{v} = -\nabla\mathbf{\Phi}, \tag{1.11}$$

where $\mathbf{v}$ is the peculiar comoving velocity, a is the scale factor, and Φ is the gravitational potential. Particle positions are typically updated using a second-order accurate integration scheme (Efstathiou et al. 1985). To calculate the forces, simulations either employ some variant of a Barnes-Hut tree algorithm, where particles are grouped by distance and these groups are used to calculate average forces over large distance (Barnes & Hut 1989), or a particle-mesh algorithm, where the particles are mapped to a mesh to calculate their densities, the Poisson equation

$$\nabla^2\phi = \frac{4\pi G}{a^3}(\rho - \bar{\rho}) \tag{1.12}$$

(where ϕ is the comoving gravitational potential, a is the scale factor, ρ is the comoving matter density, and $\bar{\rho}$ is the mean comoving matter density) is solved, and the resulting accelerations are mapped back onto the particles (Hockney & Eastwood 1988).

The dark matter particles are typically initialized on a uniform grid and given small position and velocity perturbations. These perturbations come from linear perturbation theory. The observed CMB temperature fluctuations provide the power spectrum $P(k)$ of density fluctuations, e.g. using CMBFAST (Seljak & Zaldarriaga 1996). These are then translated to the initial redshift of the simulation using Lagrangian perturbation theory, most commonly the Zel'dovich approximation (Zel'Dovich 1970; Efstathiou et al. 1985).

While simply solving the equations of motion for dark matter traces its evolution, we must apply some simple analysis to identify structures (e.g., galaxies, groups, and clusters). For this we turn to "halo finders," which identify the "halos" of dark matter that envelope structures in the universe. In theory, all halo finders attempt to solve the same problem – identify all the gravitationally-bound structures in a given volume, but the implementations vary widely. Some codes, based on friends-of-friends (FOF) algorithms, build linked lists of particles within a set distance of each other, while others find local spherically-overdense (SO) regions which represent gravitationally-bound, virialized objects. Fortunately, as Figure 1.5.1 shows, a recent comparison of over 15 different

halo finders found remarkable agreement in determining many cosmologically-relevant statistics, including the mass function (Knebe et al. 2011).

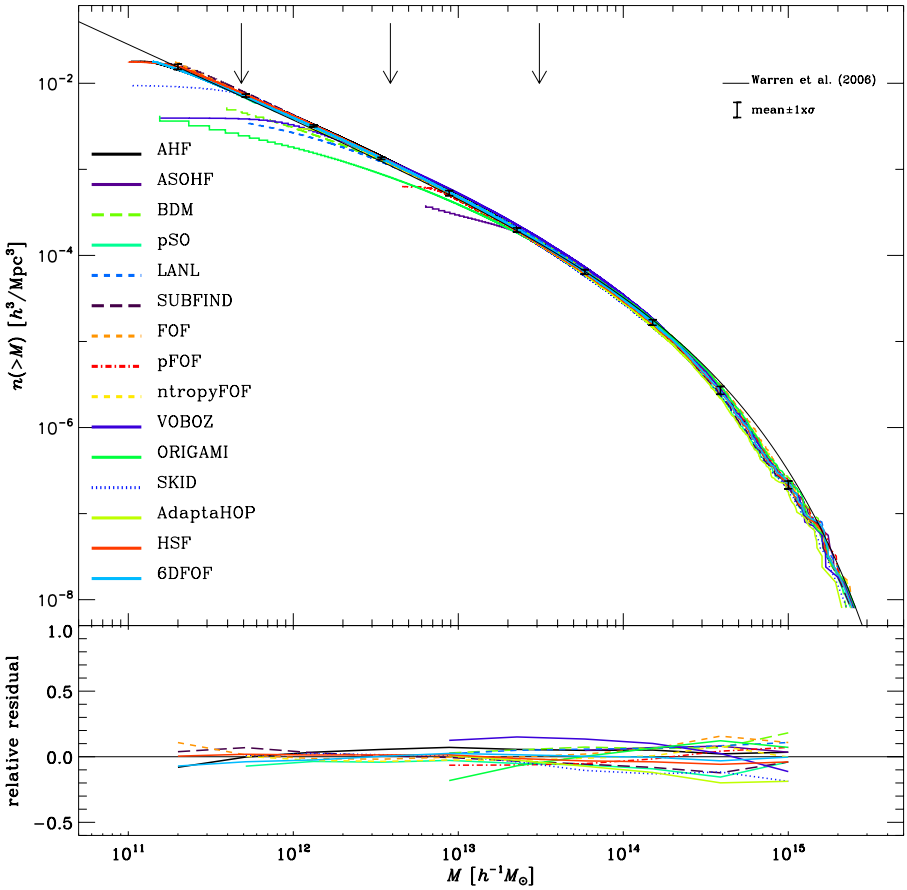

Figure 1.5: Comparison of halo finders using the mass function (adapted from Knebe et al. 2011). Results are compared against the fit of Warren et al. (2006).

1.5.2 Magnetohydrodynamics

While dark matter-only simulations are used in a variety of contexts and can be used to study many cosmological problems, they do have several deficiencies. Most immediately, it is impossible to predict observable cluster features, such as X-ray luminosity, without the presence of gas. More subtly, simulations with only dark matter predict cluster core density profiles that are very steep (Fukushige & Makino 1997; Diemand et al. 2005), in contrast to the observed smoother cores (e.g., Dahle et al. 2003), and tend to produce too many satellite structures (Moore et al. 1999). Thus, we must include gas in cosmological simulations. Of course, if we are to trace the evolution of magnetic fields, we must include those magnetic fields in the equations.

We will solve the equations for magnetohydrodynamics (MHD):

$$\frac{\partial \rho}{\partial t} + \frac{1}{a}\nabla \cdot (\rho \mathbf{v}) = 0 \tag{1.13}$$

$$\frac{\partial \rho \mathbf{v}}{\partial t} + \frac{1}{a}\nabla \cdot (\rho \mathbf{v}\mathbf{v} + \bar{p} - \mathbf{B}\mathbf{B}) = -\frac{\dot{a}}{a}\rho \mathbf{v} - \frac{1}{a}\rho \nabla \Phi \tag{1.14}$$

$$\frac{\partial E}{\partial t} + \frac{1}{a}\nabla \cdot [\mathbf{v}(\bar{p} + E) - \mathbf{B}(\mathbf{B} \cdot \mathbf{v})] = -\frac{\dot{a}}{a}\left(\rho v^2 + 3p + \frac{B^2}{2}\right) - \frac{\rho}{a}\mathbf{v} \cdot \nabla \Phi \tag{1.15}$$

$$\frac{\partial \mathbf{B}}{\partial t} - \frac{1}{a}\nabla \times (\mathbf{v} \times \mathbf{B}) = -\frac{\dot{a}}{2a}\mathbf{B}, \tag{1.16}$$

where

$$E = \frac{1}{2}\rho v^2 + \frac{p}{\gamma - 1} + \frac{1}{2}B^2 \tag{1.17}$$

$$\bar{p} = p + \frac{1}{2}B^2. \tag{1.18}$$

These equations are given in a comoving frame assuming an adiabatic equation of state with $\gamma = 5/3$, where a is the scale factor, $\mathbf{v}$ is the peculiar gas velocity, $\mathbf{B}$ is the magnetic field, p is the pressure, ρ is the density, and Φ is the gravitational potential. Note that these are all comoving quantities. There are many challenges to solving these equations numerically, such as identifying shocks and maintaining zero divergences in the magnetic field.

Strategies for solving these equations are as numerous as those for solving the dark matter, but as before there are two broad approaches: Lagrangian- and Eulerian-based schemes. Lagrangian, such as Smoothed-Particle Hydrodynamic (SPH), codes track fluid elements with individual particles (Lucy 1977). To calculate densities in SPH schemes, particles are spread out with some smoothing kernel W:

$$\rho_b(\mathbf{x}) = \sum_{i=1}^{N} m_i W\left(\mathbf{x} - \mathbf{x}_i, h\right), \tag{1.19}$$

where h is a smoothing length, W is a smooth window function, and m_i and $\mathbf{x}_i$ are particle masses and positions. As a result, each particle samples the local gas quantities. This allows SPH algorithms to easily sample high-density regions without excessive computational resources, at the cost of lower shock resolution and the inability to appropriate mix gas (Kang et al. 1994).

The most popular SPH code, Gadget-2, has been modified to include magnetic fields (Dolag & Stasyszyn 2008), but SPH codes in general have difficulty representing these fields due to "clumping" effects - if a particular SPH particle carries a strong magnetic field, it will tend to draw nearby particles to it, which spreads that strong field to the other particles, which draws in more particles, and this process continues and leads to catastrophe (Dolag & Stasyszyn 2008). Magnetized SPH codes thereby must include some correction factors to prevent this unphysical behavior, which is purely a consequence of the Lagrangian formalism. Also, there is no guarantee that the magnetic field is divergence-free.

Eulerian-based approaches divide the computational domain into a grid with each zone representing a portion of the volume. Gas can move in and out of each zone, and solutions are updated by calculating fluxes at the cell boundaries (Ritchmyer & Morton 1967). This strategy allows the codes to follow shocks as they form and propagate (e.g., Ryu et al. 1993). In order to achieve high spatial resolution without overwhelming computational resources, adaptive mesh refinement (AMR) allows multiple levels of grids to be applied to regions of interest (Anninos et al. 1994). Many popular AMR-Eulerian codes now include MHD solvers, including FLASH (Fryxell et al. 2000; Dubey et al. 2008), Enzo (Collins et al. 2010), and RAMSES (Teyssier 2002).

As with SPH codes, AMR solutions to the MHD equations must maintain zero divergence in B. Fortunately, there are several techniques available. The simplest techniques simply clean any divergences after the evolution step (e.g., Brackbill & Barnes 1980), while more sophisticated approaches explicitly maintain zero divergence (at least, to machine precision) throughout the calculation (e.g., Hawley & Stone 1995).

There have been several attempts to systematically compare SPH and AMR techniques. The study of Heitmann et al. (2008) found excellent agreement among many codes when simulating only dark matter. However, Frenk et al. (1999) applied multiple codes to the study of a single cluster and found $\sim 10\%$ agreement among estimates of cluster temperature, whereas X-ray luminosities varied by a factor of 2 (note that this was primarily due to differences in the central entropy profile). Similarly, Mitchell et al. (2009) found significant differences among codes in the study of merging clusters. Here the differences were mainly due to SPH codes suppressing eddies and vortices. Additionally, Agertz et al. (2007) found that AMR codes were much better able to handle shocks and instabilities in realistic astrophysical scenarios. Despite these differences, there is still strong qualitative agreement between the two approaches.

1.5.3 Subgrid models of active galactic nuclei

The physics of AGN systems is incredibly rich: general relativity, radiation, gas, and magnetic fields all play important dynamical roles. Additionally, accretion disks and the initial launching of jets occur on scales (~ 100 AU) below which we can typically resolve in cosmological (> 2 kpc), and even individual cluster ($\sim 0.5 - 4$ kpc), simulations. Thus, we must build "subgrid" or sub-resolution models that link the gas quantities in those simulations (i.e., temperature and sound speed) to an assumed model of the behavior of the AGN.

The first model assumption deals with the accretion rate. While the Bondi accretion rate (Bondi 1952),

$$\dot{M}_{\rm Bondi} = 4\pi G^2 m_{\rm BH}^2 \rho / {c_{\rm s}}^3, \tag{1.20}$$

where $c_{\rm s}$ is the sound speed, ρ is the gas density, and $m_{\rm BH}$ is the black hole mass,

is generally accurate for observed clusters (Allen et al. 2006), the measurements of v_s and ρ in simulations may underestimate the true accretion rate near the SMBH in most clusters and at lower resolutions. Thus, most authors typically "boost" the estimate Bondi rate by a fixed multiple – typically by a factor of 100 to 300 (e.g., Sijacki et al. 2007). An alternative method proposed by Booth & Schaye (2009) attempts to alleviate the arbitrary nature of this parameterization by scaling the accretion rate with the local density. However, since the accretion rate may be highly variable (King et al. 2004), perhaps more stochastic models, such as those proposed by Pope (2007), may be required.

Next, the feedback applied to the cluster atmosphere must be modeled. Subgrid models generally take one of two approaches: either attempting to simulate the large-scale jet outflows or by placing already-formed bubbles. Typically, jet models require higher resolution, and the jets are not guaranteed to reproduce observed cavity morphology. Bubbles, since they are much larger than jets, can be implemented with much less resolution, but the models must be more tuned than jets in order to generate realistic-looking bubbles.

A variety of jet models have been developed and explored in isolated clusters, including simple fluxes at cell boundaries (Gaspari et al. 2011), limited-lifetime jets (Morsony et al. 2010), extended jets (Cattaneo & Teyssier 2007), wide-angle jets (Sternberg et al. 2007), and precessing jets (Falceta-Gonçalves et al. 2010a). In cosmological runs, only the simplest jets (fluxes driven at cell boundaries) have been explored (Dubois et al. 2010). Due to the nature of jet-based feedback, these have only been implemented in AMR codes.

Bubbles are more commonly incorporated in SPH simulations. Sijacki et al. (2007) developed a sophisticated model that links the bubble radius to the energy released from accretion and the local density, so that bubbles produced are in pressure equilibrium. These authors also include a "quasar" mode to account for highly energetic ($\dot{M} > 0.1\dot{M}_{\rm Edd}$) feedback events. Simpler bubble models have been incorporated in full cosmological simulations, including fixed-radius bubbles (Di Matteo et al. 2008) and bubbles that only affect the nearest N particles (Booth & Schaye 2009). Bubbles have also been investigated in AMR simulations of isolated mock clusters, both in the context of already-formed magnetically-supported bubbles (Ruszkowski et al. 2007), buoyant bubbles (Gardini 2007), and more realistic slowly inflated bubbles (Jones & De Young 2005).

Magnetized bubbles have been studied, but these have not been linked to an accretion rate, i.e. they have been either already formed (e.g., Ruszkowski et al. 2007) or given an assumed strength (e.g., Xu et al. 2008a). We will investigate the effects of magnetic fields on subgrid models and the ability of various models to magnetize the surrounding cluster atmosphere in Chapter 3.

1.5.4 Subgrid models of supermassive black holes

AGN are usually studied in the context of a single cluster (e.g., Sijacki et al. 2007; Cattaneo & Teyssier 2007; Brüggen & Scannapieco 2009). To include them in a fully cosmological simulation, we must track and evolve the underlying supermassive black holes (SMBHs). SMBHs are born via unknown processes at high redshift (e.g., Madau & Rees 2001; Koushiappas et al. 2004; Islam et al. 2004) and as the host galaxies merge the SMBHs merge as well (Hopkins et al. 2010). The merger process can possibly trigger enhanced accretion events (Treister et al. 2010) and sometimes eject the merging black holes out of the system (Bogdanovic et al. 2007). As with the accretion and feedback processes described above, the formation and merging processes operate at scales below those which we can currently resolve in cosmological simulations.

Authors have taken a variety of approaches with increasing levels of sophistication. The simplest approach is to examine black holes in a post-processing analysis of merger trees derived from simulation (e.g., Micic et al. 2007), but these must make assumptions about merger rates and gas feedback. The most straightforward method to directly include SMBHs in the simulation is to seed density peaks with black hole particles (Dubois et al. 2010). However, these approaches must set artificial limits on the production of black holes since noise in the density field can lead to spurious production, and they do not reproduce the known relations between SMBH mass and the surrounding gas properties, such as galactic bulge luminosity.

The most sophisticated approaches involve finding halos during the evolution of the simulation (Sijacki et al. 2007). Assumptions must still be made regarding the initial seed mass and criteria for merging. With appropriate adjustments to the subgrid parameters, these models can reproduce the observed SMBH-bulge correlations (Booth & Schaye 2009). We have investigated in detail these SMBH subgrid models (Sutter & Ricker 2010) and will present our analysis and results in Chapter 4.

1.5.5 The FLASH code

The primary simulation tool in this manuscript is the AMR magnetohydrodynamics plus N-body code FLASH. FLASH was originally developed under the DOE ASC/Alliances Program at the University of Chicago Flash Center for simulations of Type Ia supernovae. It has since been applied to a wide range of problems, including planet formation, star clusters, clusters of galaxies, turbulent reactive flows, laser-driven shock experiments, and fluid instabilities. Its core technology, AMR, allows high-resolution meshes to be placed only in regions of interest (Berger & Oliger 1984; Colella & Woodward 1984). FLASH's AMR capability is provided by the NASA-funded PARAMESH library (MacNeice et al. 2000). Its object-based framework and automated testing suite make the code reliable and simple to use. It is written in Fortran 90, with some C

routines and Python integration and testing tools. FLASH is freely available online and has more than 300 users. We will use two versions of FLASH in this manuscript: version 2.5 and 3.3.

FLASH 2.5 uses a traditional directionally split, resistive, compressible MHD solver based on the algorithm of (Powell 1999), which requires projection cleaning (Brackbill & Barnes 1980) to remove divergences from the magnetic field. This cleaning method utilizes the multigrid Poisson solver. FLASH 3.3 features a highly efficient MHD solver that explicitly maintains div(B) = 0. This new solver is based on a directionally unsplit method developed by Dongwook Lee as part of his Ph.D. thesis work (Lee 2006; LEE & DEANE 2009). Lee's method uses staggered-mesh differencing and constrained transport with multi-dimensional fluxes obtained from solution of the MHD Riemann problem. The method also employs efficient dissipation controls to prevent the growth of instabilities that arise in traditional constrained-transport schemes.

Elliptic solvers are essential for many astrophysical problems because of the need to solve the Poisson equation for the gravitational potential. The FLASH distribution has long provided users with two options for self-gravity: a multipole solver for problems with nearly spherical symmetry and isolated boundary conditions, and a relaxation-based multigrid solver for general problems with isolated or periodic boundary conditions. The multigrid solver has historically required a significant fraction of the run time and exhibited only modest strong scaling. However, multigrid methods have proven to be very successful for elliptic problems on adaptive meshes (Trottenberg et al. 2000), so we are strongly motivated to maintain our focus in this area.

FLASH 3.3 incorporates a new "direct" multigrid solver that uses a version of the algorithm described by Huang & Greengard (2000). This algorithm improves considerably upon relaxation-based multigrid solvers by allowing refined patches to be solved directly using "black-box" uniform-grid solvers. Unlike the direct method described by Couchman (1991), the HG algorithm properly minimizes the global residual by allowing information to flow back from fine meshes to coarse meshes. However, it is formulated on a finite-difference mesh in which refined patches are not permitted to touch. Our version is modified to work with finite-volume oct-tree AMR meshes, such as those used by PARAMESH (Ricker 2008). To improve scalability, this multigrid solver is coupled to a parallel FFT algorithm to compute solutions on the course mesh.

To identify halos, our work in Chapter 2 is based on a simple parallelized FOF algorithm. However, the remainder of our research is based on a newly-developed algorithm, pSO (Sutter & Ricker 2010). The parallel spherical overdensity (pSO) halo finder is a fast, highly scalable tool integrated into the FLASH simulation code. Designed to provide on-the-fly halo finding and analysis for use in subgrid modeling, merger tree analysis, and adaptive refinement schemes, pSO uses a minimal amount of memory and processing time. The pSO algorithm begins by mapping dark matter particles onto a mesh using cloud-

in-cell weighting. Spheres are drawn around density peaks until the internal average density equals a specified overdensity relative to the cosmological critical density. The algorithm determines the halo center, bulk velocity, mass, and velocity dispersion without additional post-processing. pSO is provided as both an API for use in-code and as a stand-alone halo finder.

1.6 This work

In Chapter 2 we present a first estimate based on a cosmological gasdynamics simulation of galaxy cluster radio halo counts to be expected in forthcoming low-frequency radio surveys. Our estimate is based on a FLASH simulation of the ΛCDM model for which we have assigned radio power to clusters via a model which relates radio emissivity to cluster magnetic field strength, intracluster turbulence, and density. We vary several free parameters of this model and find that radio halo number counts are highly dependent - up to a factor of two - on the average magnetic field strength in clusters and that upcoming surveys may be able to use number counts to constrain cluster magnetic field properties. We find that expected number counts can be degenerate with both re-acceleration and hadronic secondary models of cosmic ray generation. However, by building mock radio sky maps we demonstrate that surveys such as LOFAR may have sufficient resolution and sensitivity to break this degeneracy by imaging individual clusters.

In Chapter 3, we investigate the scenario in which active galactic nuclei (AGN) found at the centers of clusters of galaxies are a source for cluster-wide magnetic fields. To evaluate this scenario, we present 3D adaptive mesh refinement MHD simulations of a cool-core cluster that include injection of kinetic, thermal, and magnetic energy via an AGN-powered jet. Using the MHD solver in FLASH 3.3, we compare several sub-resolution approaches that link the estimated accretion rate as measured on the simulation mesh to the accretion rate onto the central black hole and the resulting feedback. We examine the effects of magnetized outflows on the accretion history of the black hole and discuss the ability of these models to magnetize the cluster medium.

Chapter 4 focuses on subgrid models of supermassive black holes (SMBHs). This chapter contains material previously published in Sutter & Ricker (2010). While SMBHs play an important role in galaxy and cluster evolution, at present they can only be included in large-scale cosmological simulation via subgrid techniques. However, these subgrid models have not been studied in a systematic fashion. Using a newly developed fast, parallel spherical overdensity halo finder built into the simulation code FLASH, we perform a suite of dark matter-only cosmological simulations to study the effects of subgrid model choice on relations between SMBH mass and dark matter halo mass and velocity dispersion. We examine three aspects of SMBH subgrid models: the choice of initial black hole seed mass, the test for merging two black holes, and the frequency of applying

the subgrid model. We also examine the role that merging can play in determining the observed SMBH scaling relations, ignoring the effects of SMBH-driven accretion and feedback. We find that the choice of subgrid model can dramatically affect the black hole merger rate, the cosmic SMBH mass density, and the low-redshift relations with halo properties. We also find that it is possible to reproduce observations of the low-redshift relations without accretion and feedback, depending on the choice of subgrid model.

Finally, in Chapter 5 we will use the preceding work to outline a large-scale cosmological MHD calculation of the growth and evolution of magnetic fields in the early universe. Using FLASH 3.3, we seed halos with black holes and model the accretion of gas onto these black holes and the subsequent magnetized feedback. We can use this simulation to identify the earliest redshift of significant magnetic growth in cosmic structures and the relationship between magnetic field strength and halo properties. We will be able to follow the relationship between magnetic fields and cluster properties as the clusters grow and evolve.

Chapter 2

A first estimate of radio halo statistics from large-scale cosmological simulation

2.1 Introduction

Although diffuse radio halos were discovered in clusters of galaxies more than 50 years ago (Large et al. 1959), complete statistical information about them has only been forthcoming within the past decade, owing to their rarity, steep spectra, and low surface brightnesses. Radio surveys using the Very Large Array (VLA) (Giovannini 1999; Cohen et al. 2007; Giovannini 2009), the Westerbork Synthesis Radio Telescope (WSRT) (Kempner & Sarazin 2001), and the Giant Metrewave Radio Telescope (GMRT) (Brunetti et al. 2007) have detected ~ 20 radio halos at redshifts up to $z \sim 0.4$, along with a variety of smaller-scale radio features in clusters (Kempner et al. 2004). Only about 1/3 of massive ($> 10^{15}\ M_{\odot}$) clusters are known to host radio halos, and the halos themselves are not associated with any particular member galaxy, but rather dispersed throughout the intracluster medium (ICM) (Feretti et al. 2004). For clusters that do host halos, strong correlations are seen between radio power and X-ray luminosity (Liang et al. 2000; Bacchi et al. 2003; Cassano et al. 2006; Brunetti et al. 2007), halo mass (Cassano et al. 2006), and gas velocity dispersion (Cassano et al. 2008). Also, observations indicate a strong connection between the presence of a halo and morphological evidence for recent mergers (Buote 2001; Brunetti et al. 2009), although some exceptions do exist (Russell et al. 2011). Indeed, recent simulations of merging clusters suggest that the fraction of turbulent clusters is roughly equal to the fraction of clusters hosting radio halos (Vazza et al. 2010).

The proximate cause of diffuse radio halos is most likely synchrotron emission by high-energy electrons in galaxy cluster magnetic fields, but the means of generating and accelerating these electrons remains an open question, since these electrons have relatively short (< 1 Gyr) lifetimes. Dennison (1980) proposed that cosmic ray electrons are produced as secondary particles by hadronic collisions of > 1 GeV cosmic ray protons with ambient thermal ICM protons. The protons can be accelerated by shocks and quickly (< 1 Gyr) diffuse through-

out the cluster. This naturally explains the diffusive, cluster-wide properties of radio halos (Blasi 1999; Pfrommer et al. 2008). Some observations have discovered a correlation between radio and X-ray surface brightness, another feature of this model (Keshet & Loeb 2010). Note that these observations also indicate that the ICM must be highly magnetized (~ 3 μG). Gamma-ray observations place limits on the abundance of high-energy protons, since they may inverse Compton scatter off of cosmic microwave background photons. These observations indicate that hadronic cosmic rays may contribute at most 5-10 % of the total pressure support in clusters (Ackermann et al. 2010). However, this model may have difficulty explaining the diminishing of radio power with radius within the Coma cluster and the scaling of radio power with X-ray luminosity (Donnert et al. 2010a,b). Also, the ability of the high-energy protons to stream away from their sources can have significant implications for the resulting radio emission (Enß lin et al. 2011).

Another promising explanation for the acceleration of the cosmic ray electrons is second-order Fermi acceleration by intracluster turbulence (Schlickeiser et al. 1987; Petrosian 2001; Brunetti & Lazarian 2011). The cosmic rays themselves must be injected into the ICM by radio galaxies (Jaffe 1977) or accelerated by merger shocks. Since the lifetime of synchrotron-emitting GeV electrons in the intracluster magnetic field ($\langle B \rangle \sim 1 - 10$ μG) is at most ~ 1 Gyr (Kuo et al. 2003; Brunetti et al. 2009), these electrons must be re-accelerated by some process that operates in a more diffuse fashion. Hence a local acceleration mechanism is favored. Some low-frequency observations support the re-acceleration model (Brunetti et al. 2008). Assuming that ICM turbulence locally accelerates cosmic rays to produce clusterwide radio halos, we expect that the radio emission should correlate spatially with the turbulent pressure $\langle \rho v^2 \rangle$. Indeed, this expectation is consistent with some observations (Govoni et al. 2004). However, the identity of the cosmic rays as primary electrons initially boosted by merger shocks and active galactic nuclei, or as hadronic secondaries produced by collisions of cosmic-ray protons with thermal ICM protons, remains to be determined.

Within the next decade and a half the number of known radio halos should increase dramatically owing to the development of sensitive low-frequency radio surveys based on technology originally developed for cellular communications. Examples of the operating and planned instruments include the LOw Frequency ARray (LOFAR), GMRT, the Karoo Array Telescope (KAT), and the Square Kilometer Array (SKA). LOFAR, for example, will be sensitive to radio frequencies between 20 and 240 MHz and will be able to detect sources as faint as $0.4 - 110$ mJy at $15 - 240$ MHz (Jarvis 2007; Rottgering 2003; Rottgering et al. 2006). These characteristics are ideal for detecting and counting radio halos such as the Coma radio halo ($\sim$640 mJy at 1.4 GHz with a spectral index $\sim 0.4 - 0.75$; Deiss et al. 1997) as far away as a redshift of 0.75. Indeed, estimates of radio halo counts using turbulent re-acceleration models predict many

more radio halos at low frequency than at higher frequencies (Cassano et al. 2008).

Counts of cluster radio halos, in addition to probing the evolution of cluster merger activity, also potentially provide an additional means for using clusters to constrain cosmological parameters. Unlike other methods for using clusters as cosmological probes that are based on their mass function or gas fraction, this measure is linked to their "instantaneous" formation activity rather than their time-integrated numbers. In principle its dependence on the cosmological volume element dV/dz and the growth factor of linear density fluctuations $D_+(z)$ should also be different from and thus complementary to the more traditional measures. Additionally, if the cosmic-ray electrons responsible for the halos are accelerated by shocks and/or turbulence generated by mergers, it is reasonable to expect that recently merged clusters would display the most radio activity. Thus determining the abundances, spectral distributions, and other characteristics of radio halos as functions of redshift could provide information about the evolution of clusters and their merging activity over time.

In this paper we present results from a numerical simulation of cluster formation intended to study the form and evolution of the radio halo population as might be observed in a typical LOFAR survey. We will apply a model of radio power that is generalized to include both hadronic and re-acceleration cosmic ray generation mechanisms. The means employed in the conversion of cluster density and velocity information into a simulated LOFAR radio sky are somewhat rudimentary given the uncertainties in the physics responsible for radio halos and the small scales on which it likely operates. However, our results are the first based on combining a large-scale cosmological gasdynamics simulation with observed features of radio halos, and they show that future simulations with higher resolution and more realistic physics should enable straightforward comparisons with results from low-frequency radio observatories. While earlier analytical studies have involved more sophisticated models of CR generation, these have relied on the X-ray luminosity function combined with the known correlation between radio power and X-ray luminosity (Enß lin & Roettgering 2002), the Press-Schechter mass function (Cassano et al. 2006), or Monte-Carlo realizations (Cassano 2010). Donnert et al. (2010a) introduced a simulation of the local group including magnetic field injection and CR generation, but these results may be sensitive to the assumptions made about the magnetic field injection and are limited in volume. Our simulation, while involving simpler physics, covers a large (1 h^{-1} Gpc) volume, which will allow us to gather reliable statistics and produce mock whole-sky radio maps, which are difficult to produce accurately with methods based on analytical mass functions.

In Section 2.2 we provide details of the cosmological simulation, while in Section 2.3 we explain the procedure used to associate a radio power with each cluster. We will explore the range of valid models in Section 2.4 and use these results to produce radio power relations in Section 2.5. Section 2.6 discusses the

results in terms of radio halo counts as functions of flux and redshift, and we present various example radio sky maps in Section 2.7. Finally, we conclude in Section 2.8 with a discussion of future directions.

2.2 The simulation

We simulated structure formation using the ΛCDM cosmological model within a periodic box spanning 1024 h^{-1} comoving Mpc. We assumed a Hubble constant $H_0 = 100h$ km s^{-1} Mpc^{-1} with $h = 0.719$, a present-day matter density parameter $\Omega_{m,0} = 0.262$, baryonic density parameter $\Omega_{b,0} = 0.0437$, vacuum density parameter $\Omega_{\Lambda,0} = 0.738$, and spatially flat geometry, as suggested by results from WMAP data (Komatsu et al. 2011). Initial conditions for 1024^3 dark matter particles at a starting redshift $z_i = 66$ were generated using a version of GRAFIC (Bertschinger 2001) modified to accept power spectra generated by CMBFAST (Seljak & Zaldarriaga 1996). We normalized the power spectrum using $\sigma_8 = 0.74$. We included adiabatic gasdynamics for the baryons using a perfect-gas equation of state with adiabatic index $\gamma = 5/3$ and mean particle mass determined using interpolation from collisional ionization equilibrium tables for primordial gas from Sutherland & Dopita (1993). Although no additional physics is included in this first calculation, we initialized the gas temperature at z_i to a constant value of 9100 K, corresponding to a preheating entropy of 250 keV cm^2 at a redshift of 3. This level of preheating is adequate to reproduce the observed X-ray luminosity-temperature relation (Bialek et al. 2001) for clusters of galaxies, although details of the scatter in this relation and its correlation with other cluster properties such as the presence of cold cores are not constrained to match observations.

We ran our simulation using the FLASH code version 3.3 (Fryxell et al. 2000; Dubey et al. 2008) using a new direct multigrid Poisson solver (Ricker 2008) with 1024^3 dark matter particles and a uniform 1024^3 base mesh. The piecewise-parabolic method (Colella & Woodward 1984) was used to solve the Euler equations of gasdynamics. To achieve the resolution necessary to estimate the level of turbulence within clusters, we used adaptive mesh refinement within 100 preselected regions. Each region was 10 h^{-1} Mpc on a side centered on a halo identified using a lower-resolution precursor run. The halos were selected to uniformly sample the range of resolvable halos using mass function weighting to ensure a representative sample in the full simulation. Within the preselected regions we used a dark matter particle refinement criterion, allowing no more than 100 dark matter particles within a zone. We refined to a maximum resolution of 32 h^{-1} kpc. Estimates of the integral scale of turbulence in clusters suggests a power law spectrum from spatial scales of 0.8 to 8 kpc, with no visible turnover (Kuchar & Enß lin 2011), indicating that the integral scale is larger and that our resolution is a reasonable approximation. Since the refined regions were larger than the halos on which they were centered, we captured a total

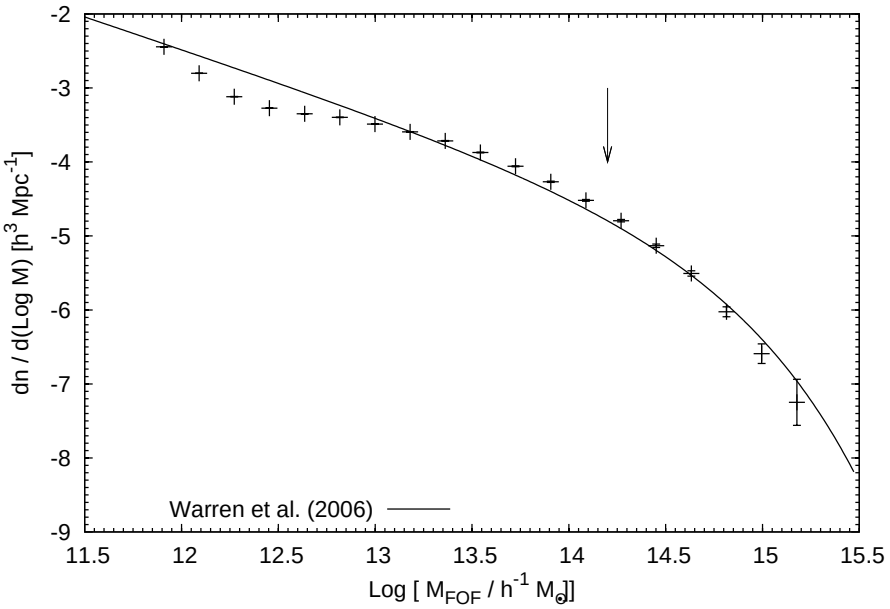

Figure 2.1: Mass function of all halos in the simulation volume compared against best fit of Warren et al. (2006). Errors bars are given at 2σ and the vertical arrow denotes our minimum resolvable FOF halo mass.

of 131 high-resolution clusters. We ran the code on the Cray XT5 machine at Oak Ridge National Laboratory, where the simulation required approximately 450,000 CPU-hours on 16,000 processors. Output files containing both particle and gas information were written beginning at $z = 2.0$ at every $\Delta z = 0.25$ for the purposes of mock sky generation.

2.2.1 Halo finding and virial mass

We created halo catalogs from the simulation outputs using the friends-of-friends (FOF) technique with a linking length parameter $b = 0.2$ and considered only halos with at least $3,000$ particles (i.e. an FOF dark-matter mass of $2 \times 10^{14}\ h^{-1}\ \mathrm{M}_{\odot}$). Our base-grid spatial resolution is sufficient to ensure accurate counts of halos with this many particles throughout the range of redshifts we consider here (Heitmann et al. 2005; Lukić et al. 2007). Figure 2.1 shows our mass function for all halos in the simulation volume compared against the best fit of Warren et al. (2006). We find fewer high-mass objects relative to the Warren fit, but this is not unexpected (see, for example, Knebe et al. 2011). Also, we tend to over-produce low mass objects, even below our resolvability limit. However, note that even though we produce too many low-mass objects relative to the Warren fit below our resolution limit, our mass function still turns away from the expected slope, and thus we cannot fully trust the number counts below this threshold. There were ~ 4000 resolvable objects at $z = 0.0$.

To make comparisons with the observational analysis of Cassano et al. (2006)

(hereafter CBS06), we compute spherical overdensity radii R_v for each of our halos. For the high-resolution sample (i.e., the adaptively-refined halos within the 100 predefined regions), we compute overdensities including both just dark matter and with dark matter plus gas. For the remaining fixed-resolution halos outside the predefined regions, we only include dark matter in the overdensity calculation since the gas data in these halos were poorly resolved. In Section 2.6 we discuss our procedure for assigning radio power to these lower-resolution halos. We use the same definition of overdensity as in CBS06, namely Kitayama & Suto (1996):

$$\Delta_c = 18\pi^2 \left(1 + 0.4093\omega(z)^{0.9052}\right), \tag{2.1}$$

where $\omega(z) \equiv \Omega_f(z)^{-1} - 1$. Here,

$$\Omega_f = \frac{\Omega_{m,0}(1+z)^3}{\Omega_{m,0}(1+z)^3 + \Omega_\Lambda}. \tag{2.2}$$

The virial mass, M_v, follows as $M_v = 4/3\pi\Delta_c\rho_m(z)R_v^3$, where $\rho_m(z)$ is the mean mass density:

$$\rho_m(z) = 2.87 \times 10^{11}\Omega_{m,0}(1+z)^3\ h^2\ \ M_\odot\ \mathrm{Mpc}^{-3}. \tag{2.3}$$

The most massive cluster in our simulation has a mass $M_v = 1.2\times10^{15}\ h^{-1}\ \mathrm{M}_\odot$.

2.3 Simulating radio emission

We identify gas zones within R_v for each halo and associate them with the halos. We create two-dimensional maps of projected density and projected turbulent pressure, $m_i v_i^2$, where m_i is the mass in the cell i and the average velocity is defined as the difference between the measured velocity in the cell and the center-of-mass velocity of the entire cluster, $\mathbf{v}_i \equiv bfv_i - \mathbf{v}_{\mathrm{cm}}$. Note that this strategy does not distinguish turbulence from bulk motions within the cluster (an alternative approach which attempts to remove bulk velocities from this calculation is discussed in Paul et al. 2011). We use these projections in two ways: to create simulated surface brightness maps and to construct total radio luminosities by integrating these quantities across the entire projected cluster surface out to the virial radius. The integrated projected density is of course M_v and we will designate the integrated turbulent pressure as $\Gamma_v = \sum_i m_i v_i^2$.

Therefore we can create simulated radio surface brightness maps for our clusters by normalizing maps of projected turbulent pressure and projected mass using assumed radio luminosities and rest-frame spectra. Because we may not fully resolve intracluster turbulence, the total amount of turbulent pressure in our clusters may be lower than the $\sim 10\%$ of hydrostatic pressure seen in high-resolution simulations (Ricker & Sarazin 2001; Ritchie & Thomas 2002; Mitchell et al. 2009). However, because the normalization of the radio power

is supplied independently (see below), all we require of the turbulent pressure maps is that they be sufficiently diffuse and representative in spatial extent of clusters containing radio halos. The detailed structure of the maps should not be regarded as realistic. Because of the beam smearing described below, this fact does not significantly affect our analysis. Also, while we cannot depend on these simulated clusters to provide correct high-resolution X-ray and radio surface brightness maps, we can still use them to identify broad features, such large-scale shocks and the relative radial dependence of turbulence.

Using these integrated quantities, we construct a rest frame 1.4 GHz radio power via

$$P_{1.4\ \mathrm{GHz}} = C_s B M_v^a \Gamma_v^c, \tag{2.4}$$

where C_s is a scaling constant, M_v is the virial mass, Γ_v is the virial turbulent pressure, and B is the average cluster magnetic field as a function of mass:

$$B = \frac{B(M_v)^2}{(B(M_v)^2 + B_{\mathrm{CMB}}^2)^2}, \tag{2.5}$$

where $B(M_v) \equiv \langle B \rangle (M_v/\langle M \rangle)^b$ and $B_{\mathrm{CMB}} \equiv 3.2(1+z)^2\ \mu$G is the equivalent magnetic field strength of the cosmic microwave background. This formulation separates physical processes that generate cosmic rays (M_v and Γ_v) from those that contribute to radio emission (B in the numerator) and CR losses due to emission (B^2 in the denominator) and inverse Compton scattering (B_{CMB}). The losses enter into this equation because they limit the maximum CR energy. In this formalism, M_v measures the total cluster mass and thus should scale with the dependence of cosmic ray generation on hadronic secondary processes, whereas Γ_v measures the total cluster turbulence and thus should provide a measure of the re-acceleration of cosmic ray electrons by that turbulence. We will set $\langle M \rangle = 1.5 \times 10^{15}\ M_\odot$. There are thus five independent parameters: the average magnetic field $\langle B \rangle$, the scaling of magnetic field with cluster mass, b, the scaling of radio power with virial mass, a, the scaling of radio power with turbulent pressure, c, and an overall scaling parameter C_s. A summary of our model parameters is given in Table 2.1. This model is a generalization and extension of the one derived in Cassano & Brunetti (2005). We are fixing the form of the magnetic field dependence since the radio synchrotron power will always depend on magnetic field pressure (B^2) independently of the cosmic ray generation and acceleration mechanisms (see Cassano & Brunetti (2005) for a discussion). We stress that although this model is relatively simple and ignores the streaming and diffusion of cosmic rays (Enß lin et al. 2011), it allows us to explore a range of plausible acceleration mechanisms and examine relative changes to luminosity functions, scaling relations, and other radio properties.

This model allows us to explore both cosmic ray generation mechanisms or a mixture of both. For example, the hadronic secondaries model should predict radio power which scales with cluster mass, so $c = 0$ in this case. A

Table 2.1: Parameters of the radio luminosity model.

Parameter	Description
C_s	Overall scaling
$\langle B \rangle$	Average magnetic field
b	Scaling of magnetic field with cluster mass
a	Scaling of radio power with cluster mass
c	Scaling of radio power with turbulent pressure

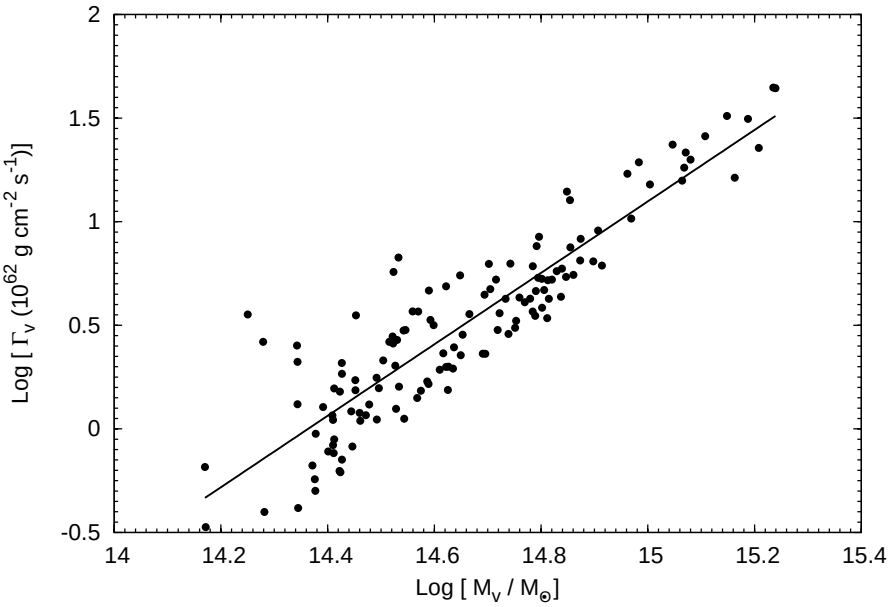

Figure 2.2: Total turbulent pressure, Γ_v, versus virial mass, M_v at $z = 0$. Shown is a best-fit line in log space. The slope of the line is ~ 1.7.

re-acceleration model is proportional to turbulent pressure, so a would be 0. Note that the model of CSB06 is based on re-acceleration, but only scales with cluster mass. This is because Γ_v roughly scales with M_v with a logarithmic slope of 1.7, as shown in Figure 2.2. Note that the model of CSB06 corresponds here to $a = 4/3$ and $c = 0$.

A degeneracy exists for calculations of total radio luminosity between models that scale with turbulent pressure and those that scale with mass, since we may freely exchange c for $1.7a$ and vice-versa. However, a more detailed examination of cluster atmospheres reveals striking differences. Even with the relatively low resolution of our simulation, and the resulting inability to fully reproduce correct structures in the cluster atmospheres, we can identify gross differences in the projected maps. Figure 2.3 shows projections of mass and turbulent pressure for two clusters. The mass projections of both clusters are roughly spherical, as expected. However, the turbulent pressure maps show more varying morphology. While the halos are roughly equal in mass ($\sim 8 \times 10^{14}\ h^{-1}\ \mathrm{M}_\odot$), one shows much greater turbulent structure, indicating recent merger activity, which may

explain the scatter in Figure 2.2. Thus, even though different mechanisms of CR generation may produce similar cluster counts (as we will see below), high-resolution radio and X-ray imaging of clusters may help to determine which mechanism dominates.

Since we do not include in our simulations any detailed cosmic ray generation mechanisms, and we because we want to keep our model as general as possible, we must fix the scaling parameter C_s by using observations. This scaling will then combine any extra constants and parameters not included in our analysis. For a given set of model parameters, we set C_s by assigning a radio luminosity to the most massive cluster in our simulation. We do this with the $P_{1.4} - M_v$ relation found in CBS06, which is based on combining the observed correlation of radio halo power and X-ray luminosity with the correlation between X-ray luminosity and mass:

$$\log\left[\frac{P_{1.4}}{3.16\times10^{24}h_{70}^{-1}\frac{\mathrm{W}}{\mathrm{Hz}}}\right] = (2.9\pm0.4)\log\left[\frac{M_v}{10^{15}\ h_{70}^{-1}\ \mathrm{M}_\odot}\right] - (0.814\pm0.147) \tag{2.6}$$

We then apply this same constant scaling to all remaining high-resolution halos in the sample. While the scaling may contain some additional dependence on mass or turbulent pressure not accounted for in our parameterization, this can easily be accommodated in our study by adding to (or subtracting from) the parameters a and c. An example of a particular model compared against the observed relation is shown in Figure 2.4.

Since no radio halos have been observed beyond a redshift of ~ 0.4, and available statistics do not strongly constrain evolution in this relation, we will fix the scaling at $z = 0$ and apply the same scaling to higher-redshift clusters. We will also assume power-law energy spectra with a spectral index of 1.2, consistent with low-redshift observations (Feretti et al. 2004). Finally, we do not include in our model the relationship between synchrotron break frequency and the presence of a radio halo, which can be used to calibrate models to the observed fraction of clusters hosting radio halos (CBS06).

2.4 Exploration of valid models

To constrain our model choices we make selections for the model parameters, assign radio powers to the clusters using the procedure described above, find the best fit line to our derived $P_{1.4} - M_v$ data, and compare the best-fit slope and normalization to the observed values. We will only accept model choices that produce fits that lie within 1σ of the observed relation. Note that this is a similar strategy to the one employed by CBS06, but that we are applying a more stringent test by enforcing the known relation to lower radio powers than they consider. Obviously, we could just select two models that span the valid range and analyze their difference, but we wish to explore the relationships among the

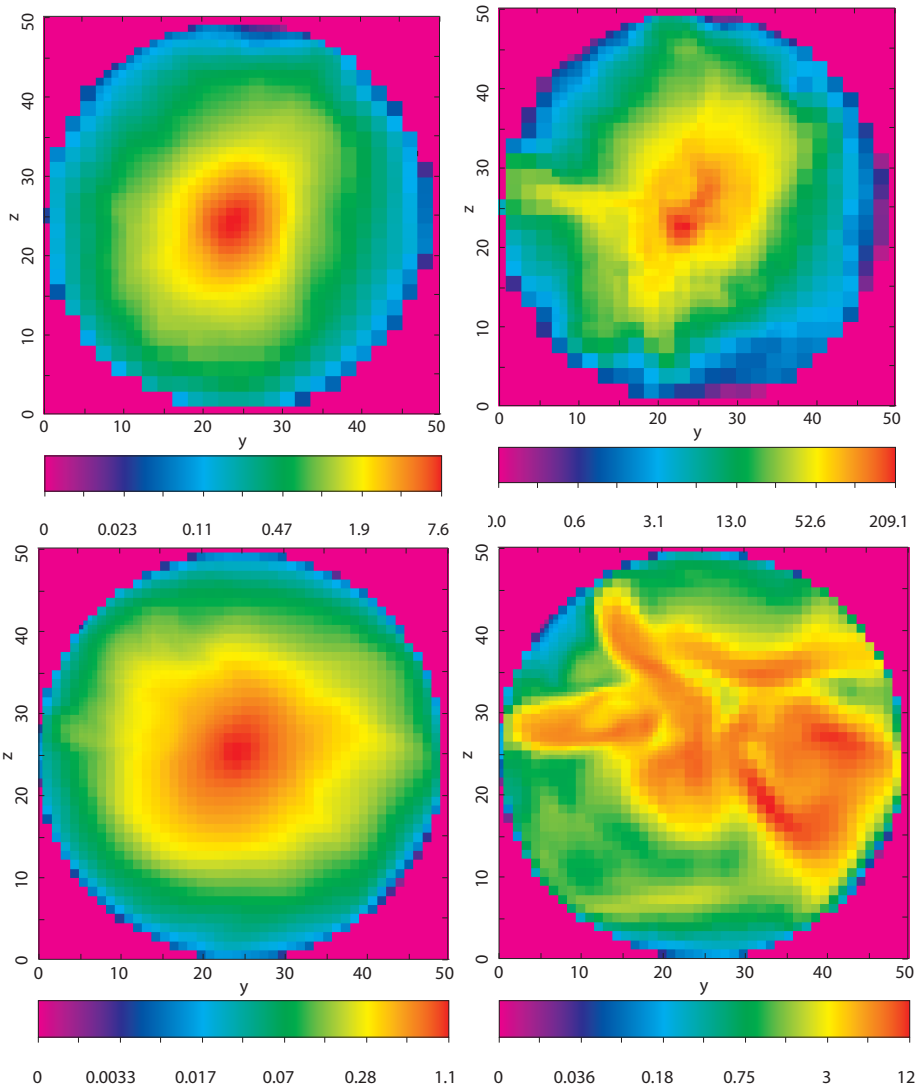

Figure 2.3: Projected density (left-hand plots) and projected turbulent pressure (right-hand plots) for a two clusters (top and bottom rows). Projections are taken along the x-direction within R_v for each cluster. The units for projected density are 10^{44} g and for projected turbulent velocity are 10^{58} g cm^2 s^{-2}. The images are normalized to a uniform grid 50 cells on a side.

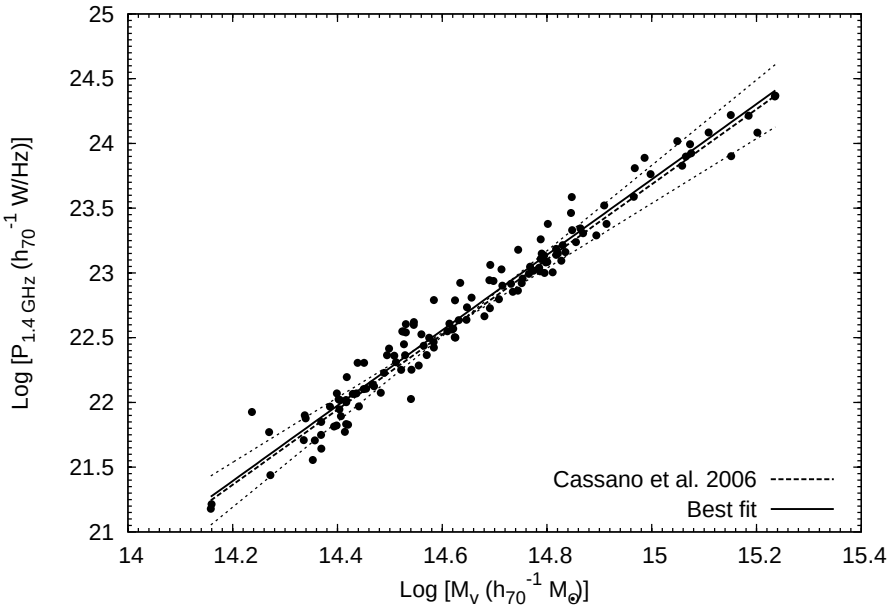

Figure 2.4: Radio halo luminosity versus virial mass for one example model (points) with best fit (solid line) compared against the observed best fit found in CBS06 (thick dotted line) and 1σ uncertainties (thin dotted lines). The example uses parameters $\langle B \rangle = 3.2\mu$G, $b = 0.8$, $a = 0.0$, and $c = 0.8$.

various model parameters and the separate consequences of varying each one.

Figure 2.5 shows contour plots of allowable models. We vary $\langle B \rangle$ from 0.2 to 6.0 μG, b from 0.5 to 1.5, a from 0.0 to 2.5, and finally c from 0.0 to 1.5. We could explore even larger values of a and c, but as we will discuss below 1σ uncertainties in the measured $P_{1.4\mathrm{GHz}} - M_v$ relation place upper limits on the scaling of a and c at this chosen maximum value. Note that we also assume a positive correlation between radio power and M_v and Γ_v. While we allow the mass and turbulent pressure scaling parameters to vary all the way to 0, we constrain the scalings associated with magnetic fields. We constrain the average cluster magnetic field strength from 0.2 μG, which is set by observed upper limits on hard X-ray emission (CBS06), to 6.0 μG, which is a reasonable upper limit from rotation measure observations (e.g. Govoni et al. 2004; Bonafede et al. 2011). The restrictions on b come from the simulations of Dolag et al. (2002), which followed the adiabatic compression of seed magnetic fields as clusters formed. They found a scaling $B \propto M^{1.33}$. We allow some uncertainty in this value, but do not allow a compete lack of scaling of magnetic field with cluster mass. For simplicity, we have combined the mass and turbulent pressure values as $a + c$, so $a + c$ is varied from 0.0 to 4.0. The contours for each individual parameter show structures similar to those for this combined parameter. Note that in these plots we are showing the *maximum* allowed value for a given point on each contour plot. All values less than the plotted value are also allowed.

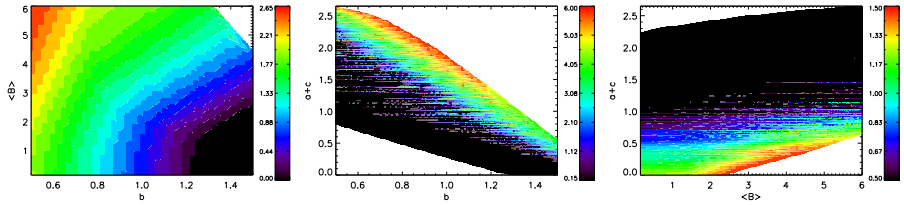

(a) $a + c$ as a function of $\langle B \rangle$ and b.

(b) $\langle B \rangle$ as a function of $a + c$ and b.

(c) b as a function of $a + c$ and $\langle B \rangle$.

Figure 2.5: Contours of allowed radio halo model parameters. Allowed models are determined by fitting a line to our $P_{1.4} - M_v$ data and ensuring that the slope and normalization are within 1σ of the known relation.

For example, for $b = 1.0$ and $\langle B \rangle = 3.0$ μG the allowable values for $a + c$ are from 0.0 to ~ 1.0.

We find that very strong magnetic fields are only allowed if the scalings with virial mass and turbulent pressure are very steep. In these cases strong radio power in low mass objects due to high $\langle B \rangle$ is offset by significantly lower radio power associated with M_v or Γ_v. If the scaling of magnetic field strength with cluster mass is above unity, then it is difficult to fit strong magnetic fields at high mass within the observed relations. We find several regions forbidden in our models: strong magnetic fields coupled with high b, and very low or very high $a + c$ and b values.

We see interesting structures in the contours: steps and wiggles in the $a + c$ plots, and striations in the others. These are due to the scatter that develops in the $P_{1.4} - M_v$ relations and the resulting variations of the best fit lines. Because of this variation, we do not see monotonically increasing (or decreasing) behavior in the contour plots, especially at extreme values. Surprisingly, we find that $a = c = 0.0$ is allowed, but only at low $\langle B \rangle$ and high b. This is because of the implicit mass dependence in the calculation of the cluster magnetic field strength, $B(M_v)$. Also, the model used in CBS06 is *forbidden* in our analysis, since we are enforcing the known relation to a wider range of cluster masses. However, we can allow their model choice when restricting ourselves to the mass ranges they consider.

We use these contours to guide our selection of models for further study. We wish to adequately sample the space of allowable models and explore the limits allowed by observational constraints. We also wish to explore the effects of holding one parameter constant and varying the others to their extreme allowed values. To aid analysis, we collect our choices into six model groups, enumerated in Table 2.2. In this table we list the values chosen for a particular parameter set and a unique designation for that set used in further plots.

In Model Group 1 we set a to 0.0, fix $c = 0.6$, and vary the magnetic field parameters as widely as possible from a minimum of $\langle B \rangle = 0.2$ to 5.8 μG. We also vary the scaling parameter associated with the magnetic field, b. Each $\langle B \rangle$

Table 2.2: Model groups and parameter sets.

Designation	$\langle B \rangle (\mu\mathrm{G})$	b	a	c
Model Group 1: Varying Magnetic Field				
1A	0.2	0.675	0.000	0.600
1B	1.0	1.000	0.000	0.600
1C	3.0	0.800	0.000	0.600
1D	3.0	1.175	0.000	0.600
1E	5.8	1.325	0.000	0.600
Model Group 2: Varying Scaling				
2A	2.0	1.000	0.000	0.335
2B	2.0	1.000	0.000	0.710
Model Group 3: Exchanging a and c				
3A	2.0	1.000	1.300	0.000
3B	2.0	1.000	0.650	0.325
3C	2.0	1.000	0.000	0.650
Model Group 4: Extreme Magnetic Fields, Fixed Scalings				
4A	0.2	1.000	0.250	0.500
4B	4.2	1.000	0.250	0.500
Model Group 5: Extreme Magnetic Fields, Free Scalings				
5A	0.2	0.500	0.000	0.800
5B	6.0	1.325	0.200	0.500
Model Group 6: Extreme Allowed Scalings				
6A	0.2	1.275	0.000	0.000
6B	5.8	0.550	2.438	0.150

is coupled with a unique b, except for $\langle B \rangle = 3.0$ μG, where we examine $b = 0.8$ and $b = 1.175$, which are the minimum and maximum allowed values for this particular configuration. We explore the opposite behavior in Model Set 2 by fixing the magnetic field parameters to $\langle B \rangle = 2.0$ μG and simple linear scaling $b = 1.0$ while having no explicit M_v dependence and studying the maximum and minimum allowed values for turbulent pressure scaling, c. We chose this value of the magnetic field so that we could get the maximum difference in c. We keep the same magnetic field configuration for Model Set 3, but here we exchange a and c using the measured relation (Figure 2.2). In this Model Set we fix the quantity $(a + 2c)$. This allows us to hold the magnetic field fixed while going from a hadronic-like CR model ($c = 0$) to a re-acceleration model ($a = 0$). We designed this Model Set to verify that our results are robust to even exchanges of a and c using the measured relation, which they should be. In Model Set 4 we fix $b = 1.0$, $a = 0.25$, and $c = 0.5$ and examine the extreme allowed average magnetic field. We chose these values of b, a, and c such that we could get the maximum change in $\langle B \rangle$. We repeat this test in Model Set 5, but now allow b, a, and c to vary to accommodate the extreme values studied of $\langle B \rangle$. Finally in Model Set 6 we pick two model parameter sets that represent extremes of all four parameters.

2.5 Radio power relations

We will begin our analysis by using our sample of 131 high-resolution clusters to examine the relationship between radio luminosity and virial mass and X-ray luminosity. To construct X-ray luminosities, we use the `mekal` plasma emissivity model supplied with the XSPEC package (Arnaud 1996). We then build a composite X-ray spectrum for each cluster and use that spectrum to generate the $0.1 - 2.4$ keV rest-frame luminosity within R_v for each cluster. Note that since our simulation does not include cooling and central AGN feedback, our cluster temperatures, and hence X-ray luminosities, are uniformly higher than observed (see Stanek et al. (2010) for a discussion of such effects). However, the slopes of our relations are still within observed limits, and we can still study the relative differences among models and their evolution with redshift.

In Figure 2.6 we show the best-fit slope and normalization for each model, grouped by Model Group, for the $P_{1.4} - M_v$ relation generalized from (Eq. 2.6):

$$\log\left[\frac{P_{1.4}}{3.16 \times 10^{24} h_{70}^{-1} \frac{\mathrm{W}}{\mathrm{Hz}}}\right] = Af \log\left[\frac{M_v}{10^{15}\ h_{70}^{-1}\ \mathrm{M}_\odot}\right] + bf \qquad (2.7)$$

where Af and bf (note that we have added the suffix f for "fit" to distinguish these from the parameters used in our radio power model) are the slope and normalization, respectively. Note that we fix the scaling parameter C_s at each redshift for each model. In essence this assumes that the $P_{1.4\mathrm{GHz}} - M_v$ relation

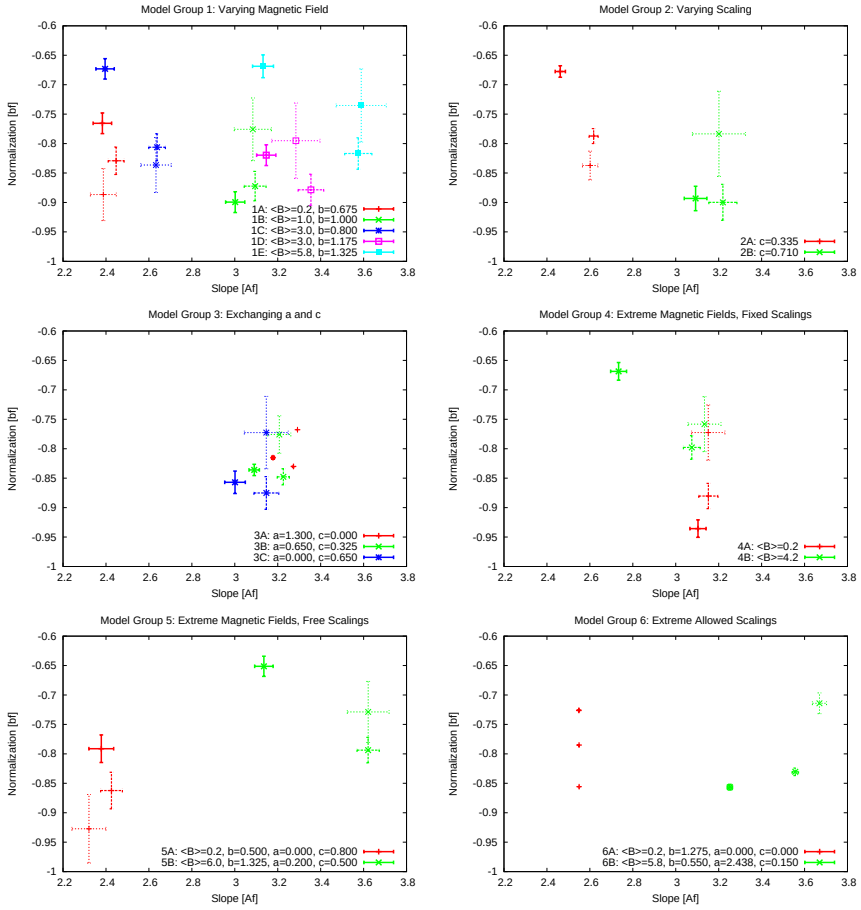

Figure 2.6: Best fits for the $P_{1.4} - M_v$ relation for each radio halo parameter set. Each best fit to Eq. 2.7 generates a slope and normalization, which we represent as a point with 1σ error bars. Solid lines are the best fit at $z = 0.0$, thick dotted lines are $z = 0.25$, and thin dotted lines are $z = 0.5$. We have identified each model with its designation from Table 2.2 and the portions of the model that change in the given Model Group.

holds even at high redshift. For each model we show three points: one each for $z = 0.0$, 0.25, and 0.5. Above redshift 0.5 we do not have enough halos above the minimum mass threshold to generate meaningful statistics. Note that the observational uncertainties essentially fill the entire plotting space.

For Model Group 1, where we vary only the magnetic field parameters, we see a clear separation between models with $b < 1.0$ (1A and 1C) and the remaining models which have $b \geq 1.0$. Model 1C, which has $b = 1.0$, sits precisely at slope $Af = 2.0$. In general, higher values of b lead to steeper slopes, although the effect is strongest near $b = 1.0$ with diminishing effects further from unity. Note especially the differences between models 1C and 1D, which have identical $\langle B \rangle$. The values of b and $\langle B \rangle$ also jointly affect the normalization of the $P_{1.4\mathrm{GHz}} - M_v$ relation, with smaller values b generally leading to lower normalizations.

The redshift evolution of the models in Model Group 1 shows diverse be-

havior. For models with $b < 1.0$ the normalization decreases with increasing redshift in a statistically significant way. This makes sense as the clusters are in general uniformly smaller at higher redshift. However, the slope increases at $z = 0.25$, which perhaps suggests greater variance in the turbulent properties of the clusters. The uncertainties in the values for redshifts 0.25 and 0.5 make them difficult to compare against each other. This redshift dependence of the normalization continues for the other models, except for the case where $b = 1.0$; however, these points lie within their respective uncertainties.

In Model Group 2, where we keep the magnetic field fixed and vary the scaling with turbulent pressure, we see that, as expected, larger values of c lead to steeper slopes and lower normalizations in the best fit relation. Since our scatter is related to the turbulent pressure, models with higher values of c will have correspondingly larger uncertainties. We see similar redshift dependence for model set 2A as in Model Group 1, but the model set 2B displays reverse behavior: increasing normalization with redshift, although the uncertainties are so large as to make firm statements difficult. Possibly, the steep dependence on turbulent pressure overwhelms the general mass dependence, so that even though the clusters are in general smaller (leading to a lower normalization), the most massive cluster (which is used to fix the relation) maintains strong turbulence, negating this.

For Model Group 3 we see that exchanging a for c in the radio power model does lead to small differences in the slope and normalization. When we set $c = 0$ (so that there is no dependence on turbulent pressure) we essentially eliminate the uncertainties. The small differences are due to the fact that our scaling relation between Γ_v and M_v is only a best-fit approximation, and that scatter in that relation can affect the resulting $P_{1.4\mathrm{GHz}} - M_v$ relation. All the points, however, are within 2σ of each other. All these models show identical redshift dependence.

We see the drastic effects of changing the assumed average magnetic field in Model Group 4. Higher magnetic fields lead to higher normalizations and flatter slopes. However, the redshift evolutions exhibit opposite trends, such that at $z = 0.5$ the effects of the magnetic field are indistinguishable from each other. For weak magnetic fields, the cosmic rays are dominated by their interactions with the CMB, and the equivalent pressure of the CMB increases with redshift, lowering the synchrotron power at higher z. For strong fields, the dependence on cluster mass is more explicit, and at higher redshifts the clusters are, in general, smaller and the mass distribution has a steeper slope.

In Model Group 5 we see that the dependence on the scalings overwhelms the dependence on the average magnetic field. Even though model set 5A has the same $\langle B \rangle$ as set 4A, the dependence on b, a, and c forces the slope to the opposite end of the graph. Thus we may conclude that the effects of average magnetic field are degenerate with the scaling parameters, although the parameters taken individually can lead to significant differences. Similar behaviors are displayed

by Model Group 6, although the error bars are so small because of the weak dependence on the turbulent pressure.

In Figure 2.7 we repeat the above analysis for the $P_{1.4} - L_x$ relation:

$$\log\left[\frac{P_{1.4}}{3.16\times10^{24}h_{70}^{-1}\,\frac{\mathrm{W}}{\mathrm{Hz}}}\right] = Af\log\left[\frac{L_x}{10^{45}h_{70}^{-1}\,\frac{\mathrm{ergs}}{\mathrm{s}}}\right] + bf. \tag{2.8}$$

We find similar behaviors as in the $P_{1.4\mathrm{GHz}} - M_v$ relation plots above, except that our error bars are generally larger due to scatter from our estimates of L_x. Since X-ray luminosities are generally easier than virial masses to compute from observations, observations of many more radio halos may reduce the statistical uncertainties to such a level as to potentially distinguish the allowed scalings and dependencies. The redshift evolution of the $P_{1.4} - L_x$ relation especially may provide a way of determining the dominant components of radio power and the average magnetic strength of clusters, as we have discussed above for the $P_{1.4} - M_v$ relation..

In general, if the observational uncertainties in Af and bf are reduced by approximately a factor of two, many degeneracies in the model parameters will be eliminated. We note that we are basing this analysis on our sample of only 131 clusters. While this is significantly more than the current known number of radio halos, it is still far fewer than we expect to see with instruments such as LOFAR, as we will see below. While more objects could reduce the uncertainty, the precise amount of error also depends on the intrinsic scatter in the observed relations, which can be affected by biases. We also assume a power-law relationship holds between radio power and cluster mass even to low-mass clusters, which may not be the case once significant numbers of low-luminosity halos are detected.

2.6 Luminosity functions and radio halo counts

We now turn to a discussion of these models in terms of total counts of all objects in the simulation. To do this, we must assign a rest-frame radio luminosity to each cluster in the simulation box, even if it is not at high resolution. To do this we will combine the derived $P_{1.4} - M_v$ relations described above with a relationship between M_v, which includes gas, and $M_{v,\mathrm{DM}}$, which only includes dark matter. Our smallest clusters are only a few zones across and thus do not contain enough gas zones to accurately capture the contribution of the gas to M_v. However, we defined our minimum resolvable mass so that we can always get reliable evaluations of $M_{v,\mathrm{DM}}$ (i.e., $R_v \geq \Delta x,$, where Δx is the resolution of our pre-refinement uniform grid).

We find a very tight correlation between M_v and $M_{v,\mathrm{DM}}$ for our high-resolution sample, as shown in Figure 2.8. We fit a line to these data and

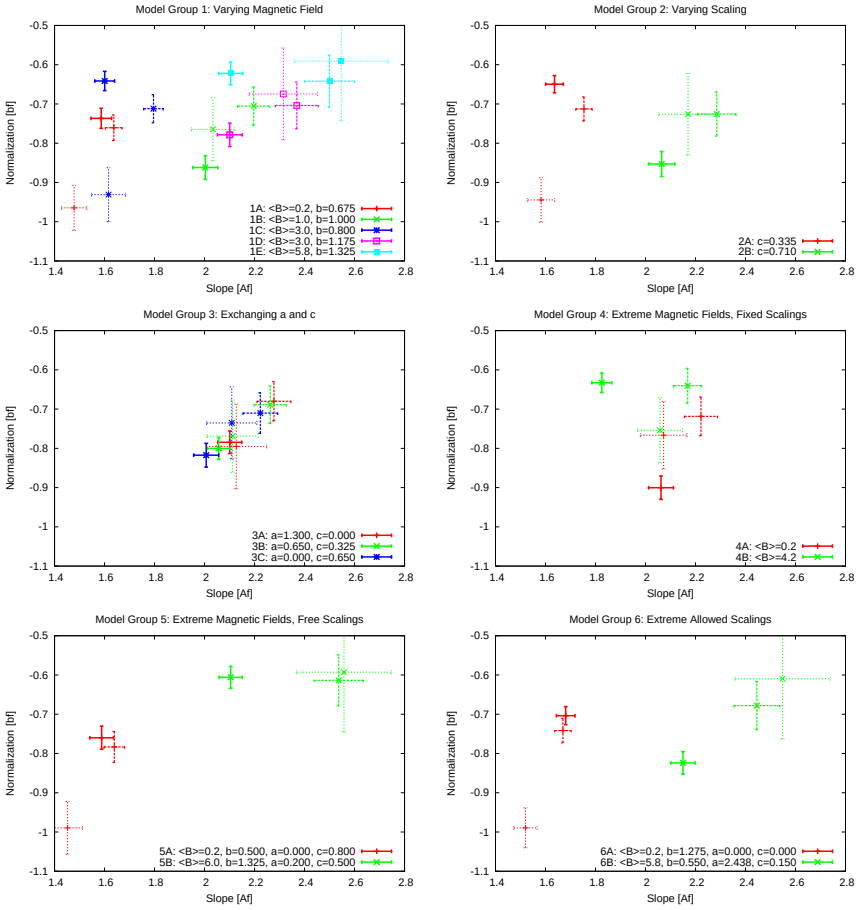

Figure 2.7: Best fits for the $P_{1.4} - L_x$. relation for each radio halo parameter set. Methods and colors are identical to Figure 2.6 We have identified each model with its designation from Table 2.2 and the portions of the model that change in the given Model Group.

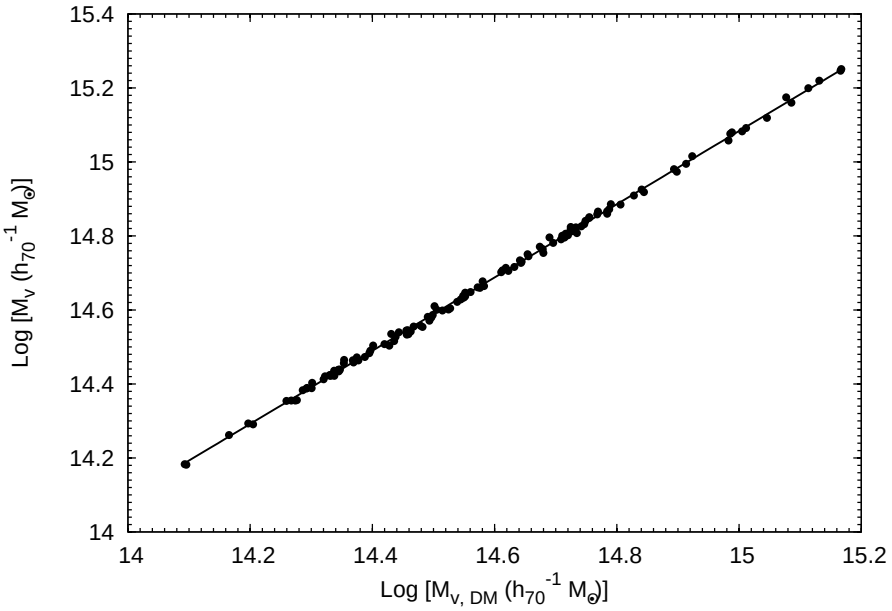

Figure 2.8: Data for (points) and best fit to (solid line) the M_v - $M_{v,\mathrm{DM}}$ relation.

found the correlation to be

$$\log\left[\frac{M_v}{10^{15}\ h_{70}^{-1}\ \mathrm{M}_\odot}\right] = 0.99\log\left[\frac{M_{v,\mathrm{DM}}}{10^{15}\ h_{70}^{-1}\ \mathrm{M}_\odot}\right] + 0.08. \tag{2.9}$$

This relationship implies a uniform gas fraction consistent with other simulations (e.g., Stanek et al. 2010). We use this fit to extract an M_v for each fixed-resolution cluster (i.e., those outside the refinement regions) which is then used to compute its equivalent radio power using the $P_{1.4} - M_v$ relation. While equivalent to directly interpolating from an $P_{1.4} - M_{v,\mathrm{DM}}$ relation, we found that this procedure produces less scatter and hence more reliable interpolations. Note that we do *not* add additional scatter to the interpolation procedure. For the analysis below we will include Poissonian uncertainty where appropriate, and this dwarfs any uncertainty introduced by scatter. By binning our data for luminosity functions, the main effect of scatter that we have in the $P_{1.4} - M_v$ relation is to simply move clusters around within a given luminosity bin, and any clusters that are scattered into a luminosity bin are roughly offset by clusters scattered out of the same bin.

Not every cluster hosts a radio halo, and for simplicity we will only assign radio halos to 1/3 of our clusters. We do this because we do not have enough high-mass ($> 10^{15}\ h^{-1}\ \mathrm{M}_\odot$) halos to calibrate our number counts based on the intrinsic scatter in our derived $P_{1.4\mathrm{GHz}} - M_v$ relation. More sophisticated techniques to calibrate number counts exist, such as using the synchrotron break frequency, ν_b, which is used in the identification of radio halos (see CBS06 for a discussion). However, again we do not have enough high-mass objects to use this

approach. With enough high-mass halos, the precise calibration would depend on our choice of parameters $\langle B \rangle$, b, a, and c. Thus we may be over-counting the number of radio halos at 1.4 GHz. However, we can still gather useful results as to the relative effects of varying radio halo models. Also, our analysis will include results at 150 MHz, where ν_b is much lower and hence our results are more valid. To calculate the radio luminosity at 150 MHz, we assume a simple power law with spectral index 1.2. Note that our smallest resolvable cluster has a 1.4 GHz radio luminosity of $\sim 2 \times 10^{21}$W/Hz.

Figure 2.9 shows our calculated radio halo luminosity functions at redshift $z = 0.0$ at 1.4 GHz and 150 MHz. For Model Group 1, in which we fix the dependence on cluster mass and turbulent pressure but vary the average magnetic field strength and scaling of magnetic field with cluster mass, we see a bifurcation in the luminosity function at low luminosities along the lines of the division seen above in the best fits to the $P_{1.4\mathrm{GHz}} - M_v$ relation: models with $b < 1.0$ produce up to a factor of two more low-luminosity radio halos than those models with $b > 1.0$. The distinction is much more significant at 150 MHz, where more objects allow for smaller uncertainties. However, despite difference in the $P_{1.4\mathrm{GHz}} - M_v$ relations, models 1A and 1C are indistinguishable from each other, as are models 1B, 1D, and 1E. Thus the number counts at low luminosity are reduced significantly when the magnetic field scaling b is greater than unity. At 1.4 GHz, the models are largely indistinguishable, with the exception of model set 1E, which includes a very strong average magnetic field. This model is the only one able to produce some radio halos with 1.4 GHz luminosity $\sim 10^{25}$ W/Hz.

We see in Model Group 2, in which we keep the magnetic field values fixed, that steeper scalings with turbulent pressure produce many more radio halos at both 1.4 GHz and 150 MHz. The 1.4 GHz halos are only statistically distinguishable at low luminosities, but the 150 MHz halos are easily separable throughout almost the entire range of radio luminosities. Similar conclusions can be made regarding Model Group 4, which brackets the extreme allowed magnetic fields with fixed scalings, where strong differences in the assumed average magnetic field strength lead to distinguishable differences. These behaviors persist for Model Groups 5 and 6, in which all parameters are allowed to vary, with the general rule being that it is difficult to separate these models when only relying on 1.4 GHz halo counts. The only models that remain inseparable are those in Model Group 3, in which our exchanges of a and c lead to degenerate radio halo counts at both frequencies, as expected.

As we move to higher redshifts, as in Figure 2.10 for $z = 0.25$ and Figure 2.11 for $z = 0.5$, we see the expected depletion of high-luminosity objects, especially at 1.4 GHz. However, some models are still distinguishable at 150 MHz even at redshift 0.5, although the large uncertainties make comparisons difficult. Models which have high scaling indices, such as model sets 2B and 6B, produce almost no radio halos even at 150 MHz at high redshifts.

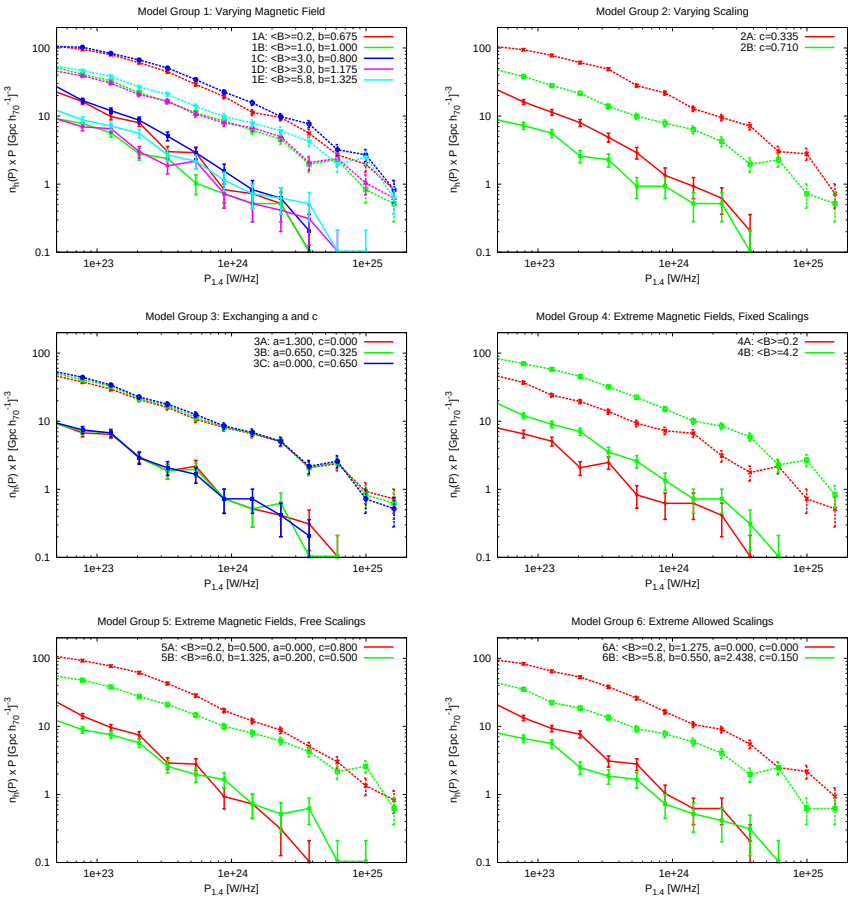

Figure 2.9: Radio halo luminosity functions at $z = 0.0$. Solid lines are luminosity functions at 1.4 GHz and dashed lines are at 150 MHz. Error bars indicate 1σ Poisson uncertainties. We have identified each model with its designation from Table 2.2 and the portions of the model that change in the given Model Group.

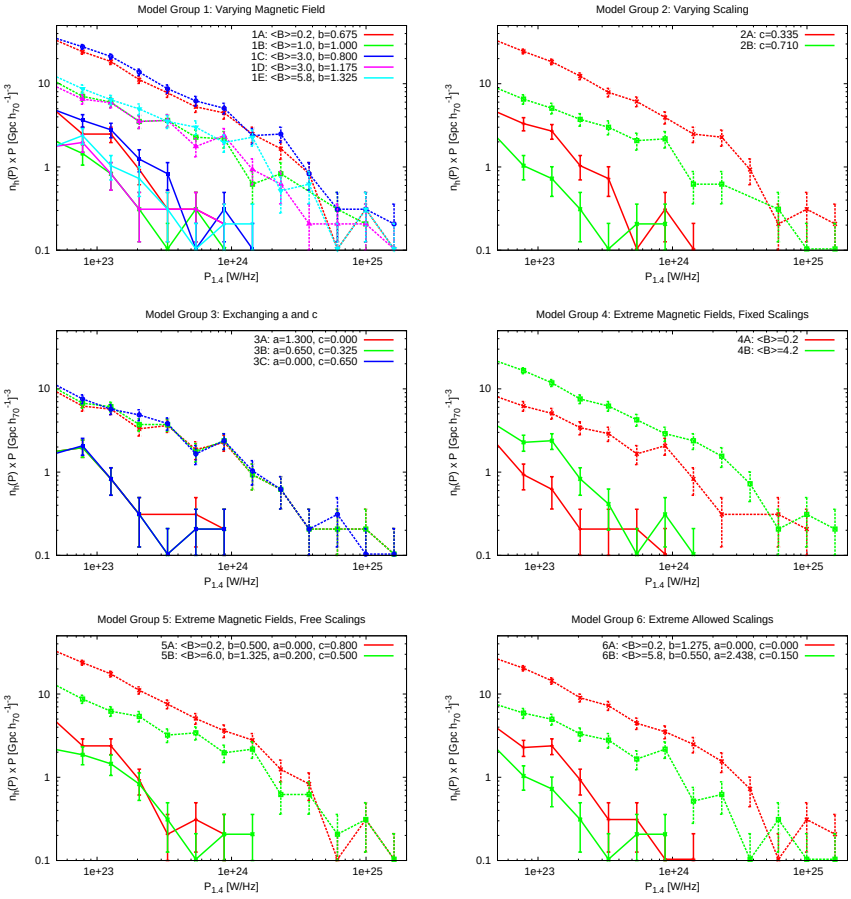

Figure 2.10: Radio halo luminosity functions at $z = 0.25$. Solid lines are luminosity functions at 1.4 GHz and dashed lines are at 150 MHz. Error bars indicate 1σ Poisson uncertainties. We have identified each model with its designation from Table 2.2 and the portions of the model that change in the given Model Group.

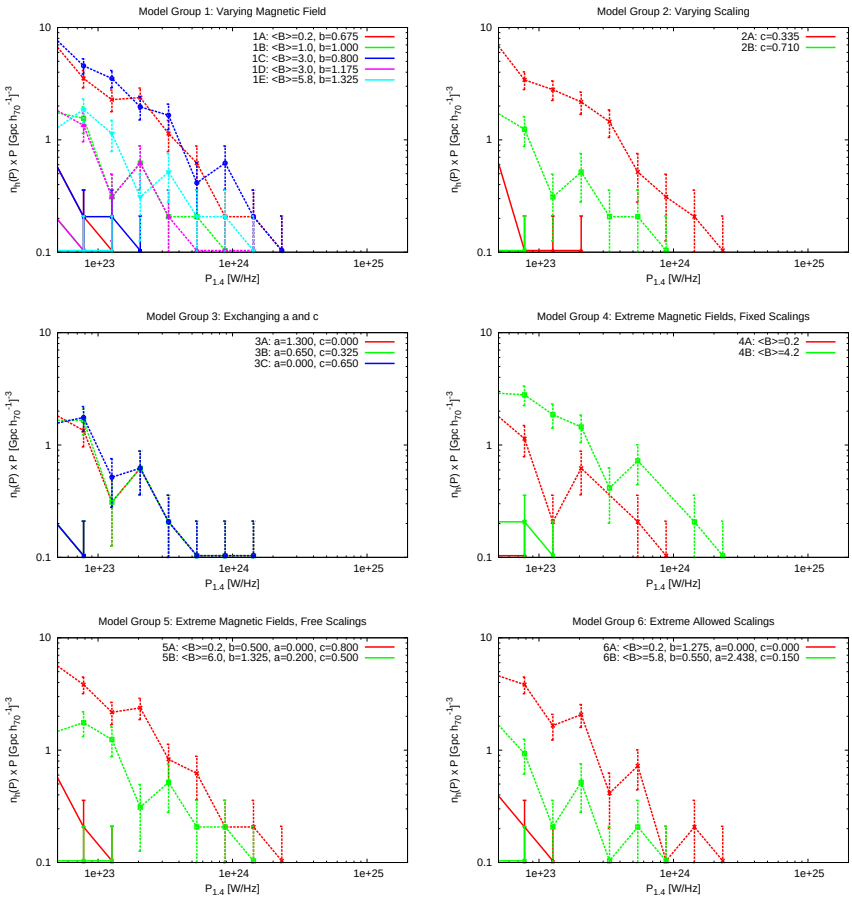

Figure 2.11: Radio halo luminosity functions at $z = 0.5$. Solid lines are luminosity functions at 1.4 GHz and dashed lines are at 150 MHz. Error bars indicate 1σ Poisson uncertainties. We have identified each model with its designation from Table 2.2 and the portions of the model that change in the given Model Group.

To accumulate total and binned counts we set a vantage point in the center of our computational domain and find halos whose locations lie on the light cone emanating from this position. To do this we use our saved checkpoint files from $z = 0.0$ to $z = 1.0$. Moving outwards in small ($\Delta z = 0.05$) redshift slices covering the same range, we locate the nearest output (in redshift) to each slice and use the center-of-mass peculiar velocities of the clusters found in that output to estimate new positions in the slice under consideration. We then compute the flux as $P/(4\pi d_L^2)$, where d_L is the luminosity distance of the cluster. We do this at both 1.4 GHz and 150 MHz.

We begin with Figure 2.12, where we show the total counts of radio halos at 1.4 GHz and 150 MHz in the entire universe as a function of flux limit in mJy. We assume Poisson uncertainties in the number counts. Although this is not entirely correct, since we are counting a population and not a sample, these number counts are extrapolated from our limited simulation volume, and hence this is a reasonable estimate of the uncertainties intrinsic to this approach, i.e. an estimate of fluctuations due to cosmic variance. Our number counts are bound by the resolvability limit of our simulation. While the model trends continue from the above analysis, we find that at high flux limits (> 100 mJy) and high frequencies, we are still able to strongly distinguish several models, specifically those with large discrepancies in either assumed average magnetic field or scalings with virial mass or total turbulent pressure. The exceptions are Model Groups 5 and 6, in which the suppression of radio halos at high redshift means that the integrated counts depend most strongly on high-luminosity objects, where the counts are nearly the same. At 150 MHz and an assumed LOFAR sensitivity limit of 30 mJy, we find an almost factor of two difference in the total counts between some models, such as model sets 2A and 2B.

In Figure 2.13 we show the total counts of radio halos within redshift $z < 0.2$ at 1.4 GHz and 150 MHz. This redshift range fits largely within our computational volume without the need for interpolation from older checkpoints and is more easily accessible to observers. We find little degradation in the total number counts in the LOFAR-accessible regime (> 20 mJy), and most models remain distinguishable, especially models that differ in the average magnetic field strength.

To conclude, we examine binned radio halo counts as a function of redshift in Figure 2.14. We examine five redshift bins equally spaced from $z = 0.0$ to $z = 0.5$. We see that the 1.4 GHz counts for all models are strongly peaked at low redshift and drop rapidly with increasing redshift, limiting their usefulness for distinguishing models. However, some models, particularly those with small a and c scaling parameters, are able to maintain some radio halos at modest ($z \sim 0.25$) redshift. On the other hand, the 150 MHz distribution is much smoother across the redshift bins, with most models producing roughly twice as many objects at low redshift than at high redshift. We note that separate models maintain their differences out to high redshift.

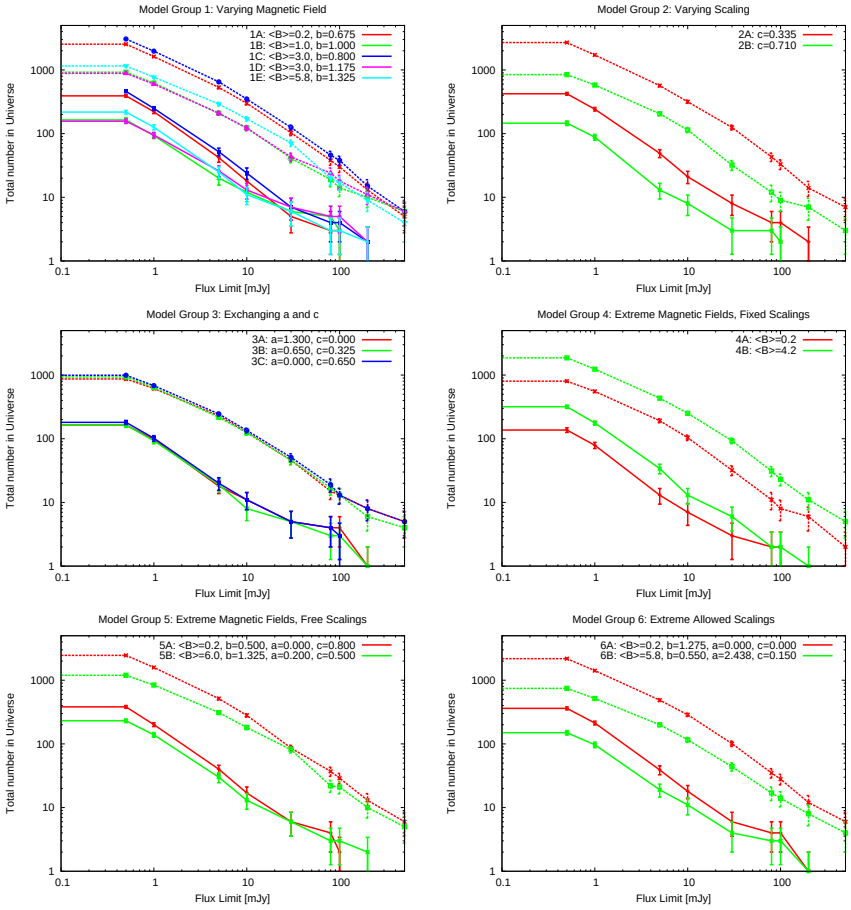

Figure 2.12: Radio halo total counts at 1.4 GHz (solid lines) and 150 MHz (dotted lines) versus flux limit in mJy. Error bars indicate 1σ Poisson uncertainties. We have identified each model with its designation from Table 2.2 and the portions of the model that change in the given Model Group.

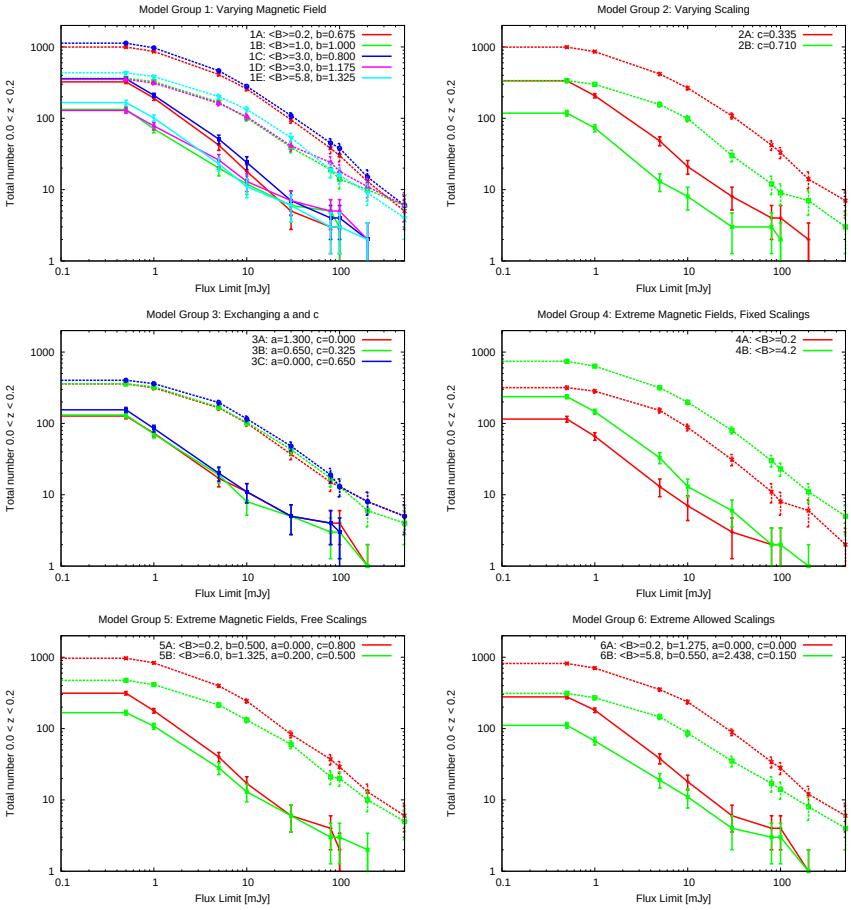

Figure 2.13: Radio halo counts for $z < 0.2$ at 1.4 GHz (solid lines) and 150 MHz (dotted lines) versus flux limit in mJy. Error bars indicate 1σ Poisson uncertainties. We have identified each model with its designation from Table 2.2 and the portions of the model that change in the given Model Group.

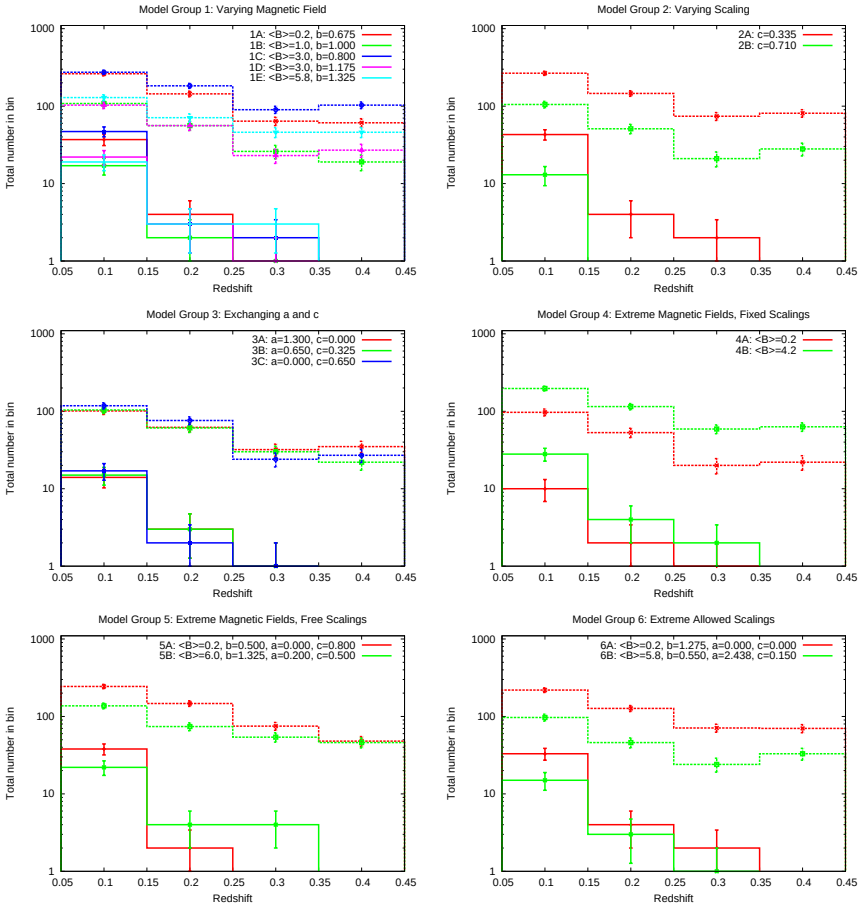

Figure 2.14: Radio halo binned counts at 1.4 GHz (solid lines) and 150 MHz (dotted lines) assuming a 5 mJy flux limit as a function of redshift. Each redshift bin has width $\Delta z = 0.1$. Error bars indicate 1σ Poisson uncertainties. We have identified each model with its designation from Table 2.2 and the portions of the model that change in the given Model Group.

2.7 Simulated radio sky maps

We generate raw mock sky maps in the $20 - 240$ MHz LOFAR bandpass by following a similar strategy of interpolating and redshift-correcting clusters as used above. Appropriate cosmological dimming and redshift are then applied to determine the contribution of the slice to the sky observed at $z = 0$. We generate a radio image for each cluster by projecting its density and turbulent pressure onto the skymap and computing the relevant radio intensity using a given set of radio model parameters, ensuring that the integrated radio power across the projected cluster is equal to the value obtained using M_v and Γ_v in the above sections. We only project gas values within R_v. For halos not within the high-resolution sample, we identify the nearest high-resolution cluster in mass and copy that high-resolution image to the location of the low-resolution halo. While this procedure is admittedly somewhat crude, it does allow us to explore some of the observational consequences of these models and demonstrates a method of generating radio maps in the future using more sophisticated and realistic simulated data.

Figure 2.15 shows the entire radio sky containing our simulated clusters at 120 arcsecond resolution assuming no background (i.e., a threshold sensitivity of 0 mJy). This resolution best approximates the LOFAR beam at an average frequency of ~ 120 MHz and a longest baseline of $L \sim 2$ km. For this example we have chosen model parameter set A1. This map particularly highlights the paucity of radio halos in the universe, even at low sensitivity thresholds, but it is useful for providing a mock all-sky map for linking simulations to observations.

Figure 2.16 highlights a region of the sky 6 degrees on a side at a resolution of 10 arcseconds, representing the high-resolution capability between 20 and 240 MHz at the longest baseline configuration of LOFAR. We also draw contour levels at varying sensitivities: 1, 10, and 30 mJy. These sensitivities represent different configurations of the LOFAR array. At high resolution and peak sensitivity, we are able to clearly distinguish several substructures and features within the two radio halos, indicating that LOFAR may be able to cleanly distinguish various radio power models based on their dependence on local gas density or local turbulent pressure, which can have different characteristic structures in the cluster atmosphere (Figure 2.3). At lower sensitivities, we can still distinguish features in the cluster cores, and early LOFAR images of nearby and bright radio halos may also provide useful distinguishing results.

Figure 2.17 shows the same region of the sky as above with a much lower resolution of of 240 arcseconds. The contours are the same as above. While we lose significant information about distant and small clusters, some larger clusters, such as the one shown, still show significant structure even at lower resolutions. We see that we can still identify substructure within the large cluster, and the effects of higher sensitivity thresholds are limited to distant clusters and the outer regions of nearby objects. These results are encouraging,

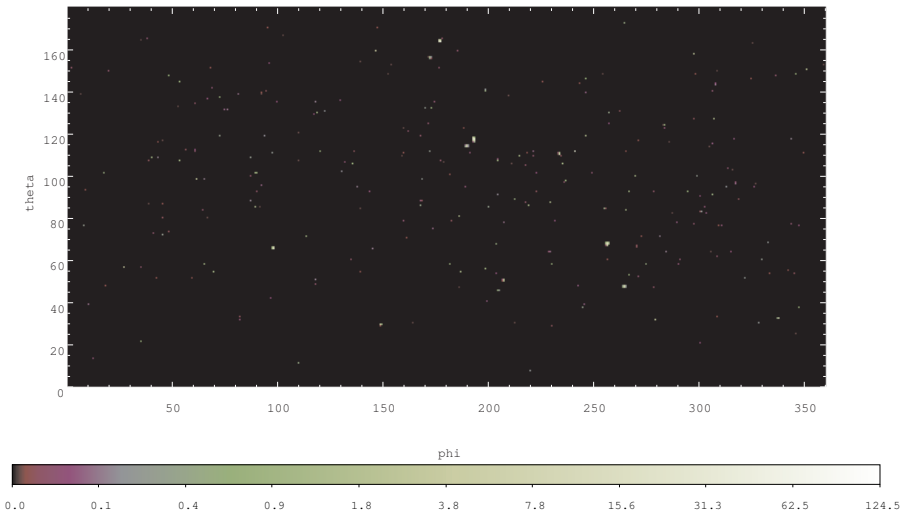

Figure 2.15: Example radio halo all-sky map. This map assumes 0 mJy sensitivity threshold and a resolution of 120 arcseconds. The color scale is the logarithm of radio power in mJy.

since they indicate that LOFAR may be able to give detailed radio maps of many radio halos.

2.8 Conclusions

We have introduced the first set of radio halo statistics derived entirely from large-scale cosmological simulation. Our radio power model is sufficiently broad to encompass many viable and more realistic models of cosmic ray generation and synchrotron emission in clusters of galaxies. Our approach demonstrates the viability of using large-scale simulation to bridge simulations and observations, both by deriving radio halo statistics from the simulated data to constrain possible radio power models and by producing mock radio sky maps that can be directly compared to observations.

From our analysis we have determined that the slope and normalization of the $P_{1.4\mathrm{GHz}} - M_v$ and $P_{1.4} - L_x$ relations are potentially key probes of the various models of cosmic ray generation. They also allow us to place limits on the average cluster magnetic field strength and the scaling of magnetic fields with cluster mass. With the uncertainties from only 131 observed radio halos we can significantly constrain the scaling of radio power with cluster mass and turbulent pressure. With the 131 objects of our high-resolution sample we are able to clearly separate some models with strong statistical significance. The evolution with redshift of these relations also allows us to potentially distinguish various models.

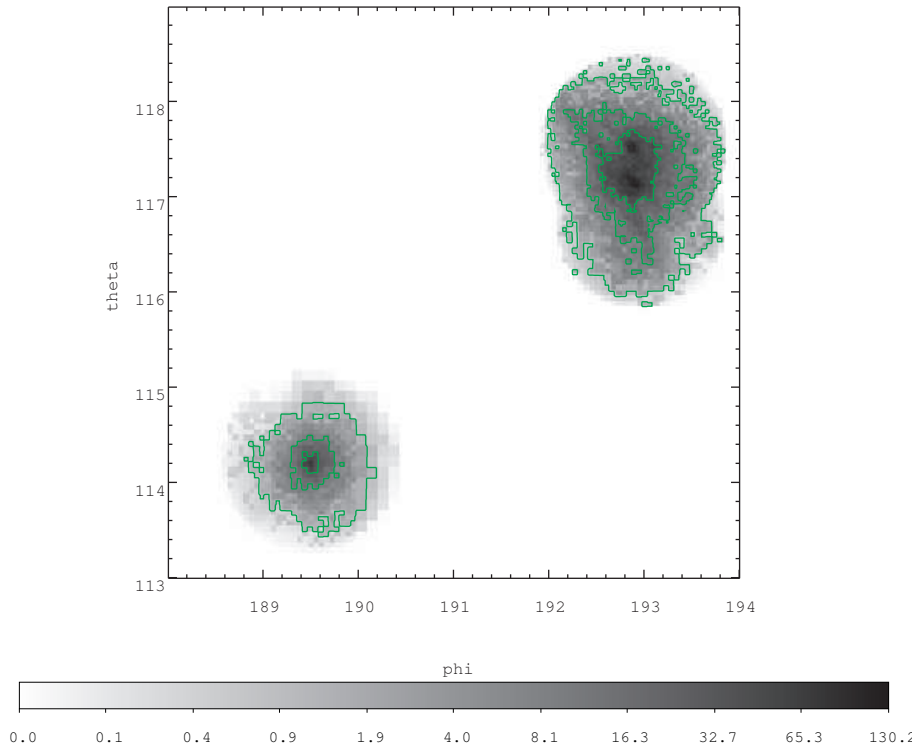

Figure 2.16: Example radio halo partial-sky map at 10 arcsecond resolution. The color scale is the logarithm of radio power in mJy. Contours are drawn at 1, 10, and 30 mJy levels.

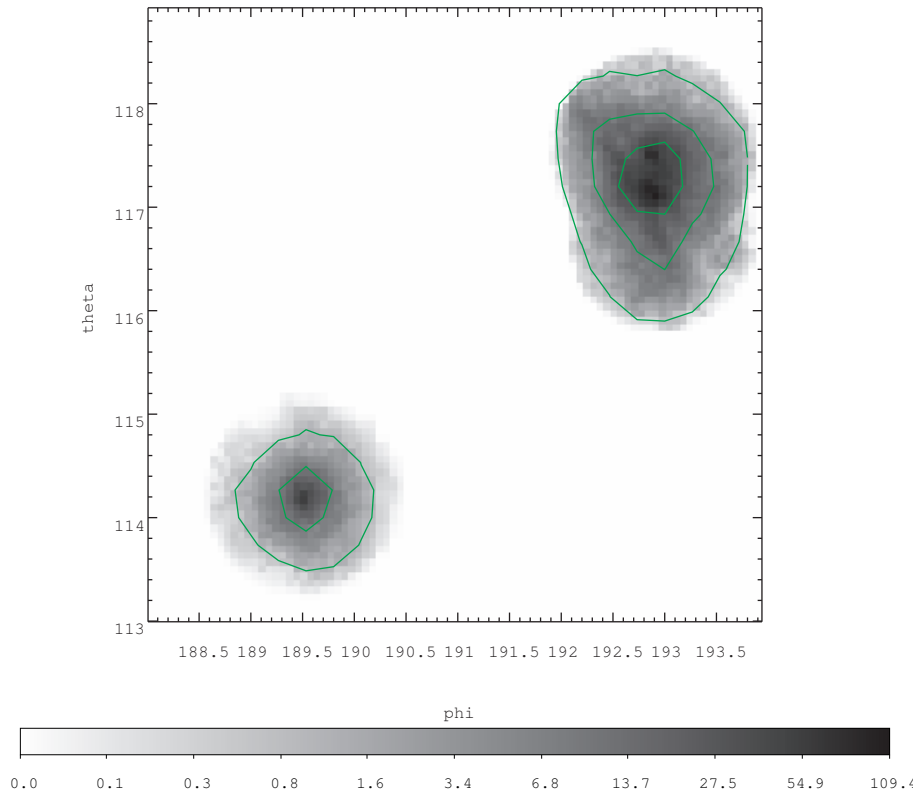

Figure 2.17: Example radio halo partial-sky maps at 240 arcsecond resolution. The color scale is the logarithm of radio power in mJy. Contours are drawn at 1, 10, and 30 mJy levels

We find similar radio halo luminosity functions as the analysis of Enß lin & Roettgering (2002), which combined the X-ray luminosity function with the observed correlation between X-ray luminosity and radio power. However, our limited volume prevents us from counting the very largest - and hence rarest - clusters. We predict many more high-frequency radio halos than the analysis of CSB06, since we do not include a calculation of the synchrotron break frequency, ν_b, to calibrate high-luminosity number counts but rather just assign a radio halo to 1/3 of our clusters, since we did not have enough high-mass halos to reliably use this technique. However, at lower frequencies we obtain roughly similar number counts, since these number counts are less sensitive to calibrations at the high-mass end. While our model is intended to include the prescription of CBS06, we find that we cannot study their exact parameters because we force our models to agree with the observed $P_{1.4\mathrm{GHz}} - M_v$ relation to lower masses than in CBS06, and consequently their particular model is ruled out. However, we reach similar conclusions about the relationship between cluster mass and magnetic field strength.

However, we have uncovered some degeneracies among the scalings of radio power with cluster mass and turbulent pressure and the mass-dependence of cluster magnetic fields. These degeneracies can be broken by several methods. For example, a better understanding of the relationship between cluster mass and magnetic field will constrain our $\langle B \rangle$ and b parameters, allowing us to make more conclusive statements about the observational limits placed upon the a and c parameters. On the other hand, more high-resolution radio and X-ray images of clusters may constrain the effectiveness of the various mechanisms of generating cosmic rays, which would further constrain our a and c parameters.

We find that low-frequency observations are especially important for distinguishing and constraining the scaling of radio power with cluster mass and turbulent pressure, since the radio halo number counts are much higher at lower frequencies. These counts are sufficiently high at the expected LOFAR sensitivities that statistical uncertainties become small enough to clearly separate models. The redshift dependence of number counts and luminosity functions especially may become a crucial method of identifying models, and these high redshift - and correspondingly low flux - objects are only accessible by LOFAR and future large-scale radio arrays. Radio observations are especially important since the gamma ray emission associated with the production of cosmic rays from hadronic secondary interactions from clusters might be too small for FERMI to detect, which means that we may not be able to use this instrument to distinguish models (Brunetti 2009).

Similarly, since hadronic secondary models of cosmic ray production are highly degenerate with re-acceleration models when only considering total counts and integrated cluster quantities, high-resolution radio images are required in order to effectively distinguish these models.

Our simulated radio cluster and sky maps are freely available upon request to

the authors or via `http://sipapu.astro.illinois.edu/foswiki/bin/view/Main/RadioHaloMaps`. We have produced images at a variety of sky coverage areas, sensitivity limits, and resolutions for all of the models described above. These images are simple `FITS` files. The images are straightforward to produce, allowing us to explore further refinements to the models and more sophisticated instrument modeling.

Since this initial work is highly preliminary, we have room for many improvements and modifications to make stronger connections with observations. As an immediate improvement we may perform simulations with larger volumes than our 1 h^{-1} Gpc box in order to capture more massive objects. With larger volumes we can also capture more low- and moderate-mass objects to obtain better statistics for the $P_{1.4\mathrm{GHz}} - M_v$ and other relations. With more simulations, we may begin to investigate the dependence of radio halo counts on cosmological parameters. We may also begin to self-consistently include magnetic fields, although our results in this approach would be tied to a specific model of magnetic field injection and growth. Similarly, we can begin to investigate generating and propagating cosmic rays in the simulation, although it is difficult to scale current methods to large volumes and high resolutions. However, our results demonstrate an important first step in bridging simulations and observations to more fully understand the large-scale radio universe.

Chapter 3

Injecting magnetic fields into clusters of galaxies via active galactic nuclei

3.1 Introduction

Radio observations of clusters of galaxies indicate that they host large-scale, volume-filling diffuse magnetic fields of strength $0.1 - 10\mu$G, while additional rotation measure observations suggest that these fields are tangled with auto-correlation lengths of 10-20 kpc (see Carilli & Taylor (2002) for a review) and have complex topology (Falceta-Gonçalves et al. 2010b). These fields are extremely important in understanding cluster astrophysics: they provide a source of non-thermal pressure support (Dolag & Schindler 2000), allow for synchrotron emission from cosmic rays (Miniati et al. 2001; Pfrommer et al. 2007; Brunetti et al. 2007; Skillman et al. 2008), potentially suppress or modify thermal conduction (Ruszkowski & Oh 2010; Parrish et al. 2009), and modify turbulence in the cluster atmosphere (Narayan & Medvedev 2001; Chandran & Maron 2004; Shukurov et al. 2006). However, despite their ubiquity and importance we do not at present understand their origins and evolution or the precise correlations of these fields with other cluster properties.

While exotic processes in the early universe may generate these large-scale fields (e.g., Baym et al. 1996; Bamba et al. 2008; Battefeld et al. 2008), magnetic fields may have difficulty surviving the radiation-dominated era due to very high diffusion rates (Lesch & Birk 1998). Alternatively, we may turn to astrophysical mechanisms, and especially active galactic nuclei (AGN), for seeding and amplifying magnetic fields. In this scenario, weak seed fields ($\sim 10^{-18}$ G) are generated via a plasma process, such as the Biermann battery mechanism (Biermann 1950; Widrow 2002). Dynamo action in supermassive black hole (SMBH) accretion disks can quickly amplify these weak fields which then launch jets (Koide et al. 1999). The jets can propagate tens of kiloparsec into the intracluster medium (Kirkpatrick et al. 2011) and inflate bubbles (Colbert et al. 1996). The bubbles rise into the intracluster medium (ICM) and eventually disperse, distributing heat (Voit & Donahue 2005) and potentially magnetic fields within cluster cores. AGN outflows are more than powerful enough to match the ob-

served magnetic energy in clusters (Colgate & Li 2000) and are natural carriers of magnetic flux (Daly & Loeb 1990). Rotation measure observations of jets indicate the presence of magnetic fields in them (Contopoulos et al. 2009). AGN feedback is also a strong candidate for preventing excessive cooling in cluster cores (McNamara & Nulsen 2007).

However, the complex physics of AGN accretion disks and jets coupled with the small scales involved (~ 100 pc) makes it difficult to include AGN in cluster and cosmological simulations, which typically resolve scales greater than 2 kpc. Thus, we must include the accretion and feedback processes as subgrid models. Subgrid models have been developed and employed by many authors with varying levels of sophistication. Accretion rate calculations can vary from the simple Bondi rate (Bondi 1952) to stochastic models (Pope 2007). If the resolution and computing resources permit it, large-scale jets can be placed on the simulation grid with many modifications, including simple fluxes at cell boundaries (Gaspari et al. 2011), limited-lifetime jets (Morsony et al. 2010), extended jets (Cattaneo & Teyssier 2007), wide-angle jets (Sternberg et al. 2007), and precessing jets (Falceta-Gonçalves et al. 2010a). Since jets eventually inflate bubbles, it is easier computationally to simply place already-formed bubbles (e.g., Sijacki et al. 2007; Gardini 2007; Di Matteo et al. 2008; Booth & Schaye 2009) or to slowly inflate them (e.g., Jones & De Young 2005). Whereas jets continuously feed back energy and momentum onto the simulation grid, bubbles are modeled as discrete events.

All of the above models have been discussed using purely hydrodynamic simulations. While there has been some research into the effects of AGN-driven turbulence in a magnetized cluster (Dubois & Teyssier 2008), magnetized outflows themselves have only been studied by a few authors. The stability of AGN-blown bubbles with a predetermined magnetic field configuration has been somewhat well examined (e.g., Robinson et al. 2004; Jones & De Young 2005; Ruszkowski et al. 2007; Xu et al. 2008a; Gourgouliatos et al. 2010). Additionally, Xu et al. (2010) have followed the evolution of magnetized bubbles in the cosmological formation of a large cluster. However, no simulations of magnetized AGN outflows have included feedback processes coupled to their surroundings, i.e. these studies have presumed a fixed energy in the magnetized bubbles. This link between the feedback energy and the accretion rate is essential in order to reproduce the observed cosmic SMBH mass density (Hopkins et al. 2006) and the correlation between SMBH mass and galactic bulge velocity dispersion (Booth & Schaye 2009). Furthermore, there has been no systematic comparison study of the various models of AGN feedback when magnetic energy is included (see our companion paper, Yang et al. (2011), for a comparison study of purely hydrodynamic outflows).

In this work, we will use FLASH MHD simulations of a mock isolated cluster to examine several different AGN subgrid models, exploring variations of their parameters for a variety of resolutions (we have independently studied subgrid

models of SMBH formation and merging in Sutter & Ricker (2010)). Since we cannot perform an exhaustive study of all the models presented above, we will select a representative bubble model (Sijacki et al. 2007) and a representative jet model (Cattaneo & Teyssier 2007). We will add the magnetic field injection model of Li et al. (2006). We will perform a systematic study of these models by varying some of the parameters available for each model in otherwise identical simulation setups. Note that for this study, we will not evaluate the models in terms of their respective abilities to reproduce cluster observables; our goal in this manuscript to take the models as read in their respective papers and apply magnetic injection to them. By choosing jet and bubble models we will be able to compare and contrast continuous, centrally located small-volume injections (jets) with sporadic, randomly located large-volume injections (bubbles). We will also vary the parameters associated with accretion rate models, since these are tightly coupled to the feedback properties and hence the resulting magnetic field. We choose to simulate both bubble and jet models because they are very distinct: they differ in the form of injected hydrodynamic energy, the shape of the injection region, and the periodicity of feedback events. These two approaches allow us to bracket a wide range of plausible feedback models and explore the roles that their injected magnetic fields can play in the evolution of their host clusters.

We have three main goals in this work: to examine the effect that introducing magnetic fields into the AGN injection region has on the accretion and feedback properties of the SMBH, to evaluate the ability of the various studied models to magnetize an initially unmagnetized cluster, and to examine the robustness of these models to changes in their subgrid parameters. We will characterize the resulting magnetic fields in terms of field morphology, growth rates, and radial profiles. We begin with a discussion of our simulation code and mock cluster setup in Section 3.2 and a description of the subgrid models we study in Section 3.3. We examine the role that magnetic fields play in modifying the feedback properties of the modeled AGN in Section 3.4 and the ability of our fiducial jet and bubble models to magnetize a cluster in Section 3.5. We then examine the magnetic topology of the produced fields for the fiducial runs via streamlines and rotation measure maps in Section 3.6. Finally, we perform a parameter survey in Section 3.7. For this survey, we will focus mainly on the changes to the accretion rate and magnetic properties of the outflows. We conclude and offer recommendations for constructing reliable subgrid models in Section 3.8.

3.2 Numerical approach

Using the adaptive mesh refinement code FLASH 3.3 (Fryxell et al. 2000; Dubey et al. 2008), we performed three-dimensional magnetohydrodynamic simulations with radiative cooling and AGN feedback within an isolated mock cluster sit-

ting in a 2048 kpc box. We constructed the mock cluster gas using an ideal-gas equation of state in hydrostatic equilibrium with an NFW gravitational profile (Navarro et al. 1996). We assumed a cluster mass of $1.5 \times 10^{14}\ M_{\odot}$, concentration 5.53, gas fraction 0.1, and Hubble constant $h = 0.65$. For computing accretion and feedback properties, we placed a $3 \times 10^{9}\ M_{\odot}$ black hole in the cluster center. Note that we do not include the black hole mass in the computation of the gravitational potential. We computed radiative cooling rates using the collisional ionization equilibrium tables of Sutherland & Dopita (1993) assuming 1/3 solar metallicity.

We maintained a minimum resolution of 32 kpc throughout the simulation volume and enabled progressive nested refinement centered on the black hole. We varied the peak refinement (see below) from 0.5 to 16 kpc. We defined the maximally-refined region as a box of width 80 kpc for jets and 160 kpc for bubbles.

3.3 Subgrid models

3.3.1 Accretion rate

The most basic component of the accretion model is the black hole mass. While this mass will change with time as gas accretes onto the SMBH, we must select an initial seed value. The accretion rate is strongly dependent on mass, and hence the the feedback energies in the early cluster evolution can vary greatly. Ideally, we would perform cosmological simulations and include the formation and evolution of black holes along with our simulated clusters (e.g., Booth & Schaye 2009; Sutter & Ricker 2010). Since we are simulating an already-formed mock cluster, we must select some value. While some authors (e.g., Sijacki et al. 2007) have placed low-mass ($\sim 10^{5}\ M_{\odot}$) black holes in massive clusters to study their growth, this is not consistent with the known $M_{\rm bh} - M_{\rm tot}$ relation (Bandara et al. 2009). We will choose a value consistent with an already-formed cluster, $M_{\rm bh} = 3 \times 10^{9}\ M_{\odot}$

For the purposes of this study, we will restrict our survey to the somewhat simple, but widely used, so-called α-model of estimating the SMBH accretion rate (see our companion paper, Yang et al. (2011), for an analysis of more sophisticated models). The α-model is a simple modification to the Bondi-Hoyle-Lyttleton (Bondi 1952) accretion rate:

$$\dot{M}_{\rm Bondi} = 4\pi G^{2} M_{\rm bh}^{2} \frac{\rho}{{c_{\rm s}}^{3}}, \tag{3.1}$$

where the sound speed $c_{\rm s}$ and the density ρ are measured on the simulation mesh, and $M_{\rm bh}$ is the black hole mass. This approximates well the observed accretion rate when the Bondi rate is measured at parsec scales (Allen et al. 2006). However, simulations of clusters and larger structures cannot obtain sufficient

resolution to reach these parsec scales, so we must include some compensating factor. If we assume that we are underestimating the true accretion rate at the scales we typically resolve, we can simply multiply the calculated Bondi rate by a constant:

$$\dot{M}_{\rm bh} = \alpha \dot{M}_{\rm Bondi}. \tag{3.2}$$

We are free to choose the value of α, and we will examine values from 1 (i.e., regular Bondi accretion) to 300, both at fixed resolution and by allowing the α parameter to scale with resolution, under the assumption that as we lower the resolution we must make greater enhancements to the calculated Bondi rate.

We must also choose the region in our simulation mesh where we will measure the density and sound speed for computing the accretion rate. While we may simply sample the immediate zones around the SMBH, this approach may suffer from undue variability, especially in the case of jet-based feedback where the primary effects of the feedback are felt in those same zones. However, if we choose too large a radius, we will poorly sample the gas properties and incorrectly estimate the accretion rate.

Similarly, we must remove gas from the simulation mesh as we accrete it onto the black hole. As before, we have the freedom to choose from where we will remove the gas. If we choose too small a depletion region, then in the case of strong accretion events we may potentially remove too much gas from the central zones, leading to numerical instability. On the other hand, removing gas from zones far away from the SMBH is clearly unphysical, since this gas does not actually accrete onto the black hole. To achieve a balance, many authors (e.g., Dubois et al. 2010) choose a minimum gas removal threshold so that the size of the depletion region is chosen to ensure that no more than some fraction of the gas in the depleted cells (for example, 10%) is removed in any one timestep.

Since the accretion rate is proportional to the gas density and the gas density is directly affected by our depletion mechanism, our choices for the accretion and depletion regions will influence each other and thereby the feedback properties of the AGN. We will include in our study a spherical region with radii 1 to 4 zones, varying the accretion and depletion radii jointly and separately. We will also maintain a maximum depletion fraction of 10% with the *minimum* depletion radius set as described above.

For all accretion models, we impose an upper limit on the accretion rate corresponding to the Eddington rate,

$$\dot{M}_{\rm Edd} = \frac{4\pi G M_{\rm bh} m_{\rm p}}{\epsilon_{\rm f} \sigma_{\rm T} c}, \tag{3.3}$$

where $m_{\rm p}$ is the mass of the proton, $\sigma_{\rm T}$ is the Thompson cross-section, and $\epsilon_{\rm f}$ is the radiative efficiency.

In Table 3.1 we summarize the parameters included in the accretion rate model and the values included in our survey: the initial black hole mass $M_{\rm bh}$,

Table 3.1: Parameters of the accretion rate model.

Parameter	Description	Value(s)
$M_{\rm bh}$	Initial BH mass ($M_\odot$)	3×10^9
α	Bondi multiple	$1 - 300$
$\dot{M}_{\rm max}$	Maximum accretion rate	$\dot{M}_{\rm Edd}$
$R_{\rm acc}$	Accretion radius (zones)	$1 - 4$
$R_{\rm dep}$	Minimum depletion radius (zones)	$1 - 4$
$f_{\rm dep}$	Maximum gas depletion fraction	0.1

the Bondi multiple α, the maximum accretion rate $\dot{M}_{\rm max}$, the accretion radius $R_{\rm acc}$, the minimum depletion radius $R_{\rm dep}$, and the maximum gas depletion fraction, $f_{\rm dep}$.

3.3.2 Jet-based feedback

We follow the general prescription of Cattaneo & Teyssier (2007) for building our jet-based feedback models. This particular model does not simulate the relativistic jet immediately after its launch from the AGN accretion system, which we do not have the resolution to accurately simulate, but rather the large-scale non-relativistic outflow as the jet extends to kpc scales and begins to entrain ICM material. This jet imparts thermal and kinetic energy to the ICM as well as a small amount of mass fed back from the accretion disk.

The injection rates of the mass, momentum, and energy onto the grid are treated as source terms in the hydrodynamic equations, where the energy injection rate is

$$\dot{E} = \epsilon_{\rm F} \dot{M}_{\rm bh} c^2 \left(1 - \eta\right) |\Psi|. \tag{3.4}$$

Similarly, the momentum injection rate is $\dot{\mathbf{P}} = \sqrt{2\epsilon_{\rm f}} \dot{M} c \Psi$, and the mass injection rate is $\dot{M}_{\rm inj} = \eta \dot{M} |\Psi|$. In the above, $\epsilon_{\rm f}$ is a feedback efficiency and η is the jet mass loading factor, which is a parameterization of the entrainment of gas as the jet propagates. A jet mass loading factor of $\eta = 1$ corresponds to the case in which there is no entrainment and the feedback energy is entirely kinetic. Higher values allow for the deposition of thermal energy.

The window function Ψ, which provides a mapping onto the mesh, is

$$\Psi(\mathbf{x}) = \frac{1}{2\pi r_{\rm ej}^2} \exp\left(-\frac{x^2 + y^2}{2r_{\rm ej}^2}\right) \frac{z}{h_{\rm ej}^2}. \tag{3.5}$$

We cut off injection at $z = h_{\rm ej}$ and $r = r_{\rm ej}$. Note that we normalize the injected energy within the window function by dividing Ψ by its integral $\|\Psi\| = 1 - \exp\left(-0.5 r_{\rm ej}^{-2}\right)$. The injection region is oriented along the z-axis. There is no threshold associated with activating jet feedback; the jet operates continuously, as suggested by observations (Peterson & Fabian 2006).

Note that our specific implementation has several differences from that of Cattaneo & Teyssier (2007). First, we normalize our value of Ψ. Subse-

Table 3.2: Parameters of the jet-based feedback model.

Parameter	Description	Value(s)
$\epsilon_{\rm f}$	Feedback efficiency	0.1
η	Jet mass loading factor	100
$h_{\rm ej}$	Jet height (kpc)	$2 - 16$
$r_{\rm ej}$	Jet radius (kpc)	$2.5 - 20$

quent papers based on the same model, such as Dubois et al. (2010), do this as well. Also, their model fixed the mass of the SMBH for purposes of calculating the accretion rate. For jets, this is a reasonable approximation, since the accretion rate does not reach high values. We also simulate a larger volume and maintain a larger maximally-refined central region. Furthermore, we use a smaller $R_{\rm acc}$ and allow depletion of gas from the ICM. When accounting for all these difference we have been able to match their results.

We fix, as with Cattaneo & Teyssier (2007), a value of $\eta = 100$ and $\epsilon_{\rm f} = 0.1$, which are chosen to match observed jet velocities. We vary the jet size, both exploring larger jets with fixed resolution and maintaining a fixed ratio of jet to grid size. While larger jets may be somewhat unphysical, in cosmological simulations we can only reach resolutions of $\Delta x \sim$ 2-4 kpc, and so this may be the only option available. While a jet height of 0 is a valid model, corresponding to a simple flux at a cell boundary, we will not study it here since we require some spatial extent for the injection of magnetic flux (see below).

Table 3.2 summarizes the aspects of the jet model and our chosen values: the feedback efficiency $\epsilon_{\rm f}$, the jet mass loading factor η, the jet height $h_{\rm ej}$, and jet radius $r_{\rm ej}$.

3.3.3 Bubble-based feedback

For bubble-based feedback we will follow the method outlined in (Sijacki et al. 2007), which places over-pressurized bubbles displaced from the SMBH location. In their model we have only thermal energy injection:

$$\dot{E} = \epsilon_{\rm m} \epsilon_{\rm f} c^2 \Delta M_{\rm bh}, \tag{3.6}$$

where $\Delta M_{\rm bh}$ is the increase in BH mass since the last bubble event, $\epsilon_{\rm f}$ is the feedback efficiency and $\epsilon_{\rm m}$ is the mechanical heating efficiency. We distribute this energy on a per-mass basis in a sphere with radius determined by

$$R_{\rm bub} = R_0 \left(\frac{\dot{E} dt}{E_0} \frac{\rho_0}{\rho} \right)^{1/5}, \tag{3.7}$$

where we define the radial scaling $R_0 = 30\ h^{-1}$ kpc, energy scaling $E_0 = 10^{55}$ ergs, and density scaling $\rho_0 = 10^4 h^{-2}\ M_\odot$ kpc^{-3}. These scalings are chosen to ensure that a bubble in a typical cluster environment will have a real-

Table 3.3: Parameters of the bubble-based feedback model.

Parameter	Description	Values(s)
$\Delta_{\rm bh}$	Minimum fractional BH mass increase	0.01%
$\epsilon_{\rm f}$	Feedback efficiency	0.1
$\epsilon_{\rm m}$	Mechanical heating efficiency	0.2
R_0	Radial scale (h^{-1} kpc)	30
E_0	Energy scale (ergs)	10^{55}
ρ_0	Density scale ($h^{-2}\ M_\odot$ kpc^{-3})	10^4
$R_{\rm dis}$	Maximum displacement of bubble center	$0.0 - R_{\rm bub}$

istic size when it has reached pressure equilibrium with the ICM, and we have used the same values as in the cosmological runs of Sijacki et al. (2007). Since bubble events are episodic, we must select some criterion for forming bubbles. We will only form bubbles when the black hole has increased its mass since the previous bubble formation by $\Delta M_{\rm bh}/M_{\rm bh} > 0.01\%$, which was chosen by Sijacki et al. (2007) to produce the observed $M_{\rm bh} - \sigma$ relation.

Since observed bubbles are displaced away from the cluster centers (.e.g., Voit & Donahue 2005), we will randomly place each bubble with a maximum displacement $R_{\rm dis}$ equal to the calculated bubble radius $R_{\rm bub}$. However, we will also examine the case in which we fix the bubble radius to 40 kpc and do not displace the bubble centers away from the central SMBH, as has been used in several cosmological simulations (e.g., Di Matteo et al. 2008; Battaglia et al. 2010). This setup should be an intermediate case between bubbles and jets.

In Table 3.3 we summarize our bubble model parameters and the values we will examine in our survey: the minimum black hole mass increase to trigger a bubble event $\Delta_{\rm bh}$, the feedback efficiency $\epsilon_{\rm f}$, the mechanical heating efficiency $\epsilon_{\rm m}$, the bubble radial scale R_0, the bubble energy scale E_0, the bubble density scale ρ_0, and finally the maximum displacement of the bubble center $R_{\rm dis}$.

As opposed to the jet feedback mechanisms, which as we will see maintain low accretion rates due to the continuous nature of the feedback, episodic bubble-based models can occasionally allow the accretion rate to reach large fractions of the Eddington rate. Indeed, observations indicate that the SMBH accretion rate is very high, at least at high redshift (Fan 2006). When the accretion rate, and hence the available feedback energy, reaches large values the feedback takes the form of pure radiation (Fender et al. 1999; Gallo et al. 2003). In this case, instead of mechanically inflating bubbles, the outflows from the AGN simply heat the nearby gas:

$$\dot{E} = \epsilon_{\rm f}\epsilon_{\rm r} c^2 \dot{M}, \tag{3.8}$$

where $\epsilon_{\rm f}$ is the feedback efficiency and $\epsilon_{\rm r}$ is the QSO heating efficiency. We must choose a threshold to switch to this feedback mode, and we follow Sijacki et al. (2007) with a value of $0.01\dot{M}_{\rm Edd}$. We are free here to choose our radius for depositing the energy, and for numerical stability we choose a feedback radius of 8 zones.

Table 3.4: Parameters of the quasar-based feedback model.

Parameter	Description	Value(s)
$\chi_{\rm radio}$	Two-mode feedback threshold	$0.01\dot{M}_{\rm Edd}$
$\epsilon_{\rm f}$	Feedback efficiency	0.1
$\epsilon_{\rm r}$	QSO heating efficiency	0.05
$R_{\rm radio}$	Feedback radius (zones)	8

Table 3.4 lists the parameters and values for the quasar-mode feedback: the two-mode feedback threshold $\chi_{\rm radio}$, the feedback efficiency $\epsilon_{\rm f}$, the QSO heating efficiency $\epsilon_{\rm r}$, and the radius of feedback $R_{\rm radio}$. We fix all these values and do not include any variance in our parameter survey here.

3.3.4 Magnetic field injection

We take the form of injected magnetic fields to be the "tower" model of Li et al. (2006), which assumes an underlying collimated jet extending away from the accretion system:

$$B_r(r',z') = 2B_0 z' r' \exp\left(-r'^2 - z'^2\right) \quad (3.9)$$

$$B_z(r',z') = 2B_0 \left(1 - r'^2\right) \exp\left(-r'^2 - z'^2\right) \quad (3.10)$$

$$B_\phi(r',z') = B_0 \alpha_{\rm B} r' \exp\left(-r'^2 - z'^2\right), \quad (3.11)$$

where $r' = \sqrt{x^2+y^2}/r_0$ and $z' = z/r_0$. Here, we set the scale radius r_0 to be $0.5R_{\rm inj}$, which is $R_{\rm bub}$ for bubbles and $R_{\rm ej}$ for jets, so that the entire injected magnetic structure fits inside the given feedback region. $\alpha_{\rm B}$ is the ratio of poloidal to toroidal flux, which we choose to be $\alpha_{\rm B} = \sqrt{10}$ for a field with minimum initial Lorentz force, as suggested by Li et al. (2006). We determine the scale B_0 by giving some fraction of the available feedback energy to the magnetic field: either 0.0 for purely hydrodynamic outflows, 0.5 for an equipartition case, and 1.0 for purely magnetic outflows. Note that for purely magnetic outflows in jets, we ignore the details of the window function Ψ in Eq. 3.5 and use it simply to determine the extent of the magnetic feedback region. For jet models, we align the axis of the magnetic field with the axis of the jet, and for bubbles we align the magnetic field axis with a vector pointing from the bubble center to the position of the SMBH.

We summarize the parameters of our magnetic field injection in Table 3.5: the radial scale r_0, the ratio of poloidal to toroidal flux $\alpha_{\rm B}$, and the fraction of feedback energy available to magnetic fields $E_{\rm B}$. Aside from the energy of the magnetic injection, we will not vary these parameters.

Table 3.5: Parameters of the magnetic injection model.

Parameter	Description	Values(s)
r_0	Radial scale	$1/2r_{\rm inj}$
$\alpha_{\rm B}$	Poloidal/toroidal ratio	$\sqrt{10}$
$E_{\rm B}$	Fraction of total energy in B	$0.0 - 1.0$

3.3.5 Parameter survey

In Tables 3.6 and 3.7 we detail our parameter survey for jets and bubbles, respectively. We only include in the tables those parameters that we vary in our survey. We have collected each set of parameter changes into several groups. Each group is given a unique numerical identifier, and each set of parameters within that group is given an alphabetical label. For later plots, we label purely hydrodynamic simulations as "h", equipartition models (i.e., $E_{\rm B} = 0.5E_{\rm tot}$) as "e", and purely magnetic feedback runs as "m". Thus, the label "J3Bm" will designate purely magnetic outflow ("m") from the second parameter set ("B") of the third grouping ("3") of the jet models ("J").

For jets, in our first group we study changing the peak grid resolution with a fixed jet size of $h_{\rm ej} = 2.5$ kpc and $r_{\rm ej} = 2.0$ kpc. In the next group we also vary the resolution but allow the jet size to scale with the resolution such that $h_{\rm ej} = 5$ zones and $r_{\rm ej} = 4$ zones. In the third group we vary the accretion strength α. Finally, in the last group we investigate the effects of changing the accretion and depletion radii on the resulting feedback. We do this because the jet model as described in (Cattaneo & Teyssier 2007) does not include any gas depletion, and changing these values can have significant consequences for jets since the feedback is applied very close to the central black hole. Note that for most of the jet groups we do not use our peak resolution of 0.5 kpc, but rather the larger 1.0 kpc. We chose this so that we would have enough numerical resources to complete the study. We only include equipartition magnetic fields in the first group, where we vary the grid resolution. Note that the model set "J1B" serves as our fiducial jet case.

For the first group of our bubble model survey, vary the resolution while keeping the other bubble parameters fixed. Since the bubbles are much larger than the jets (50-200 kpc) we may lower our resolution much more than in the jet runs. In the next two groups we vary the accretion multiple α both with fixed resolution and by scaling α with the grid resolution. For our last group, we fix the bubble position on the SMBH. Note that for this case, we also fix the bubble radius to $R_0 \approx 40$ kpc. This represents an intermediate case between jets and bubbles and is used frequently in cosmological simulations (e.g., Di Matteo et al. 2008; Battaglia et al. 2010). We include the equipartition magnetic feedback mode only with the bubble run ("B1B") which is at the same resolution as the jet runs, and for the fixed bubble run. We do not examine the role that the accretion and depletion radii play in this bubble survey, since the bubble

Table 3.6: Jet model parameter survey.

Designation	Δx (kpc)	α	$h_{\rm ej}$ (kpc)	$r_{\rm ej}$ (kpc)	$R_{\rm acc}/\Delta x$	$R_{\rm dep}/\Delta x$
			Varying Resolution			
J1A	0.50	1	2.0	2.5	2.0	2.0
J1B	1.00	-	-	-	-	-
			Scaling Jet Size with Resolution			
J2A	-	-	4.0	5.0	-	-
J2B	2.00	-	8.0	10.0	-	-
J2C	4.00	-	16.0	20.0	-	-
J2D	-	-	8.0	10.0	-	-
			Varying Alpha			
J3A	0.50	100	2.0	2.5	-	-
J3B	1.00	-	-	-	-	-
J3C	-	300	-	-	-	-
			Varying Accretion and Depletion Radii			
J4A	-	1	-	-	1.0	1.0
J4B	-	-	-	-	4.0	4.0
J4C	-	-	-	-	2.0	0.0

feedback is not as sensitive to these criteria. Note that the model set "B1B" serves as our fiducial bubble case.

3.4 The effects of magnetic injection on AGN feedback

Before we fully examine the growth and structure of magnetic fields using the models described above we must first see what, if any, effects the presence of injected fields have on the accretion and feedback properties of the AGN as well as some of resulting hydrodynamic characteristics of the cluster medium. We choose three of our models to examine: J1B and B1B, representing our fiducial cases for jets and bubbles, respectively, and model B4A, which uses bubbles with fixed centers and radii. For each model we examine purely hydrodynamic injection, fully magnetic injection, and an intermediate equipartition case in which the available injection energy is evenly split between magnetic and hydrodynamic components. For the plots below, models J1B and B1B have plot titles of "Jets" and "Bubbles", respectively, while model B4A is called "Fixed Bubbles."

Figure 3.1 shows the black hole accretion rate as a fraction of the Eddington limit ($\dot{M}/\dot{M}_{\rm Edd}$) for the jet model. We find that simply the presence of an

Table 3.7: Bubble model parameter survey.

Designation	Δx (kpc)	α	$R_{\rm dis}/R_{\rm bub}$
Varying Resolution			
B1A	0.50	1	1.0
B1B	1.00	-	-
B1C	2.00	-	-
B1D	4.00	-	-
B1E	8.00	-	-
Varying Alpha			
B2A	2.00	100	-
B2B	-	300	-
Scaling Alpha with Resolution			
B3A	0.50	50	-
B3B	4.00	300	-
Fixing Bubble Position			
B4A	1.00	1	0.0

injected magnetic field drastically reduces the accretion rate: for ~ 3 Gyr the magnetic fields suppress the accretion rate by a factor of five, with much smaller differences between the equipartition and fully magnetic runs. This has two causes. First, the shape of the magnetic injection, which is initially a torus rather than the axial jet of the hydrodynamic feedback, does somewhat prevent accretion onto the black hole. However, we performed tests where we injected thermal energy with the same distribution as the magnetic injection and found only small differences. The main cause of the reduced accretion rate is the "unspringing" of the highly tense injected fields. As the fields unfold after injection they efficiently drive gas away from the central zones. Eventually, however, the gas is able to cool sufficiently and overcome this tension and the accretion rate correspondingly jumps. However, the magnetized outflows still maintain an accretion rate a factor of two lower than in the purely hydrodynamic case. The accretion rate for the magnetized cases are also high variable with a rapid period of 1-10 Myr. This is indicative of the complex relationship between the unfolding magnetic fields and the gas which is attempting to accrete onto the black hole.

After 6 Gyr, the purely hydrodynamic mode undergoes a period of intense activity characterized by a rapid rise in accretion rate as the gas cools sufficiently and an associated enhanced feedback phase (see Cattaneo & Teyssier 2007). At this point the strong magnetic fields in the core become highly tangled, and the combination of strong fields surrounding the core and cold, dense gas at the core severely lowers our magnetohydrodynamical timestep. Thus we can not

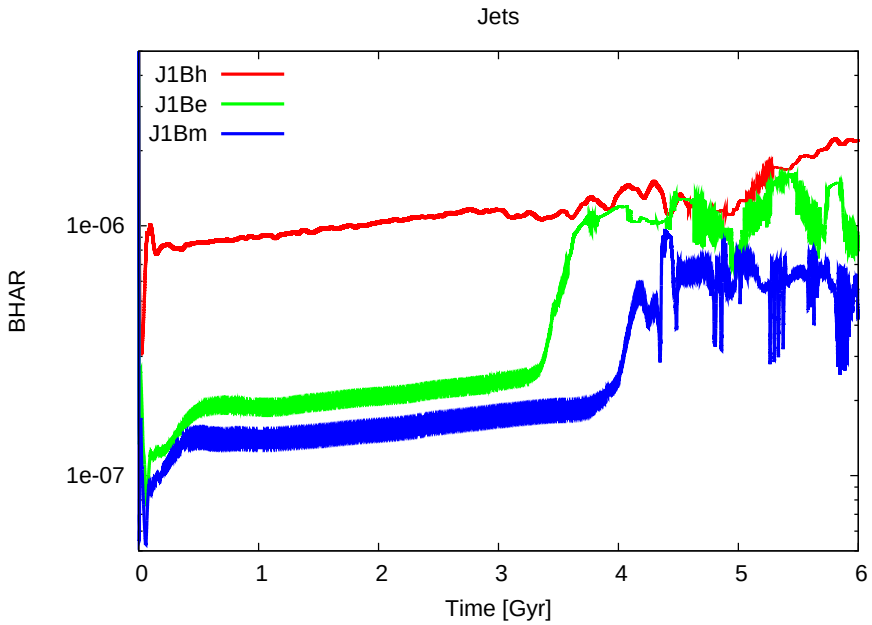

Figure 3.1: Effects of magnetic injection on the black hole accretion rate. Shown is BHAR ($\dot{M}/\dot{M}_{\rm Edd}$) versus time for purely hydrodynamic, equipartition, and fully magnetic modes of the J1B (Jets) model

efficiently carry the simulation further and simultaneously perform our intended parameter survey. For this run and all others, we evolve the simulations until the timestep drops too low to continue effectively. However, we are still able to perform these simulations across billions of years, and the timing of the onset of complex fields can yield useful information about the relationship between the magnetic fields and the cluster gas.

The effects of the injected magnetic field are much less pronounced in the randomly-placed bubble model (B1B), as shown in Figure 3.2. Since the bubbles are large and off-centered, the magnetic fields are not as effective as driving away gas from the core, and hence the accretion history is nearly identical between the purely hydrodynamic and both magnetic modes. Additionally, there is almost no difference between the equipartition and fully magnetic modes. This is highlighted by the changes to the bubbles size, as shown in Figure 3.3 (note that the other bubble model examined here, B4A, uses a fixed bubble radius, and thus is not shown). The bubbles in all cases start out very large, with radii nearly 200 kpc. Over 4 Gyr they grow smaller and more frequent as the core density increases. Eventually the hydrodynamic bubbles begin to exhibit periodic behavior, but the magnetic fields become too complex to follow efficiently at this resolution.

When we force the bubbles to be centered on the black hole, as with model B4A, we achieve similar suppression of the accretion rate as in the jets, as we see in Figure 3.2. These differences take $\sim$ 3 Gyr to manifest, however, since

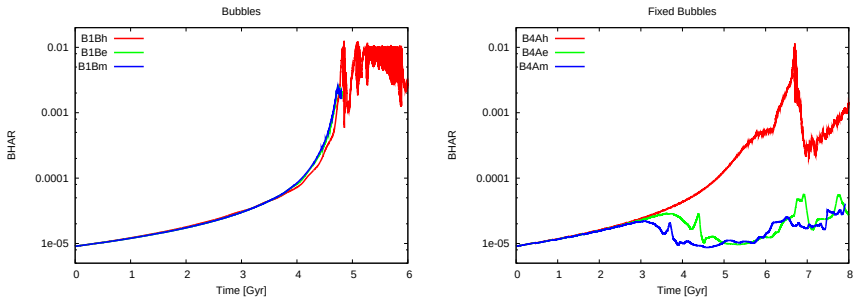

Figure 3.2: Effects of magnetic injection on the black hole accretion rate. Shown is BHAR ($\dot{M}/\dot{M}_{\rm Edd}$) versus time for purely hydrodynamic, equipartition, and fully magnetic modes of models B1B (Bubbles), and B4A (Fixed Bubbles).

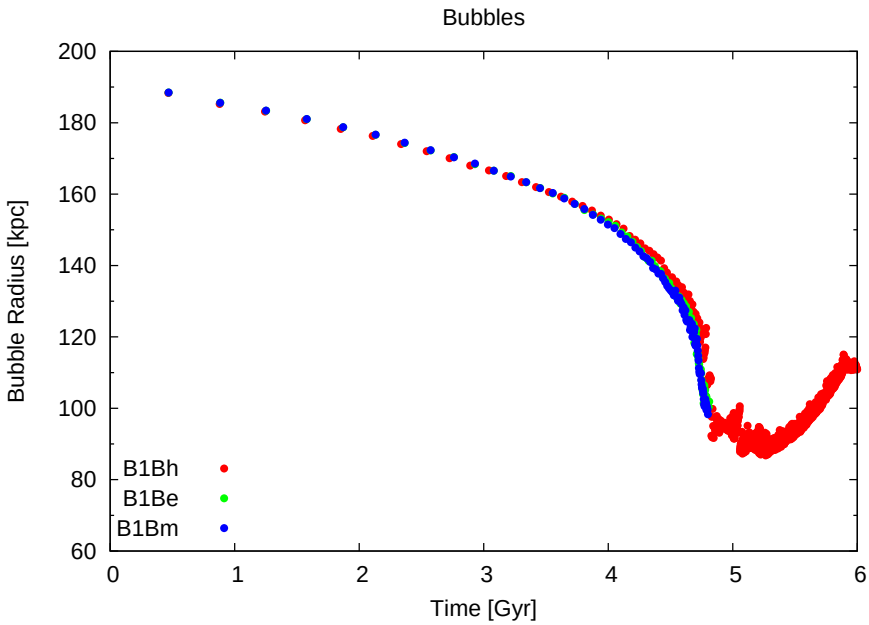

Figure 3.3: Effects of magnetic injection on the bubble size. Shown is bubble radius at each injection event as a function of time for model B1B.

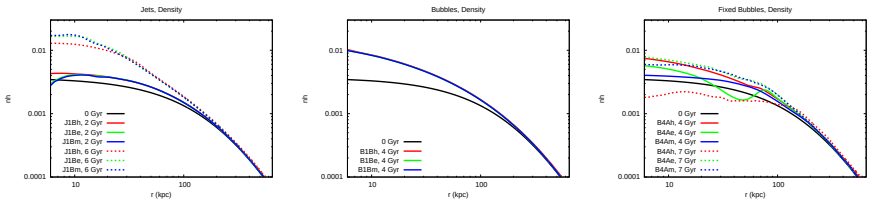

Figure 3.4: Effects of magnetic injection on the cluster density profile.

the bubbles are larger than the injection region and hence not as efficient as the jets at driving away gas (this is also noticeable when comparing the purely hydrodynamic modes, where the jets have an accretion rate roughly an order of magnitude smaller than the bubbles). Once again we also see the importance of merely the presence of magnetic injection over the relative strength of those fields: both the equipartition and fully magnetic modes exhibit nearly the same behavior, which after 3 Gyr is characterized by small (factor of ~ 2) changes to the accretion rate with a cyclic period of roughly 3 Gyr, whereas the hydrodynamic injections see much larger variations in the accretion rate over much smaller timescales.

We build radial profiles of the density in Figure 3.4. These are constructed from volume-averaged quantities in shells of thickness 1 kpc. For the jets we see that at 2 Gyr the magnetized injections are more effective at driving gas away from the core, but outside of the central regions of the cluster there are very few differences. However, after 6 Gyr the accreting gas pushes through the magnetic fields and the magnetized outflows end up with a slightly higher central density, though once again the injection modes are indistinguishable past 20 kpc. Even though the density is higher in the magnetized runs, the sound speed is also higher, resulting in the reduced accretion rate discussed above.

The randomly-placed bubbles, as expected, exhibit also no differences between magnetized and unmagnetized profiles at 4 Gyr, whereas the fixed bubbles show remarkable differences out to a radius of 100 kpc. At 4 Gyr the magnetized outflows have prevented large amounts of material from collapsing into the core and the equipartition mode has formed a low-density shell from 30 to 70 kpc. The purely hydrodynamic model has a much smaller low-density shell at 70 kpc. For the hydrodynamic case the heated outwardly-expending gas in the injection regions prevents further accretion of material from the rest of the cluster while some of the inner material within the injection region falls towards the black hole. In the equipartition case the complex interplay of the magnetic fields and injected thermal energy form a larger shell. For the fully magnetized outflow the magnetic fields simply drive gas away from the core. By 7 Gyr, however, the profiles have reversed: the intense activity of the hydrodynamic bubbles have driven gas away from the core (note that this profile is taken from a point in time which is at the trough in a cyclic pattern, as seen in Figure 3.2) while the more sedate magnetized injections see relatively little change in the

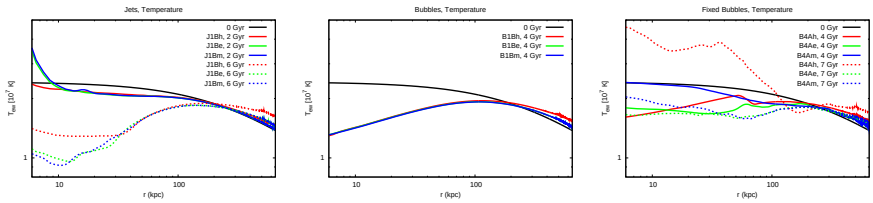

Figure 3.5: Effects of magnetic injection on the cluster temperature profile. Shown is emission-weighted temperature.

density profiles.

These conditions are also reflected by the emission-weighted temperature, as we show in Figure 3.5. Note that we did not observe significant differences in the pressure profile and hence do not show them here. For the jets, the magnetic fields, which are much more effective at removing gas from the central core, heat up the gas to 3.5×10^7 keV after 2 Gyr of evolution. Eventually the gas is able to cool, and in the magnetized case the gas reaches 10^7 keV after 6 Gyr, about 30% lower than in the purely hydrodynamic case. This is also the case with the fixed bubbles, where initially the magnetized outflows maintain higher temperatures in the core relative to the thermal outflows, but after 7 Gyr the magnetic bubbles change the inner temperature by at most 20%, whereas the hydrodynamic bubbles heat the gas considerably.

3.5 The growth of magnetic fields

To examine in detail the growth of magnetic fields, we will take only our fiducial cases J1B for the jets and B1B for the bubbles as well as the intermediate fixed bubble case of B4A. These three cases have the same peak resolution and accretion properties and - other than the form of the injection - these runs differ only in that the bubble runs use a larger centrally-refined region. For this section we only study fully magnetic injection, with no portion of the feedback energy in thermal or kinetic modes.

We first examine the rate of magnetic field injection, $B_{\rm inj}$, in Figure 3.6. The jets (model J1B) inject magnetic fields continuously at a rate ~ 600 μG Myr^{-1} for approximately 4 Gyr. Once the core begins to significantly cool down the accretion rate jumps and subsequently the jets become more powerful, seeding magnetic fields at an average rate of 1100 μG Myr^{-1}. Periodic behavior also sets in with spikes of up to 8000 μG Myr^{-1} occurring every ~ 500 Myr. Since the feedback in this case takes place in the volume which is used to measure the accretion rate, the injected magnetic field rate is highly sensitive to small perturbations in the gas properties of this region, and thus very noisy. Also, the total feedback magnetic energy is distributed over a much smaller volume than the bubbles, hence the higher magnetic field values.

Both bubble models require ~ 400 Myr before the first injection event takes

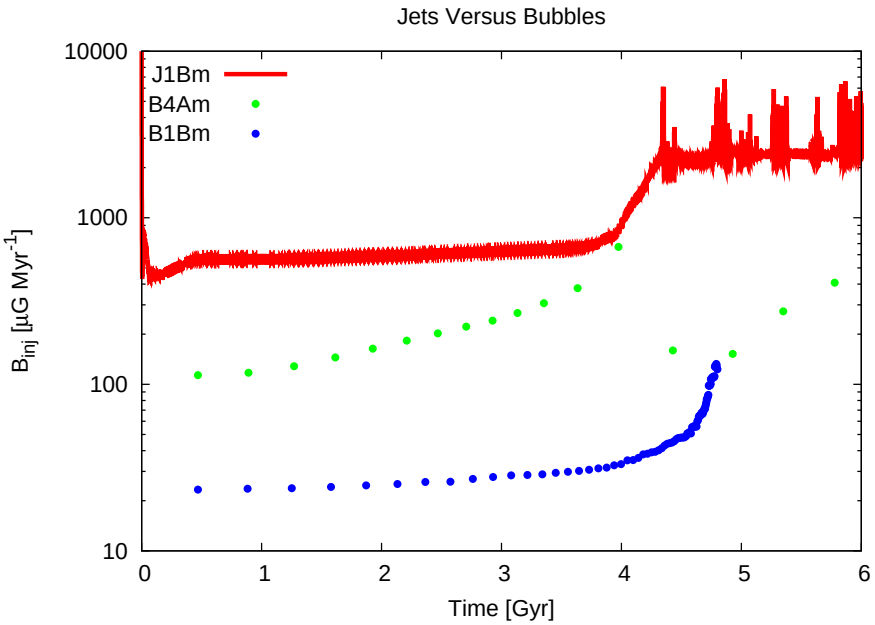

Figure 3.6: Rate of injected magnetic field strength. Shown is $B_{\rm inj}$ versus time for models J1B, B4A, and B1B. The continuous injection rate for J1B is shown as a line while the points represent the discrete injection events for models B4A and B1B.

place. While the fixed bubbles (model B4A) inject fields about 5 times stronger than the randomly-placed bubbles (model B1B), these injections take place within a fixed radius of 40 kpc, while the randomly-places bubbles have radii of ~ 200 kpc initially. Thus while the injected energies are identical for the initial injection and roughly equal for the subsequent 4 Gyr, the randomly-placed bubbles distribute this energy over a large volume and hence the magnetic field strength within that volume is lower. The fixed bubbles reach a peak injection rate of 700 μG Myr^{-1} before strong outflows prevent further accretion at 4 Gyr, which is roughly the same time when the jets begin their strong feedback phase. The randomly-placed bubbles, which take longer to drive gas away from the core, only reach a peak injection rate of 100 μG Myr^{-1} before the complex field topology prevents further efficient calculations.

We show in Figure 3.7 the average magnetic field strength within two radii, $R = R_{\rm core} \equiv 0.15R_{500}$ and $R = R_{200}$. We take a density-weighted average in the core and a volume-weighted average for the entire cluster. The fixed bubbles are most efficient at strongly magnetizing the core, reaching 1 μG after just 1 Gyr, which is an oder of magnitude stronger than the jets and randomly-placed bubbles, and a peak value of over 2 μG averaged inside the core after 4 Gyr. After that time the reduced accretion rate prevents further strengthening of the field in the core. At that time strong outflows prevent further strong feedback events and the magnetic fields in the core push outwards into the

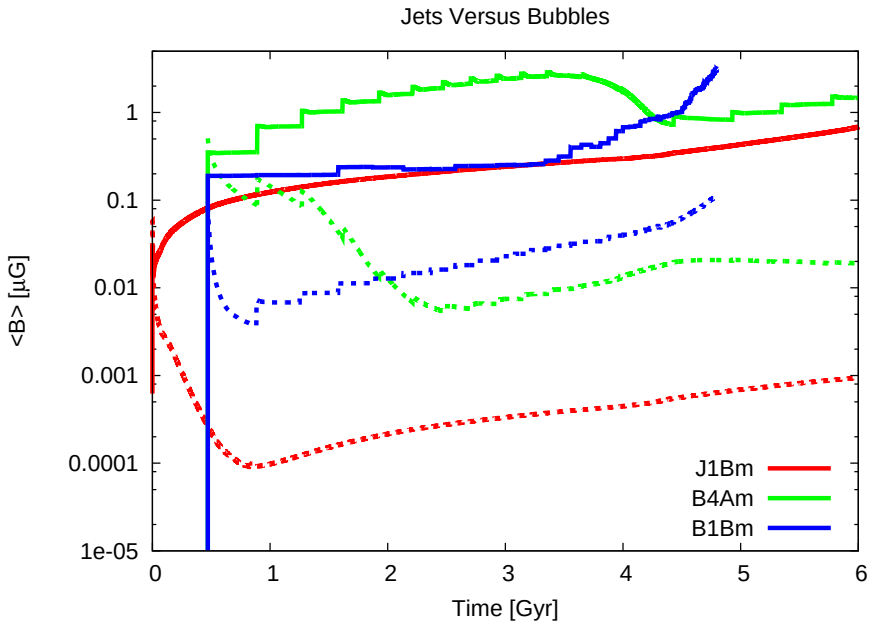

Figure 3.7: Average magnetic field strength with jets and bubbles. Solid lines are density-weighted average fields within $R_{\rm core}$ and dotted lines are volume-weighted fields within R_{200}.

cluster medium without being replenished. The jets, however, continuously operate and are always able to magnetize the core. Thus while initially the jets provide the weakest magnetic fields in the core they eventually build up enough strength to provide roughly the same magnetization as the fixed bubbles after 6 Gyr. Randomly-placed bubbles are the least efficient at magnetizing the core, since the bubbles are large and off-center. However, they do begin to produce strong fields after 4 Gyr.

Jets and fixed bubbles exhibit similar patterns when averaging fields over the entire cluster. Here the initially-injected fields quickly disperse throughout the cluster medium but eventually weaken by escaping beyond R_{200} and through numerical dispersion. However, fields from the core eventually make their way to the outer regions of the cluster and after 1-2 Gyr the average fields begin to rise again. The bubbles maintain cluster-wide fields over an order of magnitude stronger than the jets, mainly because the bubbles inject their fields farther out from the core, allowing them to more easily propagate into the cluster. The large bubbles of the randomly-placed bubble model eventually provide magnetic fields throughout the cluster as strong as the fixed bubbles.

Next we can study the growth rate of magnetic fields within the cluster volume in Figure 3.8. Here we show the total volume encompassed by fields of strength at least 10^{-12} G and 10^{-6} G. While all models are able to weakly magnetize the entire cluster, they differ substantially in the time taken to do so. The jets (model J1B) continuously inject strong fields in the core which

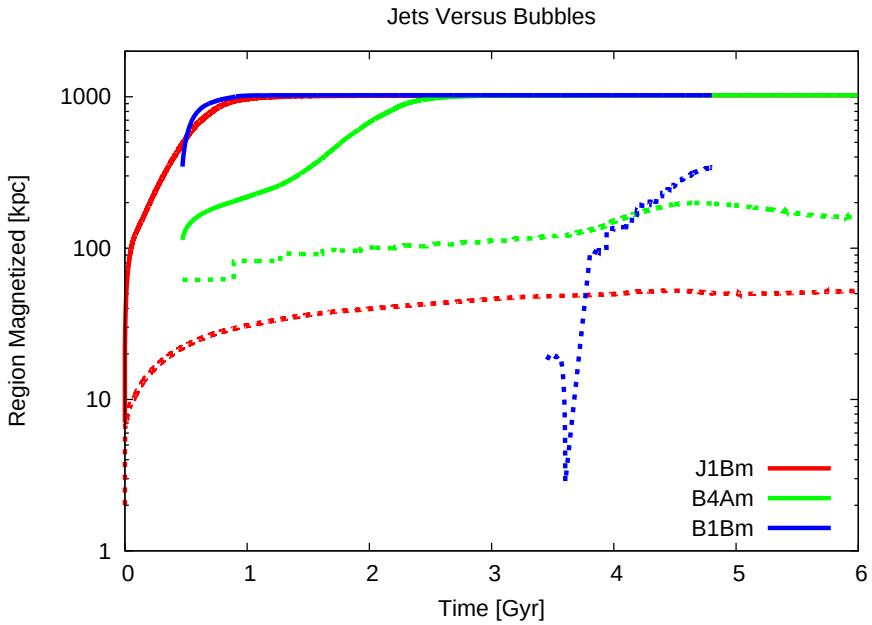

Figure 3.8: Volume magnetized due to jets and bubbles. Shown is the cube root of the total volume containing fields of strength at least 10^{-12} G (solid lines) and 10^{-6} G (dotted lines).

push out weaker fields into the cluster, saturating the cluster within 1 Gyr. The randomly-placed bubbles (model B1B) saturate the cluster almost immediately since the bubbles are very large and centered away from the core. The fixed bubbles (model B4A) take the longest, 2 Gyr, since these injected fields are centered at the core but are much weaker than the fields injected by the jets and hence less efficient at pushing weaker fields throughout the cluster.

Strong fields permeate a much smaller volume, with jets only able to provide $\sim$ μG fields within the inner 50 kpc. The fixed bubbles, with radii of 40 kpc, are naturally able to strongly magnetize almost the entire core out to a radius of 100 kpc and maintain this magnetization for five billion years. The randomly-placed bubbles cannot produce significant magnetic fields until multiple bubbles overlap so that their magnetic contributions can add together, which does not occur until 3.5 Gyr of evolution. These fields quickly disperse but recover when the bubble feedback becomes strong enough to continuously produce strong fields.

Figure 3.9 shows the total kinetic and magnetic energies within the entire cluster volume as a function of time. The evolution of the magnetic energy follows the same evolution as the injection rate. The kinetic energy follows a strongly periodic behavior as gas cools and accretes onto the black hole and is driven outwards by outflows. The kinetic energy for all cases also follows the magnetic energy, since magnetic tension in the injected fields drive additional gas motions. Since the fields of the jet model are centrally located they are less

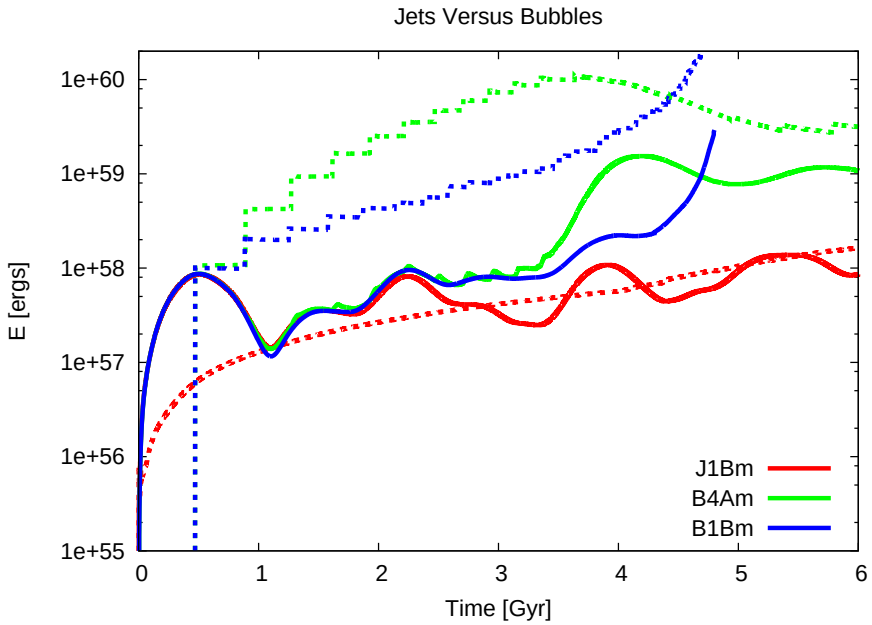

Figure 3.9: Total cluster kinetic and magnetic energy versus time. Solid lines are kinetic and dotted lines are magnetic energy.

likely to drive large-scale complicated gas motions, whereas the bubbles with large, diffuse, tangled magnetic fields generate complicated gas motions. The turbulence due to these bubbles produce kinetic energies an order of magnitude larger than the jets.

Finally we show radial profiles of the magnetic field in Figure 3.10 at 3 and 6 Gyr. We construct these profiles from volume-weighted averaging of the field in 1 kpc shells. At 3 Gyr, the fixed bubbles maintain the strongest fields (10 times stronger than the jets and 30 times stronger than the randomly-placed bubbles) within the central 100 kpc but at large radii these fields diminish rapidly. Both bubble models have the same profile shape: an inner plateau where the fields are injected and a steep reduction in field strength beyond that radius. The randomly-placed bubbles, which place weaker magnetic fields within a larger region, maintains this plateau to almost 300 kpc, which is sensible because the bubbles involved have typical radii of 150 kpc. The jets produce some slope within the inner 50 kpc and the strongest fields in the innermost core, as expected. All the models produce only weak fields ($< 10^{-12}$ G) beyond a radius of 600 kpc.

At 6 Gyr, both the jets and fixed bubbles (the randomly-placed bubbles only evolved to 4 Gyr) exhibit opposite trends. The jets continuously amplify the fields in the core, boosting the field strength in the inner 50 kpc by a factor of four while continuing the strengthening the magnetic fields at larger radii. The fixed bubbles, however, experience a drop in accretion rate at ~ 4 Gyr and hence their ability to magnetize the core after that diminishes. Thus the fields

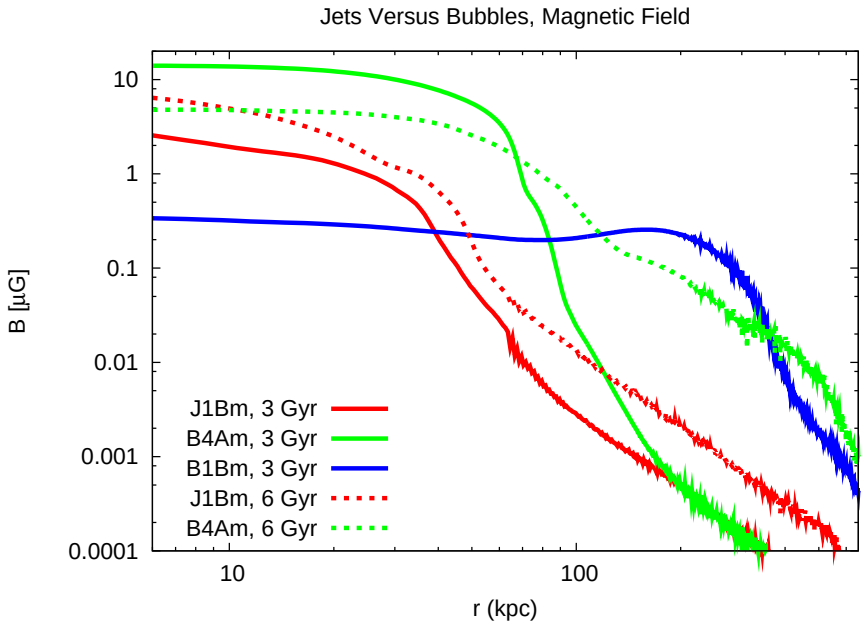

Figure 3.10: Volume-weighted magnetic field as a function of radius.

from the inner regions of the cluster just propagate outwards, magnetizing the remainder of the cluster while reducing the magnetization of the core. After 6 Gyr the jets eventually produce the strongest magnetic fields in the core, but the fixed bubbles generate a more highly-magnetized cluster overall.

3.6 Magnetic field topology

We now turn to the topology of the fields produced by our fiducial jet and bubble models: J1B to represent the jets, B1B for randomly-placed bubbles, and B4A for fixed bubbles. Streamlines of the fields demonstrate the complex morphology produced by the AGN-based injection. We generate streamlines by seeding 100 tracer particles uniformly on a sphere of radius 300 kpc. Figure 3.11 shows the streamlines for the fiducial models at various times. Each model is shown at 1 and 3 Gyr and at a time just before complex fields prevent further calculation. Thus we show the streamlines at 6 Gyr for the jets, 4 Gyr for the randomly-placed bubbles, and 8 Gyr for the fixed bubbles.

The jets initially produce a toroidal shape with a very regular structure: as the fields are injected as a torus they push out already-present fields which maintain their structure. After 3 Gyr the fields elongate along the jet axis forming a tower with cavities opening in the plane perpendicular to the jet. The magnetic field is able to escape quickly along the jet axis, quickly magnetizing volumes outside the core. Finally, at 6 Gyr, the gas is able to cool sufficiently, dragging the field lines along with it as it accretes onto the core. We thus form a dense cocoon of magnetic field lines. These fields are only slightly tangled and

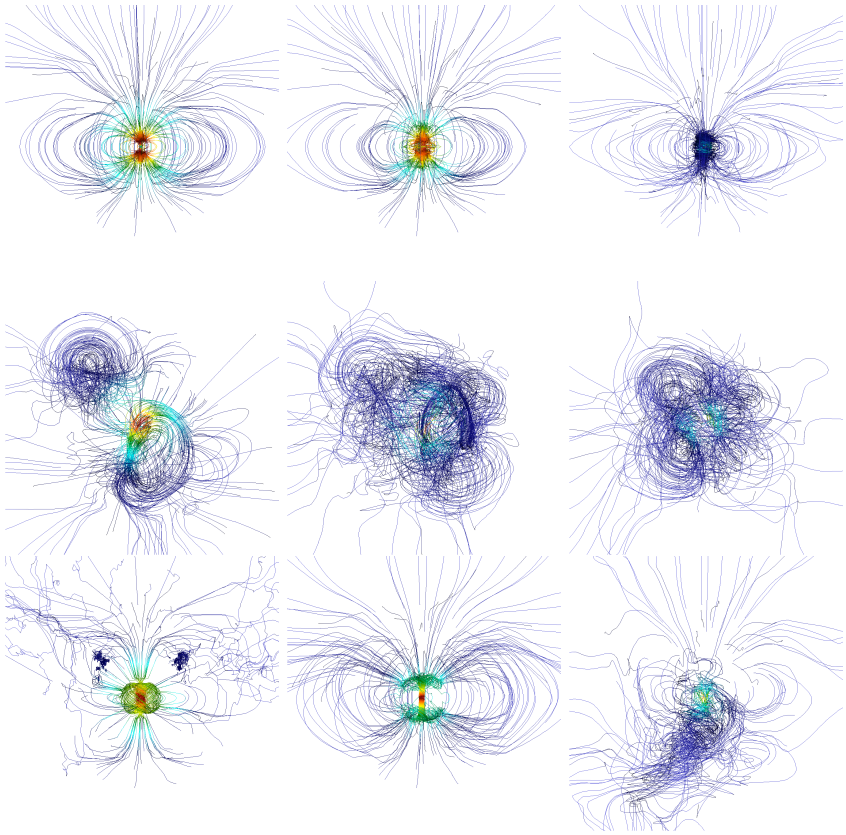

Figure 3.11: Evolution of magnetic field streamlines for the fiducial models. Shown are models J1Bm (top), B1Bm (middle), and B4Am (bottom). From left to right, model J1Bm is shown at times 1, 3, and 6 Gyr, model B1Bm is shown at times 1, 3, and 4 Gyr, and model B4Am is shown at times 1, 3, and 8 Gyr. All streamlines are constructed using 100 tracer particles uniformly distributed on a sphere with radius 300 kpc. The streamlines are colored by the local gas density, with blue colors indicating low density and red colors denoting high-density regions. The view is roughly 600 kpc across.

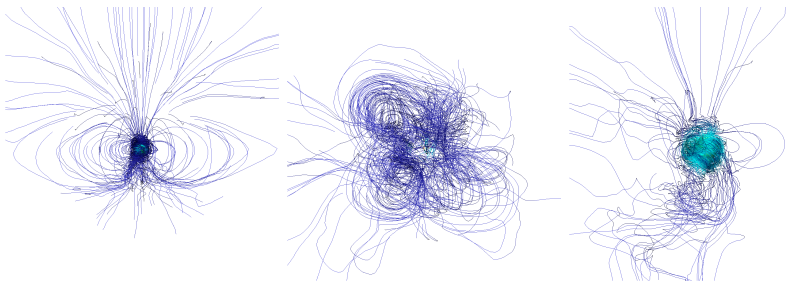

Figure 3.12: Magnetic field streamlines from the equipartition injection mode. Shown are models J1Be at 6 Gyr (top), B1Be at 4 Gyr (middle), and B4Ae at 8 Gyr (bottom). Construction of the streamlines and coloring is identical to Figure 3.11.

maintain their regular torus-like structure, but stronger fields have been able to propagate farther into the cluster.

The randomly-placed bubbles exhibit complex, tangled behavior almost immediately. While each bubble contains a torus-like magnetic field, as multiple bubbles form and overlap the fields entangle. The bubbles are able to form strong fields with complex structures far from the central core. At later times more bubbles form and overlap, increasing the average magnetic field in the core. Few magnetic field lines are able to escape into the outer cluster regions, even after 4 Gyr. However, the volume magnetized by bubbles is much larger than that of the jets. The bubbles are also much more asymmetric than the fields produced by the jets, since each injected bubble has a new, random field orientation.

The fixed bubbles initially exhibit only somewhat ordered topology. While each bubble has the same magnetic field orientation, between bubble events some magnetic field lines can escape and turbulence caused by the infalling gas can twist and tangle the fields. At 3 Gyr, however, the bubbles appear frequently enough to maintain a torus-like topology. Eventually the fields collapse due to the asymmetric infill of the gas and a large parcel of magnetic field lines escape along the jet axis leading to a complex topology containing both ordered torus-like and tangled components.

We also show the equipartition case for each fiducial model in Figure 3.12 at the latest time available for each model. For each model the magnetic fields are weaker but the larger topology remains unaffected. The final cocoon created by the jets is smaller since the injected fields are not as strong. The weaker fields of both the randomly-placed and fixed bubbles produce much more disperse field lines. Thus while we affect the overall strength of magnetic fields we do not change the topological structure of the fields when considering injection modes with less magnetic energy. Also, the addition of thermal energy in the equipartition case does not affect the topology of the fields.

Next in Figure 3.13 we see the evolution of the magnetic field in terms of the rotation measure (RM) taken along the x-axis. The rotation measure is defined

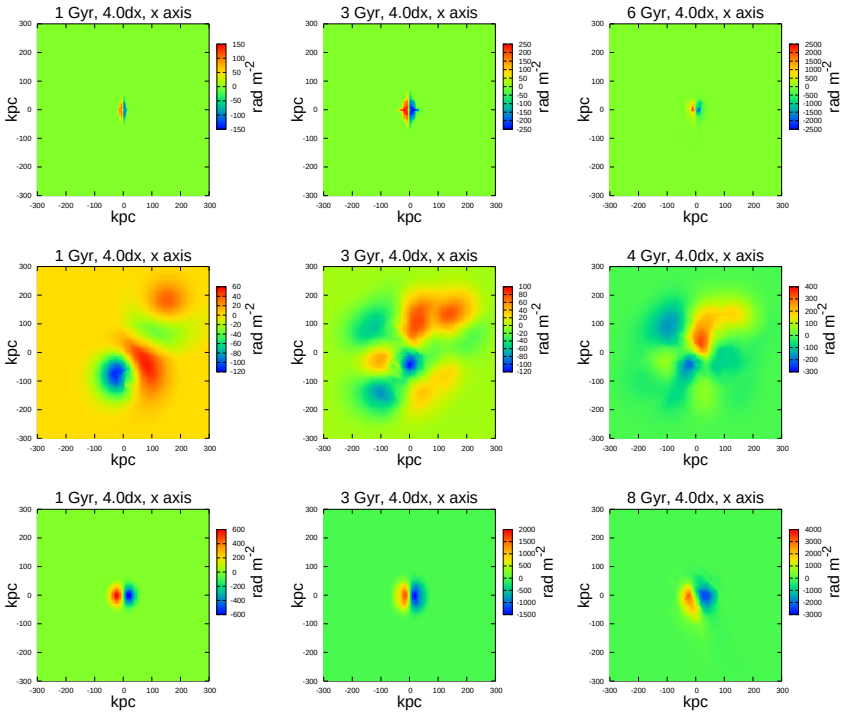

Figure 3.13: Evolution of the rotation measure for the fiducial models. Shown are models J1Bm (top), B1Bm (middle), and B4Am (bottom). From left to right, model J1Bm is shown at times 1, 3, and 6 Gyr, model B1Bm is shown at times 1, 3, and 4 Gyr, and model B4Am is shown at times 1, 3, and 8 Gyr. All rotation measures are taken along the x-axis and have a uniform resolution of 4 kpc.

as

$$\mathrm{RM} = 812 \int_0^L n_e \mathbf{B} \cdot d\mathbf{l} \text{ radians m}^{-1}, \tag{3.12}$$

where $\mathbf{B}$ is the magnetic field in μG, n_e is the electron density, and $\mathbf{l}$ is the direction of propagation in kpc. The maps shown have a spatial resolution of 4 kpc.

The jets at 1 Gyr show high rotation measure values with very little spatial extent: only ~ 10 kpc perpendicular to the jet and ~ 50 kpc along the jet axis. The RM exhibits the handedness given to the injected magnetic fields, with a value of 150 to the left of the jet and -150 to the right. At 4 Gyr the strong RM region in the center is slightly larger with peak values about three times stronger. By 6 Gyr the strong feedback episodes have dramatically increased the peak RM value to over 2500 and the collapsing gas has shrunk the volume enclosed by strong magnetic fields. Also, turbulent gas motions have begun to introduce some asymmetry in the RM map; however, the overall structure remains intact. TODO

The magnetic fields produced by the randomly-placed bubbles result in large-scale ($\sim$ 400 kpc) weak RM structures within 1 Gyr. However, the RM here

is much weaker - reaching a value of no more than 400 by 4 Gyr - than those generated by the jets since the magnetic fields are distributed over a much larger volume. As more bubbles form, the peak RM values increase and distribute over a large volume, eventually forming $\sim$ 100 kpc structures surrounding the central core. The fixed bubbles show a similar handedness as the jets since once again each injection is given the same axis. However, the RM here reaches a peak value much stronger than both the randomly-placed bubbles and the jets. Additionally, strong RM values are distributed over a much larger volume, reaching $\sim$ 100 kpc into the cluster atmosphere.

We additionally view the latest times available for each model in the y and z directions in Figure 3.14. The highly-directional jets show identical RM distributions in both the x- and y-directions, but the rotation measure along the jet axis shows little spatial variation and a very high value within the central 10 kpc. The randomly-placed bubbles exhibit nearly identical morphology along the other axes, as expected by the random orientations given to each injected bubble. The fixed bubbles exhibit similar morphology as the jets, with large RM values along the z-axis, but with some discernible rotation measure extending out to $\sim$ 100 kpc, much farther than the smaller jets.

Finally, we can compare equipartition modes to fully magnetized injection with Figure 3.15. Once again we see little difference in the overall structure for the jets and both bubble models. The values of the peak rotation measures are only slightly less in the equipartition cases than they are in their fully magnetic counterparts. Additionally, the randomly-placed bubbles show a much more smooth and uniform distribution with equipartition injection. The jets and fixed bubbles maintain their spatial extent. Thus we once again see that merely the presence of magnetic injection has significant effects and the relative proportion of magnetic to thermal energy is less important.

3.7 Model parameter survey

3.7.1 Jets

Our jet model parameter survey includes variations in the underlying peak grid resolution, the size of the jet, the value of the accretion strength parameter α, and the size of the accretion and depletion regions. For the plots in this section, we will label the model groups as follows: models J1A-J1C are labeled as "Jet Resolution", models J2A-J2C are the "Jet Size" group, "Jet Accretion Strength" will refer to models J3A-J3C, and finally models J4A-J4C will be referenced by "Jet Depletion and Accretion".

These parameter changes significantly affect the accretion history of the SMBH, as shown in Figure 3.16. With higher resolution (model J1A) the accretion history is much more variable but the average accretion rate is roughly equal to the fiducial case. In this case the strong injected fields make continuation of

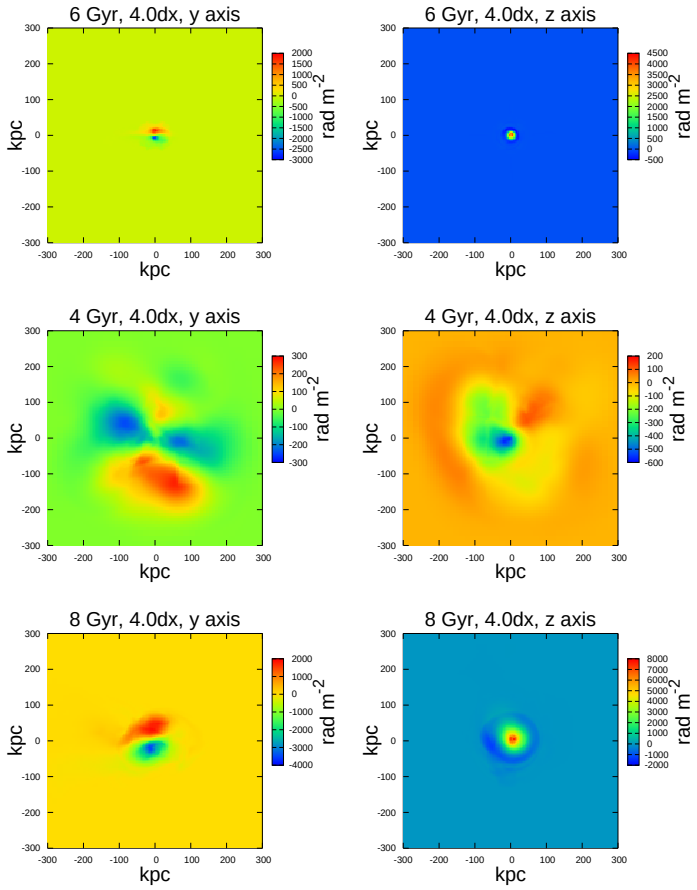

Figure 3.14: Rotation measure taken along the y-axis (left) and z-axis (right). Shown are models J1Bm at 6 Gyr (top), B1Bm at 4 Gyr (middle), and B4Am at 8 Gyr (bottom). All rotation measures have a uniform resolution of 4 kpc.

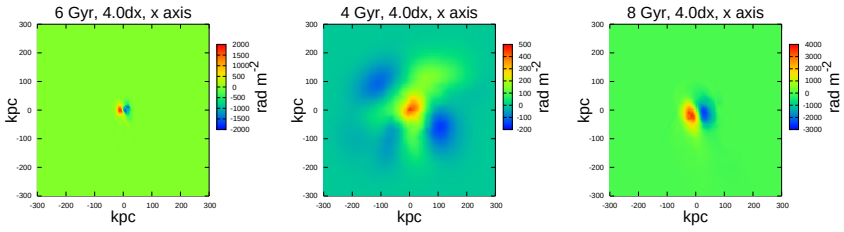

Figure 3.15: Rotation measure from the equipartition injection mode. Shown are models J1Be at 6 Gyr (top), B1Be at 4 Gyr (middle), and B4Ae at 8 Gyr (bottom). All rotation measures are taken along the x-axis and have a uniform resolution of 4 kpc.

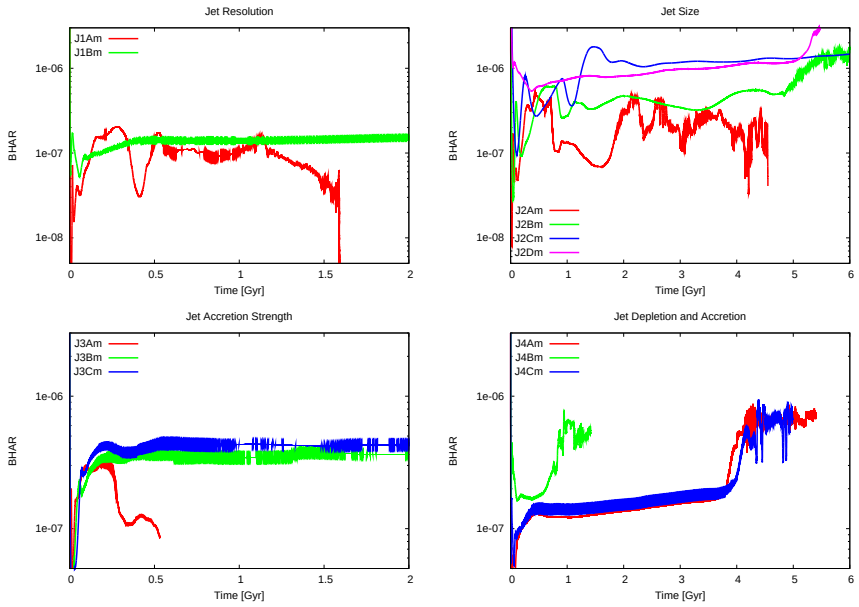

Figure 3.16: Affecting the black hole accretion rate by varying the jet model parameters. Shown is BHAR ($\dot{M}/\dot{M}_{\rm Edd}$) versus time.

the simulation very difficult past 1.5 Gyr and at this point the combination of turbulent gas motions and strong fields make the accretion rate highly variable. When we vary the jet size we get more diverse behavior and longer-lasting jets. In model J2A, where we double the size of the jets, we maintain the same average accretion strength as in the fiducial case but add the periodic behavior seen with the well-resolved jets of model J1A. As we increase the jet size while fixing $\Delta x = 1.0$ kpc in models J2B and J2C we see a consistent increase in the average accretion rate. As the jet energy gets deposited in a larger volume the magnetic fields are less effective at keeping gas away from the central black hole. When we decrease the relative size of the jet in model J2D, the smaller jet is more effective at removing gas, thereby lowering the accretion rate relative to the J2C model, which has the same resolution but a larger jet.

When we vary the accretion strength parameter α (models J3A-C), we see similar evolution patterns in the accretion rate, but the rates are uniformly higher than the fiducial case. Model J3A, which both lowers the resolution to $\Delta x = 0.5$ kpc and raises α to 100, produces incredibly strong fields within 0.5 Gyr, preventing further simulation. However, prior to this point there still appears to be some periodicity with similar features to model J1A, which has the same resolution but $\alpha = 1$. Interestingly, setting $\alpha = 100$ does not produce an accretion rate that is 100 times higher. Instead, the stronger outflows are more effective at pushing away gas from the core, lowering the overall accretion rate to just a factor of five larger than the fiducial case. Similarly, with $\alpha = 300$ in model J3C we do not see a corresponding tripling of the accretion rate.

Varying the depletion and accretion radii can have some significant effects,

especially if these values are larger than the injection region. Model J4A sets $R_{\rm dep} = R_{\rm acc} = \Delta x$ (i.e., one zone), and we do not see significant differences between this and the fiducial case. This is also the case when we remove depletion altogether, as in model J4C. Since the accretion rate is incredibly small for the jets in the first place, removing gas has no significant effects. However, when we set the accretion and depletion radii to 4 zones, as in model J4B, we see an initially larger accretion rate followed by a factor of five jump after only 1 Gyr, rather than the 4 Gyr it takes in the fiducial model. In this case, we are measuring within a volume slightly larger than the injection region itself (note that the injected magnetic fields are strongest at the scaling radius, which is one half the injection radius) and the gas that the magnetic fields drive away from the core gets included in the accretion rate calculation, leading to an increase in the accretion rate. Also the large jump in accretion rate occurs earlier since we are measuring at a larger radii, and the cooled gas does not take as long to reach the inner 4 kpc as it does to reach the inner 2 kpc, where the magnetic injection is strongest.

In Figure 3.17 we see how varying the jet parameters affects the rate of injected magnetic field strength. For model J1A, despite the small changes to the accretion rate, the injected magnetic field rate is almost a factor of two higher. This is mainly due to a severely decreased timestep in the J1A run: although the instantaneous accretion rate, and hence the injected magnetic energy, may be lower, the total injected magnetic field over long periods of time are larger in the higher-resolution run. When we vary the jet size, we find that model J2A, despite having the lowest accretion rate, has the highest rate of injection of magnetic fields. This is because this model injects magnetic fields into the smallest region. The resulting field is more strongly concentrated, leading to a higher B. As we scale to ever-larger jets, the fields are distributed over larger volumes, and hence the $B_{\rm inj}$ rate drops. Model J2D, which has a lower resolution but same jet size as J2B, maintains roughly the same injection rate, consistent with the view that these low resolutions to not contribute significantly to the resulting magnetic fields.

Varying the accretion strength parameter α has almost no effect: since the accretion rate self-regulates with changes in α, models J3B and J3C are not significantly different. However, model J3C, with a larger α of 300, does produce slightly stronger magnetic fields. When we vary the accretion and depletion radii, we once again see only strong differences with model J4B, which produced fields almost an order of magnitude stronger than the fiducial case after only 1 Gyr.

Figure 3.18 shows the changes to the average magnetic field strength within $R_{\rm core}$ and R_{200}. The higher-resolution jets (J1A) and large jets (J2C) are best at magnetizing both the inner and outer cluster regions. As expected, the large jets are able to distribute fields over a much larger volume than the fiducial case, although they cannot produce fields stronger than ~ 1 μG in the core. There

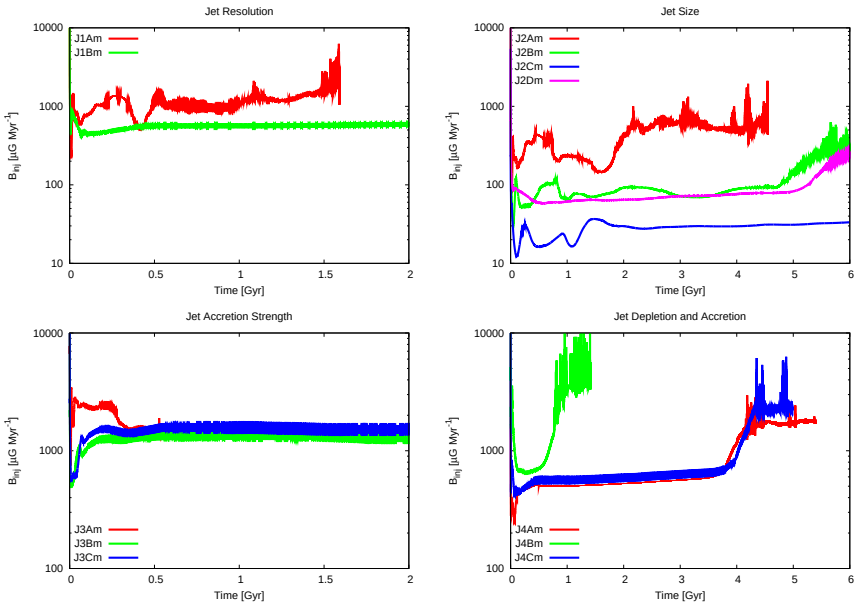

Figure 3.17: Affecting the rate of injected magnetic field strength by varying the jet model parameters.

is again no significant difference when increasing α from 100 to 300, although these models produce slightly stronger fields within the core compared to the fiducial case. Despite the enhanced accretion rate of model J4B, we do not evolve the jet long enough to see significant differences in the average field of the core. However, we do begin to see an increase in the overall magnetization of the cluster, with roughly a doubling of the average cluster-wide field.

We see similar trends in the magnetized volume, as shown in Figure 3.19. The large jets and high-α jets push weak magnetic fields throughout the cluster volumes in less than 500 Myr, whereas the fiducial case takes almost twice as long. However, the high-α models still do not push strong fields very far into the cluster - only to $\sim$ 50 kpc. On the other hand, the large jets can generate strong fields out to 100 kpc. Also, here the effects of higher resolution are less pronounced. With the boosted accretion rate of model J4B, the cluster saturates with weak magnetic fields much more quickly (less than half the time of the fiducial case), with a slightly increase in the volume of strong magnetic fields. Once again, we do not see large differences with the smaller accretion and depletion radii relative to the fiducial model.

Finally, we see in Figure 3.20 the radial profiles of the magnetic fields. We first see that model J1A, which has higher resolution than the fiducial case, is able to provide more magnetization throughout the cluster in 1 Gyr than the fiducial case is able to in twice that time. All of the large jets are able to generate strong fields in the core (over 10 μG in some case) after 6 Gyr. However, since the magnetic fields of model J2C are distributed over such a large volume, the strongest fields in the core come from the slightly smaller jets of model J2B.

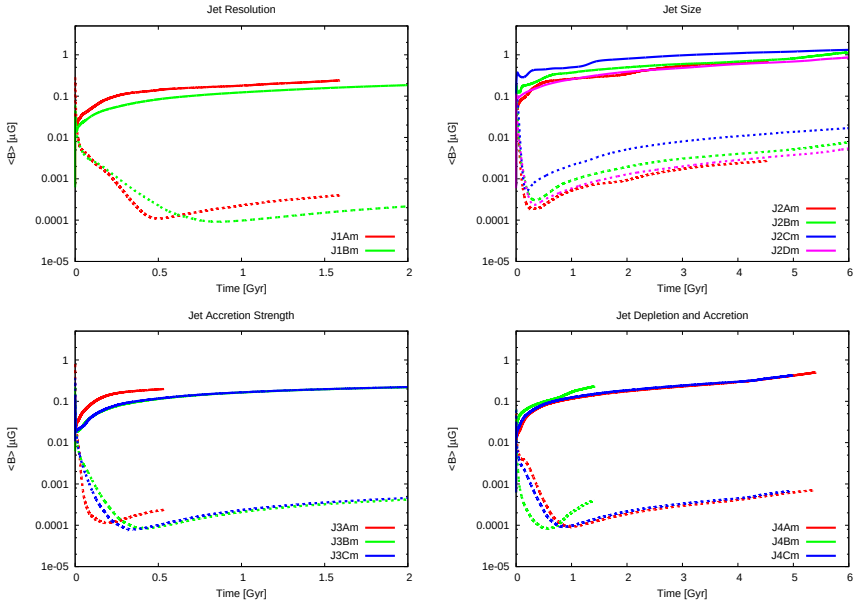

Figure 3.18: Affecting the average magnetic field strength by varying the jet model parameters. Solid lines are density-weighted average fields within $R_{\rm core}$ and dotted lines are volume-weighted fields within R_{200}.

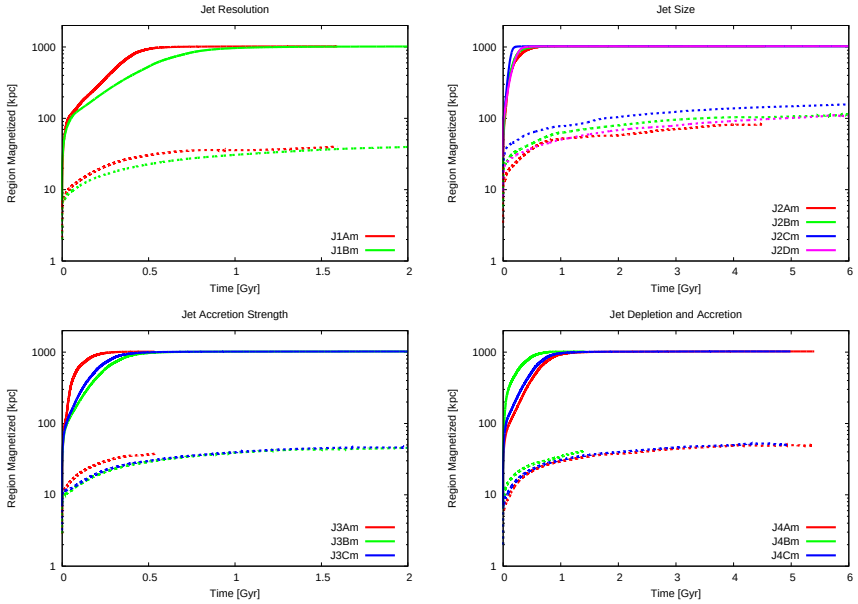

Figure 3.19: Affecting the volume magnetized by varying the jet model parameters. Shown is the cube root of the total volume containing fields of strength at least 10^{-12} G (solid lines) and 10^{-6} G (dotted lines).

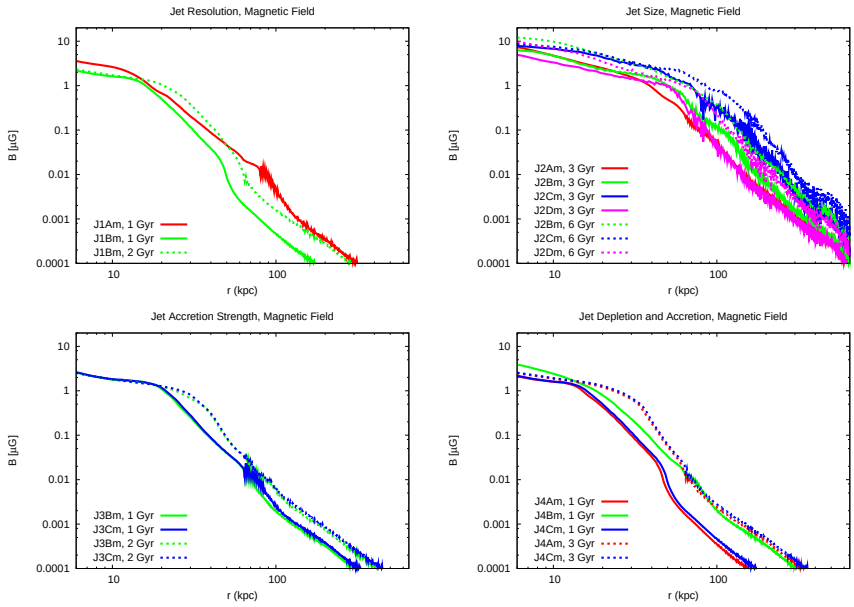

Figure 3.20: Affecting the magnetic profiles by varying the jet model parameters. Shown are volume-weighted magnetic fields as a function of radius.

When we increase α in models J3B and J3C, we see almost no differences in the profiles at 1 and 2 Gyr. Also, there is very little difference between either of these models and the fiducial case. Model J4B, with the larger accretion and depletion radii, produces an order of magnitude stronger field at large radii and nearly a doubling of the field in the inner cluster after only 1 Gyr.

3.7.2 Bubbles

By varying the peak resolution and accretion strength in the bubble models we also see significant differences in the accretion rate, magnetic outflow properties, and overall magnetization of the cluster. The plots in this section are split into two groups: "Bubble Resolution" will contain models B1A-B2E, and "Bubble Accretion Strength" will reference models B2A, B2B, B3A, and B3B.

Our parameter changes significantly affect the accretion rate, as shown in Figure 3.21. First, changing the resolution has a stronger effect on the bubbles than the jets, mostly because we can reduce the resolution much farther than in the jet models and still adequately resolve the bubbles. At the same resolution as the jets (0.5-1.0 kpc) we see very little difference. However, at lower resolutions (4-8 kpc), we begin to see much lower accretion rates as time progresses, reaching an order of magnitude in difference at 5 Gyr. At lower resolutions, we also delay the onset of the formation of highly complex fields by over a billion years, so the simulations can evolve further.

When we vary the accretion strength parameter α, we see much more complicated behavior than in the jets. Whereas the jets maintained self-regulated

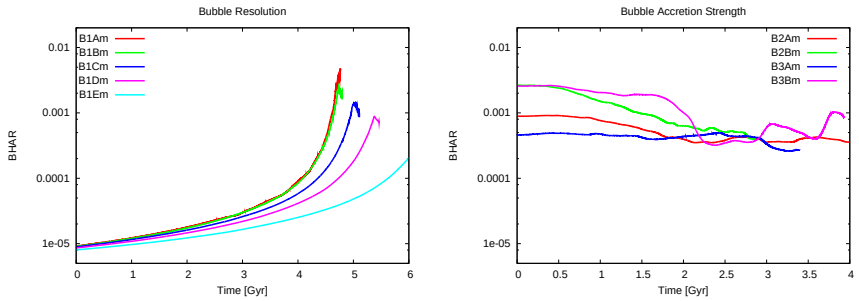

Figure 3.21: Affecting the black hole accretion rate by varying the bubble model parameters. Shown is BHAR ($\dot{M}/\dot{M}_{\rm Edd}$) versus time.

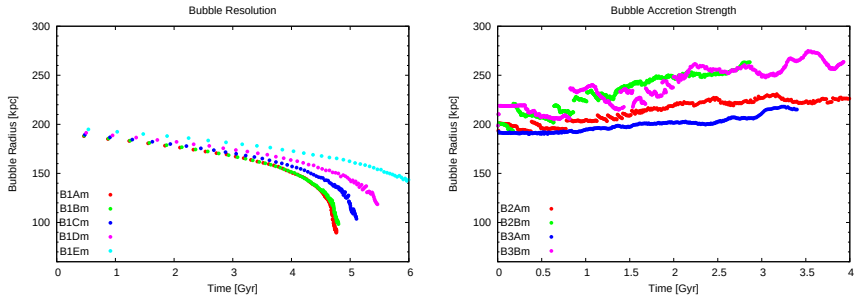

Figure 3.22: Affecting the bubble size by varying the bubble model parameters. Shown is bubble radius at each injection event as a function of time.

behavior, because the continuous jet-based feedback was coupled more tightly to the immediate surroundings of the black hole, the bubbles are much more sensitive to changes in α. As we increase α, as in models B2A and B2B, we see immediate increases in the BHAR. The bubbles, which take time to form and are not as efficient as the jets at driving gas away from the core, only slightly reduce the accretion rate below the amplified value. For example, setting $\alpha = 100$ produces a BHAR only ~ 80 times stronger rather than 100. As we vary the resolution along with α, as in models B3A and B3B, we see that the changes to the accretion strength are dominant over the changes to resolution.

The bubble sizes vary dramatically, as shown in Figure 3.22. Note that as we lower the resolution (and have correspondingly lower accretion rates) our bubbles become slightly *larger*. Since the bubble energy is fixed as a fractional increase in the SMBH mass, at lower resolutions we begin to underestimate the gas density, which both lowers the accretion rate and produces larger bubbles, as Eq. 3.7 suggests. Notice that is also takes longer to produce bubbles at lower resolutions, taking almost twice as long in the 8 kpc case than in the 4 kpc run.

Authors usually invoke an enhanced accretion strength parameter to account for underestimating the gas density at lower resolutions. However, for this cluster our changes to α dominate over changes to resolution. Note especially models B3B and B1B. Model B3B has a resolution of 4 kpc, and an α of 300 should

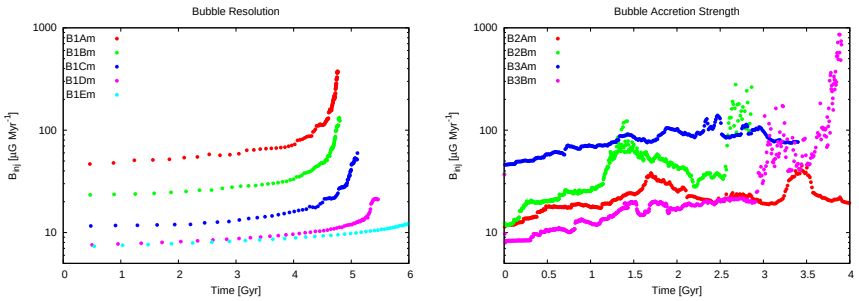

Figure 3.23: Affecting the rate of injected magnetic field strength by varying the bubble model parameters.

account for the resulting under-resolution of the gas density. Instead, model B3B produces many more bubbles with larger radii and begins a periodic cycle within 1 Gyr, which are features absent from model B1B. We also notice some discontinuities, such as in model B3B, where strong bubble events temporarily halt the cooling of gas. All of the runs with increased α produce unphysically-large bubbles (> 200 kpc) with extremely high formation rates (one bubble per 10-20 Myr), suggesting that increasing α may not always be appropriate.

Despite the small changes to the accretion rate and bubble size when changing the resolution, we see dramatic differences to the magnetic injection rate, as shown in Figure 3.23. Even though the injected energy is the same for each bubble event (Eq. 3.6), this energy is distributed over different bubble volumes. Hence, small changes in the bubble radius lead to large differences in the injected magnetic field strength. The smallest bubbles, which occur with $\Delta x = 0.5$ kpc in model B1A, have the largest injected energy, with a $B_{\rm inj}$ for the first bubble over a factor of two larger than that of model B2A, which has a resolution of 1.0 kpc. The trends continue down to 4 kpc. However, at this resolution the bubbles are already so large that at lower resolutions there is little difference in the injected field strength. For all these models the injection rate steadily increases as gas cools and accretes onto the core, eventually producing magnetic fields which are too strong and tangled to simulate further.

With the boosted-α models we again see large differences in $B_{\rm inj}$. However, instead of the steadily increasing magnetic field strength of the $\alpha = 1$ models, small cyclic variations in the accretion rate and bubble size lead to similar, but amplified, patterns in the rate of injected field strength. This is most evident in model B2B, where the injection rate changes by a factor of ~ 5 with a period of roughly 1 Gyr.

The smaller bubbles in the high-resolution runs are more effective at magnetizing the cluster, as we show in Figure 3.24. Reduced numerical dispersion as we increase resolution also plays a role. This figure displays the average magnetic field strength within the core and within the entire cluster. Model B1A is able to generate 1 μG fields within the core in 3 Gyr, where as model

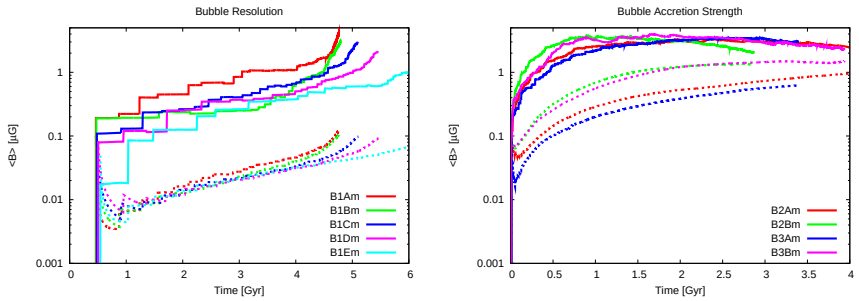

Figure 3.24: Affecting the average magnetic field strength by varying the bubble model parameters. Solid lines are density-weighted average fields within $R_{\rm core}$ and dotted lines are volume-weighted fields within R_{200}.

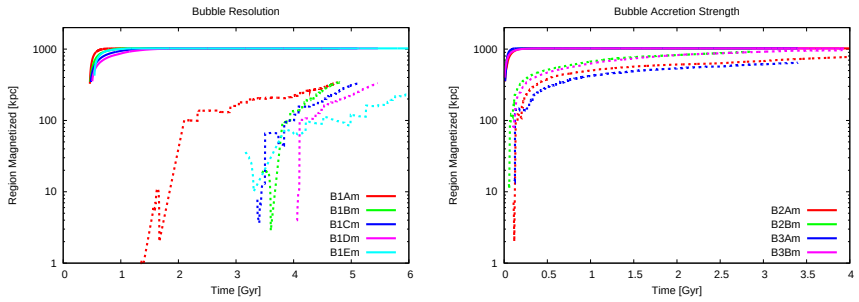

Figure 3.25: Affecting the volume magnetized by varying the bubble model parameters. Shown is the cube root of the total volume containing fields of strength at least 10^{-12} G (solid lines) and 10^{-6} G (dotted lines).

B1D, with 16 times lower resolution, takes twice as long. All of these models produce the same general trends: steadily-increasing magnetic fields both in the core and entire cluster from 1 to 4 Gyr followed by a sharp rise as the accretion intensifies.

When again see the strong dependence on accretion strength parameter: the high-α runs generate > 1 μG fields within the core and > 0.1 μG fields averaged within the entire cluster in less than 1 Gyr. Indeed, models B2B and B3B, with $\alpha = 300$, are able to produce ~ 1 μG fields within R_{200}. The higher the value of α, independent of resolution, the greater the magnetization. The time-dependent behavior of the average field within the cores for these models looks more like the jets than the fiducial bubble case.

In all bubble cases, regardless of changes to the resolution or accretion strength, the cluster quickly magnetizes, as we see in Figure 3.25. However, the high-α models not only magnetize the cluster with weak fields, but also push strong (> 1 μG) fields almost to the cluster edge. The $\alpha = 1$ cases, however, are much less effective at generating these strong fields, with most models only creating these fields after 3 Gyr. These models are also only able to push these fields to a meager ~ 200 kpc radius.

This is also reflected in the radial profiles of the magnetic fields, which we

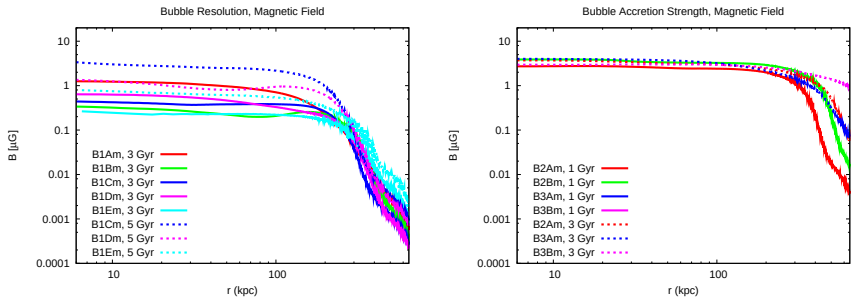

Figure 3.26: Affecting the magnetic profiles by varying the bubble model parameters. Shown are volume-weighted magnetic fields as a function of radius.

show in Figure 3.26. All the high-α models create a region of strong fields out to $\sim$ 400 kpc within only 1 Gyr. This is due to the strength and frequency of these bubbles. After another 2 Gyr of evolution the fields in this same region have doubled in strength. On the other hand, varying the resolution does not produce significant differences until 5 Gyr of evolution. In all these cases, the fields remain relatively constant out to a radius of 200 kpc before steeply falling, and changes to the resolution to not affect this behavior. While higher resolution does result in stronger fields, a factor of 16 difference in resolution only produces a factor of 2 difference in the resulting magnetic fields, even after billions of years of evolution.

3.8 Conclusion

We have conducted a systematic study of the growth and evolution of magnetic fields due to the self-regulated feedback of a central active galactic nuclei within an isolated mock cluster. This study is the first to link the energy available for injected magnetic fields to an accretion rate measured on the simulation mesh. We have implemented magnetic field injection using representative models of continuous small-scale jets and sporadic large-scale bubbles. We have examined the effects of magnetizing the jet and bubble outflows on the accretion properties of the black hole and the thermodynamic quantities of the surrounding cluster gas. We have compared the resulting magnetization of the cluster using a fiducial jet and bubble model in terms of the growth, evolution, and topological structure of the magnetic fields. Finally, we have performed a parameter survey of the jet and bubble models to determine the relationship between subgrid model parameter choices and the resulting magnetic outflow properties.

The relative effects of adding magnetic fields into the injection depends on the choice of subgrid model. Continuous jets, where the feedback is applied to the central few zones, suffer a large decrease in the accretion rate due to the tension forces inherent in the injected magnetic fields. Fixed-position bubbles, with large radii, take roughly 3 Gyr for noticable difference to emerge, while

randomly-placed bubbles are almost entirely unaffected. In general, strong magnetic fields placed near the central black hole are very effective at pushing gas away from the core and preventing cooled gas from accreting.

All models quickly permeate the entire cluster with fields of strength greater than 10^{-12} G and produce strong fields ($> 10^{-6}$ G) in the central core. While jets produce slightly stronger fields in the innermost regions of the cluster, the bubbles more quickly disperse relatively strong fields out to larger radii. Additionally, the bubble models produce flat radial profiles out to ~ 300 kpc, beyond which the field strength drops rapidly. Although the jets produce more realistic-looking radial profiles, they can take up to 4 Gyr to sufficiently magnetize the inner regions of the cluster.

The jets and fixed bubbles maintain regular torus-like shapes in the magnetic field that persist over several billion years with strong fields concentrated in the core, although eventually the fixed bubbles begin to disperse. Thus, if we are to consider the jet or fixed bubble subgrid models as realistic approaches, we must require some external source of turbulence to tangle the generated magnetic fields. The randomly-placed bubbles immediately produce large-scale highly tangled magnetic fields out to relatively large radii. However, the bubbles have difficulties generating magnetic fields with strength greater than a microGauss, something that is relatively easily to accomplish with the fixed bubbles and especially the jets.

We found the jet models to be relatively insensitive to many changes in the underlying model. Since the jets require high resolution in the first place (i.e., < 1.0 kpc) further improvements to the resolution leave the jet outflow properties unchanged. We found that it is necessary to keep the accretion radius smaller than the injection region, but changes to the depletion radius are less important since the accretion rate is so low. We see the biggest differences to the jet outflows when changing jets size. On the other hand, changing the accretion strength parameter has little effect, since stronger jet outflows simply push more gas away from the black hole, reducing the measured accretion rate to nearly its value in the fiducial case.

The bubble models were much more sensitive to changes in the accretion strength parameter, since the injection region is much larger. Even though increasing α is generally used to compensate for lower resolution, we found that the combination of lower resolution with enhanced α did *not* mimic the behavior of a higher resolution simulation with lower accretion strength parameter. Higher values of α led to very large, rapidly-forming bubbles. Thus, we advise caution when choosing a value for α, especially when considering magnetic feedback subgrid models. A value of α chosen to match, for example, the observed $M_{\rm bh} - \sigma$ relation may produce unrealistic bubbles. Furthermore, for this particular cluster, which has a relatively flat inner density profile, we only began to see significant differences when lowering the resolution past ~ 4 kpc.

While the jets appear to be more robust, they have significant difficulties in

quickly and efficiently magnetizing the cluster. They must require some additional mechanisms operating in the intracluster medium to spread and tangle the injected fields. On the other hand, the randomly-placed bubbles, which automatically generate rich, tangled magnetic field morphologies, are more sensitive to subgrid model choices. Additionally, our fiducial case - with parameters taken directly from Sijacki et al. (2007) - produces very large bubbles very rapidly, which suggests that this model is not appropriate for general cluster atmospheres. Since the fixed bubbles have a predetermined radius they do not face this problem. While they also produce somewhat ordered fields, they spread these fields out to larger volumes, which makes these fields more susceptible to tangling from cluster mergers and galaxy motions. They can also strongly magnetize the cluster very quickly - in less than 1 Gyr.

While we have performed a relatively exhaustive analysis, many questions remain. Primarily, these magnetic field models must be tested in more realistic clusters to determine their ability to sufficiently magnetize the clusters absent any assumptions about the strength of the injected magnetic fields. Secondly, we must use these resimulated clusters to more fully evaluate these magnetized outflows in terms of observables, such as AGN duty cycle and cluster X-ray luminosity profiles. We must study more topologies of magnetic injection, such as random fields, to determine if the resulting magnetic outflows are robust against changes to the injected field structure. Finally, we must perform fully cosmological simulations to ensure that the given AGN subgrid models, when injected magnetic fields are included, reproduce key observables, such as the relationship between supermassive black hole mass and host galaxy bulge velocity dispersion. Only then can we be confident that our magnetic subgrid models accurately represent realistic aspects of AGN evolution, and use them to evaluate the ability of active galactic nuclei to generate cluster-wide magnetic fields.

Chapter 4

Examining subgrid models of supermassive black holes in cosmological simulation

4.1 Introduction

This chapter contains work previously published in Sutter & Ricker (2010). Supermassive black holes (SMBHs) play a number of roles in the evolution and dynamics of galaxies and clusters of galaxies. These black holes, with masses of at least a million solar masses, and their associated accretion disks drive quasars at high redshift (Fan 2006), regulate star formation in galaxies (Hopkins et al. 2010), inject thermal energy into the intracluster medium via powerful jets (Gu et al. 2009), and may even play a large role in establishing kiloparsec-scale microgauss magnetic fields in clusters (Carilli & Taylor 2002).

Of particular interest are the correlations discovered between SMBH mass and other observed quantities of galaxies. The first discovered relationship, between SMBH mass and bulge stellar luminosity (Magorrian et al. 1998), was intriguing but suffered from large scatter. Subsequent searches found a tight correlation between SMBH mass and bulge velocity dispersion σ (Tremaine et al. 2002; Gültekin et al. 2009), although comparable improvements have also been made in the correlations to stellar luminosity (Graham 2007). Most recently, black hole mass has been linked to dark matter halo mass $M_{\rm tot}$, both indirectly by measuring galactic circular velocities (e.g., (Ferrarese 2002); (Baes et al. 2003)) and by direct estimates of halo mass via gravitational lensing (Bandara et al. 2009). The latter measurements agree well with theoretical predictions of the relationship between halo virial mass and galactic circular velocity (Croton 2009).

These relationships imply a correlation between the growth of SMBHs and that of their host galaxies. Since structures form in the universe via hierarchical clustering of smaller objects (Baugh 2006), black holes carried along with their hosts should tend to merge as well (Hopkins et al. 2010). This may provide a simple and direct scaling between halo and black hole mass, especially at low redshift (Volonteri et al. 2003). However, feedback processes driven by accretion disk systems may also contribute to the observed correlations: greater accretion

can lead to larger feedback events, thereby reducing the accretion rate and coupling the black hole mass to the surrounding system (Cattaneo & Teyssier 2007).

Attempts to explain the observed relations via cosmological simulations require large volumes (to gather enough objects) and high resolution (to capture galaxy-sized structures). However, even with current computing resources, large-volume simulations are unable to capture all the intricate physical processes that dominate in the formation, merging, and feedback of black holes. Hence, these processes must be added in post-processing as semi-analytic models (e.g., Micic et al. 2007) or included in-situ as subgrid models (e.g., Booth & Schaye 2009 ; Sijacki et al. 2007 ; Di Matteo et al. 2008).

Many processes have been proposed to explain the formation of seed SMBHs in the early universe, including remnants of Population III stars (Madau & Rees 2001; Wise & Abel 2005), direct collapse of gas in central bulges (Koushiappas et al. 2004; Begelman et al. 2006), and merging of smaller black holes (Islam et al. 2004). Merging black holes are difficult systems to study, since they interact with their gaseous environment (Mayer et al. 2007), emit gravitational radiation (Sesana et al. 2004), and can suffer kicks due to merging (Baker et al. 2008). Additionally, the self-regulating feedback processes emerging from accretion onto black holes and the subsequent formation of jets and bubbles are not fully understood (Vernaleo & Reynolds 2006), especially when considering the effects of magnetic fields (Ruszkowski et al. 2007) and turbulence (Brüggen & Scannapieco 2009). Consequently, subgrid models must make many simplifying assumptions in treating these processes.

The variety of plausible scenarios for forming and merging black holes and applying feedback processes allows modelers great latitude in developing and adjusting models to fit observations. Universally, all aspects of the formation and evolution of SMBHs are combined in the same simulation. However, we believe that subgrid models of the initial seeding and merging of SMBHs (which are linked in subgrid models to the properties of the surrounding dark matter) should be separated from models of accretion and feedback (which depend on the local gas physics). This way, we can better understand the role that merging alone plays in developing the $M_{\rm bh} - \sigma$ and $M_{\rm bh} - M_{\rm tot}$ relations and the effects of changing subgrid models on those same relations.

Thus, in this paper we examine dark matter-only simulations of the growth of structure in a cosmological volume including subgrid models to track the formation and merging of SMBHs. By comparing the results of several plausible scenarios for models against observed relations, we will determine how much of those relations is due to low-redshift and large-scale evolution of SMBHs, and how these models may affect the final outcomes, independent of any gas accretion or feedback.

To follow our dark matter halos, we have developed a new, parallel, fast halo finder built directly into the simulation code FLASH v2.5. FLASH is an

adaptive-mesh refinement (AMR) code for astrophysics and cosmology (Fryxell et al. 2000). FLASH solves the N-body potential problem with a particle-mesh multigrid fast Fourier transform method (Ricker 2008). It uses smoothed cloud-in-cell mapping (Ricker et al. in preparation 2010) for interpolating between the mesh and particles (Hockney & Eastwood 1988) and a second-order leapfrog integration scheme for variable time step particle advancement.

In the following section we discuss the precision and valid mass ranges for our new halo finder. In Section 4.3 we outline the numerical aspects of our approach and the black hole formation and merging subgrid models employed. Finally in Section 4.4 we compare our results to observations of the $M_{\rm bh} - \sigma$ and $M_{\rm bh} - M_{\rm tot}$ relations to test the validity of the models. Additionally, we provide a discussion and analysis of the performance and parallel scalability of our halo finder in the Appendix.

4.2 The halo finding method

We base the halo finder in FLASH on a spherical-overdensity (SO) technique. Throughout, we will identify our new halo finder by "pSO", for parallel spherical overdensity. In this approach, halos are defined by spherical regions within which the mean density is greater than some defined threshold. We begin by mapping particles onto the simulation mesh with smoothed cloud-in-cell mapping and identifying peaks by finding zones with densities greater then all surrounding zones and greater than $\Delta_{\rm peak}\rho_{\rm crit}$. Here and throughout, $\rho_{\rm crit}$ refers to the comoving critical density of the universe,

$$\rho_{\rm crit} = \frac{3H_0^2}{8\pi G}\left[\Omega_{M,0} + \Omega_{\Lambda,0}(1+z)^{-3}\right], \tag{4.1}$$

where subscripts of 0 here and throughout refer to present-day values. The zone midpoints serve as centers of potential halos. Using a binary search, we compare the average density within the current search radius to $\Delta_{\rm search}\rho_{\rm crit}$, selecting new search radii appropriately. Initially, search radii are doubled until the enclosed density is below the threshold. Only then does the binary procedure begin. When two successive search radii differ by no more than a chosen amount, defined by the parameter $\Delta R_{\rm stop}$, we stop the search. If, during the search, a radius falls below a cutoff value, $\Delta R_{\rm small}$, we the abort the search and disregard the halo. Finally, we remove any finished halos that have radii smaller than $\Delta R_{\rm min}$ from the catalog. We also remove satellite halos whose centers fall within the radii of larger companions. This leads to a more consistent mass function and conserves halo mass (White 2002). We may also optionally remove satellite halos which intersect larger neighbors. While this must be done to strictly conserve halo mass, many authors include these satellite halos, since it is sometimes useful to identify satellite structures (see the comparison in Evrard et al. (2008) for a discussion of this decision). Table 4.1 lists the parameters

Table 4.1: Parameters controlling the pSO halo finder in FLASH.

Parameter	Description	Value
$\Delta_{\rm peak}$	Overdensity for identifying a halo center	$200\rho_{\rm crit}$
$\Delta_{\rm search}$	Overdensity for defining a halo	$200\rho_{\rm crit}$
$\Delta R_{\rm stop}$	Criterion for completing a radius search	$0.2\Delta x$
$\Delta R_{\rm small}$	Criterion for aborting a radius search	$0.5\Delta x$
$\Delta R_{\rm min}$	Minimum resolvable halo radius	$1.0\Delta x$

controlling our halo finder and our chosen values. In the table and throughout, Δx is the grid resolution. Note that for simulations in which the halos may span an adaptively refined region, Δx will refer to the highest-resolution uniformly refined mesh level.

For this work, we chose $\Delta_{\rm peak} = \Delta_{\rm search} = 200$. However, other values may be chosen for other uses of the halo finder. For example, $\Delta_{\rm search} = 500$ would be appropriate for generating mock observations of X-ray cores for comparison to observations (Evrard et al. 1996), while a smaller value might be useful for triggering refinement.

To evaluate our halo finder, we performed dark matter-only simulations in a cubic 128 h^{-1} Mpc box with 256^3, 512^3, and 1024^3 zones, giving resolutions of $\Delta x = 500$, 250, and 125 h^{-1} kpc respectively. All runs used 256^3 particles, giving a mass resolution of 1.3×10^{10} $M_\odot$. For these tests, we chose cosmological parameter values of $\Omega_{M,0} = 0.26$, $\Omega_{\Lambda,0} = 0.74$, and $H_0 = 100h = 71$ km s^{-1}Mpc^{-1} for comparison to runs used in previous works. We compared our pSO halos against spherically overdense regions drawn from a friends-of-friends (FOF) halo finder with a linking length of 0.2 (see Lukić et al. 2009 for an analysis of SO halos drawn from an FOF catalog). The halos drawn from the FOF catalog used the most-linked particle as the halo center. Halo radii in the FOF catalog were determined by starting with a large radius and moving inwards at very small increments (much smaller than the $\Delta R_{\rm stop}$ used in pSO) until the interior density exceeded the same threshold as used by the pSO halo finder. This approach is more precise, but much slower, than the binary search technique used in pSO. We use a linear search here since with such high precision a binary technique may not complete.

We thus have several possible sources of differences between the SO and FOF halo catalogs: (1) pSO chooses the zone midpoints as the halo centers, while FOF halos use the most-linked particles, (2) the incremental search radii when finding spherical overdense regions in the FOF catalog are much smaller than those used in pSO, (3) FOF tends to find more small halos than the grid-based peak finding in pSO, since smaller halos may be irregularly shaped, and (4) FOF will tend to bridge two nearby halos, even if they have distinct spherically overdense regions.

Figure 4.1 demonstrates both the problem of selecting a halo center and that of pSO counting more satellite halos than FOF. Shown is a $\sim 10^{14}$ h^{-1} M$_\odot$ halo

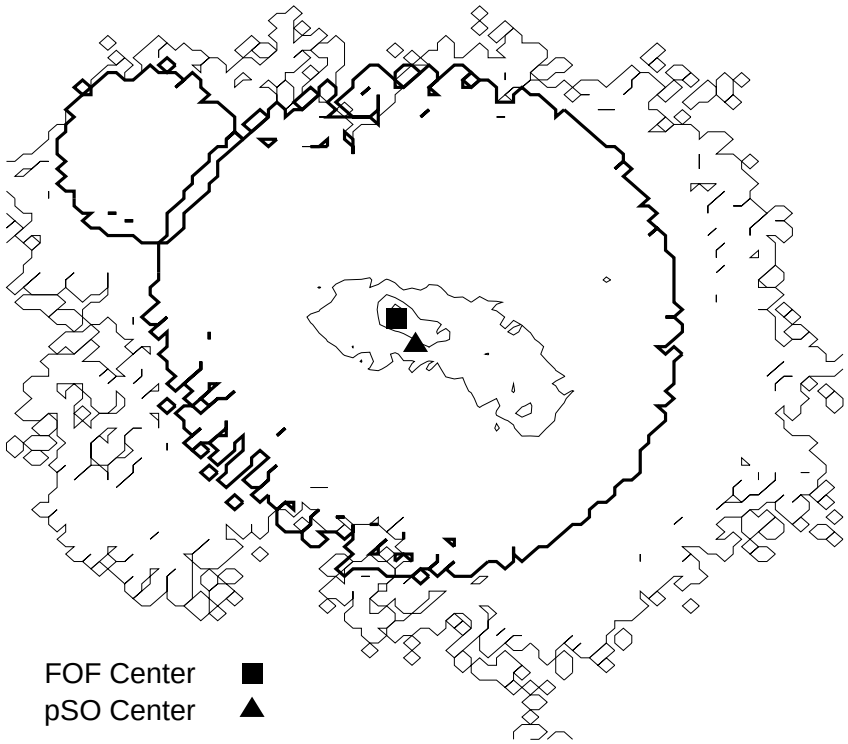

Figure 4.1: Demonstration of different choices of halo center due to recent merging. The thin lines indicate projected density contours of the FOF halo. The interior contour lines define thresholds of 50 and 200 particles per zone, while the outermost contour shows a threshold of 1 particle per zone (i.e., the boundary of the FOF halo). The two thick circles show the boundaries of the spherically overdense regions identified by pSO. The separation of the larger pSO halo center (circle) and the FOF halo center (square) is roughly one half a zone.

drawn from the run with 250 h^{-1} kpc resolution. This halo is undergoing a merger with a smaller satellite, and thus FOF is bridging two distinct spherical regions into a single halo. In agreement with the findings of Evrard et al. (2008), we find roughly $\sim 15\%$ of our halos are satellites. While the most-linked particle approximates the potential minimum well, the pSO halo center, which is simply the zone midpoint, is within a zone radius of this point. The bridging effect leaves the smaller pSO halo unmatched.

We match halos in the pSO and FOF catalogs by finding intersections. Any halos from the two catalogs that overlap such that they contain each other's centers are considered a match. Due to the ambiguity of halos with very few particles, we only compare halos with more than 100 particles. With this procedure alone, about 15% of the pSO halos remained unmatched. To determine if this was due to the FOF bridging effect, we removed from consideration any pSO halo that was within a linking length of an already matched FOF halo. This accounted for all the unmatched pSO halos.

To account for the effects of choice of halo center, we re-computed overdensities in the FOF catalog using the potential minimum halo centers found in the matching pSO catalog. Note that we found that the differences between halo centers were always smaller than a zone spacing. There may be some cases, however, where a large asymmetry will separate the most-linked particle and the maximum density peak further than a zone spacing, especially at very high resolutions. Here, asymmetries will manifest themselves in a higher relative error between matched halos. Figure 4.2 shows errors in the matched halos in the 125 h^{-1} kpc catalog at $z = 0$ before and after recentering. We define the errors as the difference in mass divided by the sum of the 1σ uncertainties in the halo mass:

$$E \equiv \frac{|M_1 - M_2|}{\sigma_{\mathrm{M}_1} + \sigma_{\mathrm{M}_2}}. \tag{4.2}$$

We estimate the halo mass uncertainty by assuming an uncertainty in the halo radius of $0.5\Delta x$. Thus, assuming constant halo density, the mass uncertainty is

$$\sigma_{\mathrm{M}} = \frac{3}{2}\frac{M}{R}\Delta x \propto M^{2/3}, \tag{4.3}$$

where M and R refer to the halo mass and radius, respectively. For halos above 10^{14} $M_\odot$ in mass, this leads to $\sigma_{\mathrm{M}}/M \approx 0.1$, which agrees with the estimates of Bhattacharya et al. (2010). While most matched halos have small error, a few differ by as much as 0.7, especially at lower masses. However, most of this is due to the bridging effect's having moved the most-linked particle away from the potential minimum. After recentering, errors for all halos larger than a zone radius drop to below 0.1. The small gap in halo sizes near $R_{200}/R_{\mathrm{zone}} = 0$ is due to our choice of ΔR_{stop} and the binary search procedure.

Also from Figure 4.2 we find that even after recentering, halos smaller than a zone do not match well to FOF halos. Thus we set the parameter ΔR_{min} to $1.0\Delta x$ and reject any halo smaller than this. Given a resolution, this sets our minimum resolvable halo mass. Note that this criterion is consistent with the estimate for minimum resolvable mass for FOF halos as defined by Lukić et al. (2009):

$$n_{\mathrm{min}} = \frac{\Delta(1.61 n_p/n_g)^3}{\Omega_{M,0}(1+z)^3}\left[\Omega_{M,0}(1+z)^3 + \Omega_{\Lambda,0}\right], \tag{4.4}$$

where n_g and n_p are the number of zones and particles per side, respectively, and $\Delta = 200$ is our chosen overdensity.

Figure 4.3 shows maximum and average errors after recentering for each of 10 mass bins at $z = 0$ for each simulation resolution. With our approach, we are able to maintain average errors of less than 0.04 for all resolvable halos, while a small number ($< 5\%$) of halos have maximum errors of up to 0.12. Although the average error stays consistent across all masses, the maximum error varies as much as 0.04 for adjacent bins, and it rises with decreasing mass. This behavior is due to a small number of irregularly-shaped halos. Also, since smaller halos

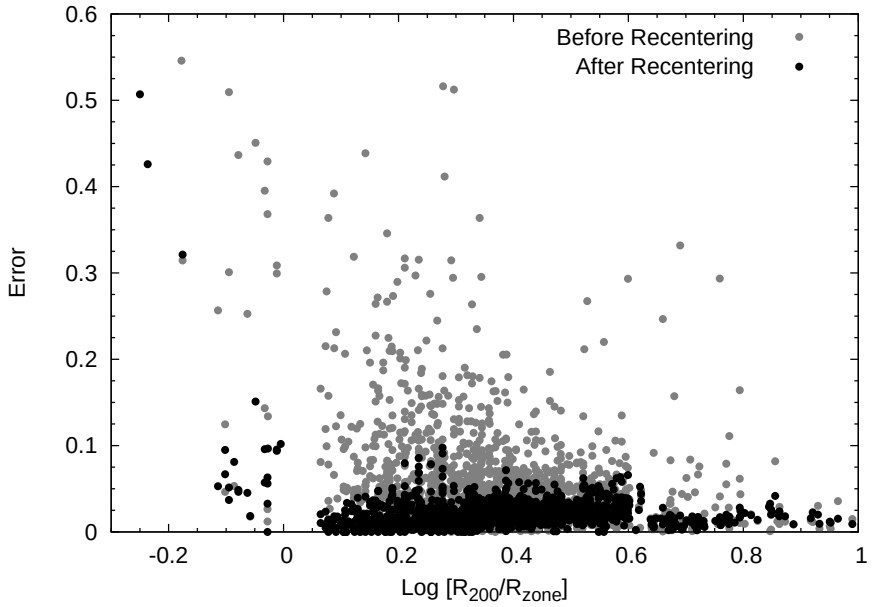

Figure 4.2: Error in matched halos before and after recentering FOF halos on pSO centers, as a function of halo radius. The error is defined in the text.

have smaller uncertainties, the errors tend to become larger with smaller halo mass.

Figure 4.4 shows errors after recentering at various redshifts in the $\Delta x = 125\ h^{-1}$ kpc run. Across all resolvable masses and redshifts from $z = 0$ to 2, we are able to maintain average errors less than 0.05. However, maximum errors in the smallest mass bins reach as high as 0.18. Again, the variability of the maximum errors is due to a small number of halos.

By adjusting $\Delta R_{\rm stop}$, we are able to reduce both the average and maximum errors. However, at smaller values we found that the binary search procedure had difficulty converging on a value for some halos, and the halo finder ran for an unacceptable amount of time. Larger values produced unacceptably high errors. For the value we chose, after accounting for different choices of halo center, the halos produced by our new pSO halo finder are statistically indistinguishable from matched halos drawn from a traditional FOF halo finder.

Figure 4.5 shows the mass function for the pSO halo catalogs at the three resolutions compared to SO halos drawn from an FOF catalog with a resolution of 125 h^{-1} kpc and compared to the mass function obtained by Warren et al. (2006). As expected, pSO captures more halos as the resolution increases. However, pSO captures fewer halos near the resolvability limit than FOF does. The procedure for mapping and smoothing tends to lower the central density, especially with halos near the resolvability limit. Thus our criterion for selecting a peak, $\Delta R_{\rm peak} = 200$, may be too stringent. We found that lowering this value captures more halos, but at the expense of identifying too many potential

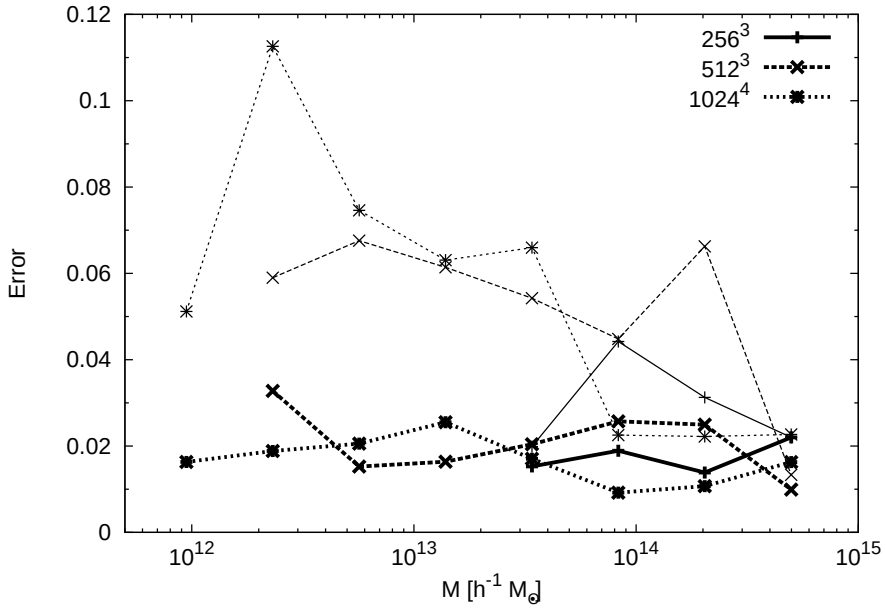

Figure 4.3: Error in matched halos at different simulation resolutions. Bold lines denote average error, while thin lines describe maximum error for each mass bin. The error is defined in the text, and is computed after recentering.

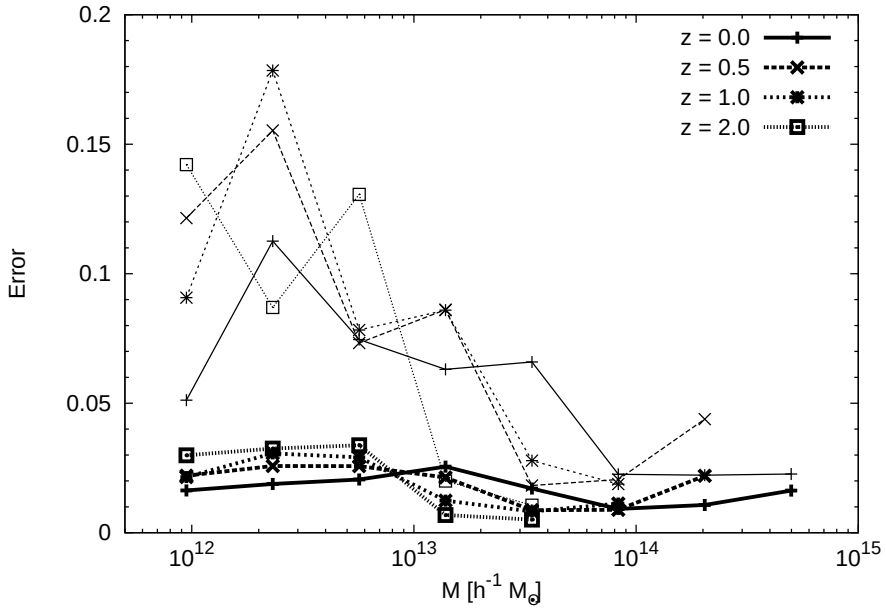

Figure 4.4: Error in matched halos at different redshifts for run with 125 h^{-1} kpc resolution. Bold lines show average error for each bin, while thin lines denote maximum error. The error is defined in the text, and is computed after recentering.

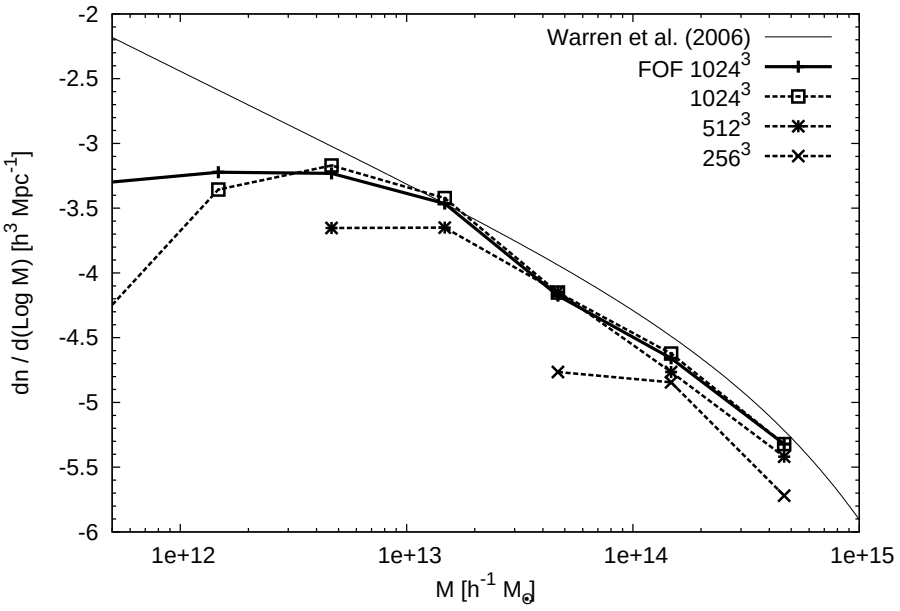

Figure 4.5: Mass functions at different resolutions compared against halos drawn from the 125 h^{-1} kpc resolution FOF catalog and against the mass function from Warren et al. (2006).

halos that end up below the resolvability limit. Even at values as low as 100, we still could not replicate the FOF mass function at these masses, while adding roughly four times as many candidate halos that were ultimately rejected.

Finally, to speed up processing we may increase $\Delta R_{\rm small}$. However, the binary search may briefly fall below this threshold before settling on a larger, and correct, radius. Thus we want to pick the largest possible value that does not cause us to remove resolved halos. We found that at any values above $0.5\Delta x$ we began to reject valid halos before their search had completed.

4.3 Subgrid models

We identified three areas in which subgrid models may differ: the initial mass of seed black holes, the prescription for determining if two black holes merge, and the frequency of finding halos, creating black holes, and checking for mergers. For each of these aspects we study two possibilities: a "pessimistic" and an "optimistic" scenario. This leads to a total of eight combinations of models.

For the initial mass of seed black holes, authors who have performed calculations similar to ours (e.g., Booth & Schaye 2009 ; Sijacki et al. 2007 ; Di Matteo et al. 2008) typically choose a constant seed mass of 10^5 $M_\odot$, and this is the value we will choose for this model. The value chosen is typically motivated by a desire not to violate constraints on the observed black hole mass density (Shankar et al. 2004), especially when black holes are allowed to accrete

a significant portion of their final mass.

However, this approach may have several weaknesses. First, black holes with masses as high as $10^9\ M_\odot$ are inferred to exist from quasar activity at $z \sim 6$ (Fan 2006). Second, depending on the frequency of halo finding, when halos are initially detected they may not have identical masses, and if whatever physical processes which create the observed relations are already present, then the seed black holes should scale with halo mass. Finally, at lower redshifts the halo finding algorithm may spuriously merge two halos. If we instantly merge black holes and in the following step the halo finder identifies two separate halos, one will be without its black hole. It may be inappropriate to re-seed the halo with a low-mass black hole.

Alternatively, we may derive the seed black hole mass from a form of the observed $M_{\rm bh} - \sigma$ relation. This approach may seem tautological; however, accretion and feedback processes may dominate at high redshift and at scales below which we can resolve (Shankar 2009; Merloni et al. 2010). The observed $M_{\rm bh} - \sigma$ relation at $z = 0$ may then simply be a consequence of pure merging at late times and large scales. Also, this approach may be useful in testing other SMBH-related processes and relations in groups and clusters. However, this approach is complicated by the fact that calculations of σ directly in simulations suffer from high scatter, especially at high redshift when halos first form and at low redshift when satellite halos may be contaminated by hot particles belonging to a larger neighbor. Fortunately, we may seed halos by relating the black hole mass directly to the halo mass through the observed relation (Bandara et al. 2009):

$$\log\left(\frac{M_{\rm bh}}{M_\odot}\right) = (8.18 \pm 0.11) + (1.55 \pm 0.31)\log\left(\frac{M_{\rm tot}}{10^{13}\ M_\odot}\right). \tag{4.5}$$

This relation comes from observations at $z = 0.2$ of bulge velocity dispersions and halo masses using gravitational lensing. These measurements are linked to black hole mass by assuming the $M_{\rm bh} - \sigma$ relation of Gültekin et al. (2009):

$$\log\left(\frac{M_{\rm bh}}{M_\odot}\right) = (8.12 \pm 0.11) + (4.24 \pm 0.31)\log\left(\frac{\sigma}{\sigma_0}\right), \tag{4.6}$$

where $\sigma_0 = 200$ km s^{-1}. We will assume the relation in Eq. 4.5 holds to high redshift.

Figure 4.6 shows velocity dispersion as measured in one of our runs (detailed below) as a function of mass at $z = 0.2$. While we agree with observations and the best fit from a suite of simulations described by Evrard et al. (2008), there is significant scatter, especially at low mass. Note that since we are performing dark matter-only simulations, we do not directly measure the velocity dispersion of the galactic central bulge; instead we measure that of the dark matter in the

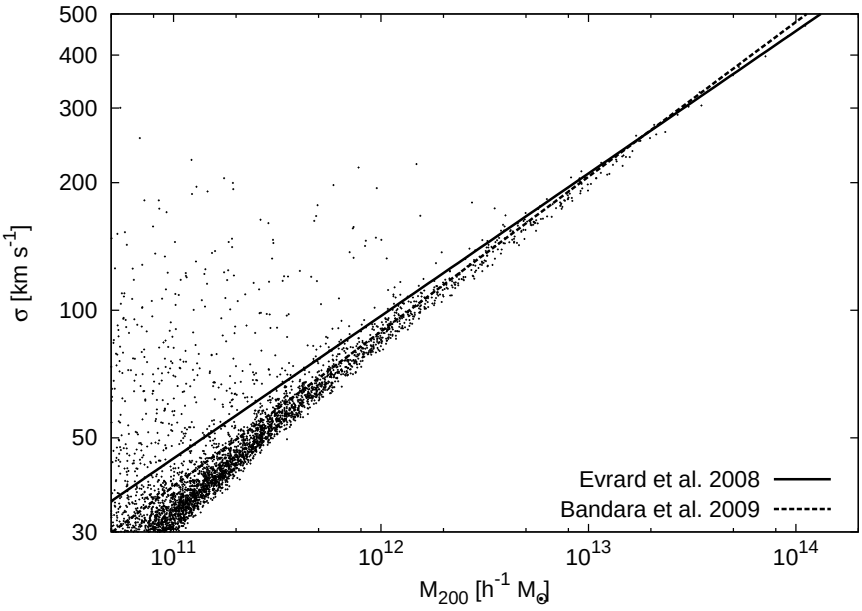

Figure 4.6: $\sigma_{\rm DM}$ as a function of halo mass at redshift $z = 0.2$, compared to observations (Bandara et al. 2009) and best fits from simulations (Evrard et al. 2008). The latter is an extrapolation below $\sim 10^{14}\ M_\odot$.

entire halo, defined by:

$$\sigma_{\rm DM}^2 = a(t)^2 \frac{1}{3N_p} \sum_{i=1}^{N_p} \sum_{j=1}^{3} |v_{i,j} - \bar{v}_j|^2 \,, \tag{4.7}$$

where $a(t)$ is the scale factor, N_p is the number of particles in the halo, $v_{i,j}$ is the jth velocity component of the ith particle, and $\bar{v}_j$ is the jth component of the center-of-mass velocity. Note that velocities in the simulation are comoving quantities. This plot and other results (as summarized by Croton 2009) indicate that $\sigma_{\rm DM}$ and $\sigma_{\rm bulge}$ agree to within a factor of order unity, so we may substitute one for the other.

Next, we may change the prescription for testing black hole mergers. Most approaches to studying the growth of SMBHs rely on halo merger histories derived from simulations (Micic et al. 2007) or Press-Schechter models (Menou et al. 2001; Volonteri et al. 2008). These approaches assume that each halo contains a single SMBH, and whenever two halos merge their respective black holes instantly merge as well. While this approach is highly optimistic, it does provide an upper limit to predicted merger rates, an important constraint on upcoming gravitational wave experiments (Amaro-Seoane et al. 2007). It is also easy to implement and provides a simple way to compare results from simulations to approaches based on merger trees. However, this approach can lead to spurious black hole mergers, since halos may temporarily intersect without

merging. We will include this scenario in our study.

Subgrid models used directly in simulations (e.g., Booth & Schaye 2009) have used a more sophisticated approach in merging black holes. In these simulations, SMBHs only merge when they are within some defined distance (for Lagrangian codes, this is typically the softening length) and have relative velocities below some threshold. This is to avoid merging black holes that are only passing by each other and are not part of a true coalescing system. The velocity threshold varies by author, but it is usually taken to be the local gas sound speed or the circular velocity near the larger black hole of the merging pair. However, we found this test to be overly restrictive; without gas to slow down black holes in cluster cores, merging times inferred from these criteria are larger than the Hubble time and hence almost no black holes merge using this model. Since observations indicate that black holes do merge (Merritt & Milosavljević 2005), we must apply a less stringent test.

Simulations of merging galaxies suggest that the time for black holes to move from kiloparsec to parsec scales is typically ~ 10 Myr (Dotti et al. 2007). This assumption was used in the merger-tree analysis of Micic et al. (2008). When applying this test we will ignore the effects of gravitational recoil (Bogdanovic et al. 2007) and the "final parsec problem" (Berczik et al. 2006). Thus, in this merging test we will only merge black holes if they are both within the same halo and are within two grid zones of each other, and their relative velocity times 10 Myr is less than that same distance. This approach allows black holes to pass near each other without merging if they are not part of a truly merging system and accounts for the time needed for the black holes to merge below our resolvable scales.

Finally, we may alter the frequency of performing our subgrid analysis. One common approach is to check for new black holes and allow mergers such that the interval between successive checks is evenly spaced in the log of the expansion factor. Booth & Schaye (2009) employ the shortest such interval, such that $a_{\rm next} = 1.02 a_{\rm current}$. This approach requires roughly 1/6 the number of halo searches compared to searching every time step. Since our halo finder is designed to be inexpensive, we may perform checks at every time step. This may cause spurious formation and merging of black holes, especially with small halos near the resolvability limit. However, with infrequent checks we may miss the formation and merging of new small halos, underestimating both the amount of black hole mass and the merger rate in the simulation. We will study checking both every time step and at an interval of $\Delta \log a = \log 1.02$.

Table 4.2 summarizes the aspects of the subgrid model we are studying, our choices for modifying each aspect, and a shortened name that we will use to identify the models in plots and tables. For example, a model that uses a constant initial seed mass, merges black holes instantly, and performs a check at every time step would be identified by "con,halo,dt". We note that the most commonly used model in the literature uses a combination of uniform initial

Table 4.2: Aspects of SMBH creation and merging subgrid models.

Aspect	Model	Short Name
Seed mass	Constant	con
	$M_{\rm bh} - \sigma$ relation	m-s
Merging strategy	Instantly on halo merger	halo
	Distance and velocity test	prox
Frequency	Every time step	dt
	Evenly spaced in $\log(a)$	log

mass, velocity tests at every time step for merging, and seeding new black holes evenly in log expansion factor. For our study, we have combined merging tests and seeding in the same step. This is closer to the approach used in merger tree analysis, where analysis can only take place on the available halo catalogs.

4.4 Comparison of models

For all calculations, we used concordance parameter values of $\Omega_{M,0} = 0.238$, $\Omega_{\Lambda,0} = 0.762$, and $H_0 = 100h = 73.0$ km s^{-1} Mpc^{-1}. All runs took place in a three-dimensional box measuring 50 h^{-1} Mpc per side with 512^3 particles and 1024^3 zones per side, giving a mass resolution of 6.15×10^7 h^{-1} M$_\odot$ and spatial resolution of 48.8 h^{-1} kpc. There was no refinement of grid spacing. All simulations used the same initial conditions: unperturbed particle positions were situated on a grid, and the initial velocities and positions were perturbed using Gaussian fluctuations normalized to $\sigma_8 = 0.74$. We assumed $P(k)$ from a ΛCDMcosmology. We used the GRAFIC2 code (Bertschinger 2001) to generate these initial conditions. All computations started at a redshift of $z = 56.8$.

Using our halo finder, our minimum resolvable halo mass is $\sim 10^{10}$ $M_\odot$. To help avoid spurious mergers, we did not include satellite halos (halos that intersect a larger neighbor) in the halo catalog used by the seeding and merging models. We seed black holes in any resolvable halo by creating a black hole particle in the simulation with a dynamical mass equal to the mass of the black hole and velocity equal to the center-of-mass velocity of the parent halo. When we merge black holes, we remove the smaller of the pair and add its mass to the larger of the pair. The larger SMBH maintains its position and velocity. We do not re-center black holes on halo potential minima.

While re-positioning black holes at potential minima reduces ejections due to scattering, this process may artificially promote merger rates. With our SMBH setup, we do indeed see a large ejection rate. Fortunately this is not an issue for our analysis: the vast majority of ejections are of un-merged black holes from low-mass halos at high redshift. Consequently, small black holes are simply replaced by another small black hole, and the merger rates and relations remain unaffected. Obviously, this would pose a problem for models that include accretion. The ideal solution in this case would be to initialize on halos well above

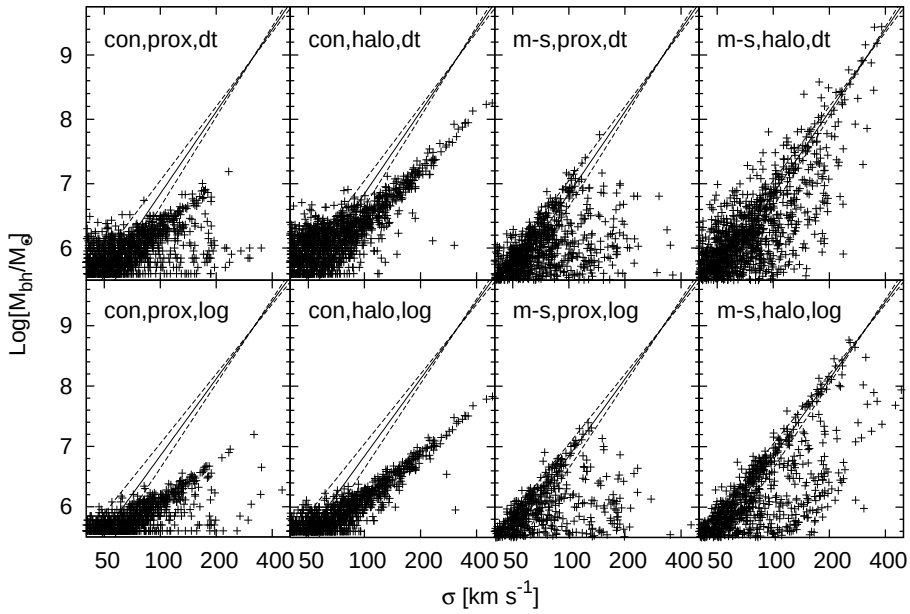

Figure 4.7: Comparison of models (shown as points) against the observed $M_{\rm bh} - \sigma$ relation at $z = 0$ (solid line). Dashed lines indicate 1σ uncertainty bounds in the observed relation.

the minimum resolvable halo mass and to adequately smooth the gravitational potential near the SMBH so that it does not experience significant two-body effects. Also, by using the black hole mass as the dynamical mass, we may underestimate the dynamical friction. However, we have found that almost all black holes lie within a zone of their host's potential minimum, so this does not affect the merger rate.

We compare the results of our simulations to the known $M_{\rm bh} - \sigma$ relation at $z = 0$ (Eq. 4.6) in Figure 4.7 and to the observed $M_{\rm bh} - M_{\rm tot}$ relation at $z = 0.2$ (Eq. 4.5) in Figure 4.8. We have arranged these plots such that the most "pessimistic" combinations of models — constant initial mass, distance and velocity tests for mergers, and new halo and merger checks evenly spaced in $\log a$ — are located in the lower-left portions of the plots, while the most "optimistic" scenarios are in the upper right. Our choice of model can greatly affect a number of aspects of SMBH relations, including the scaling of SMBH mass with σ and $M_{\rm tot}$, the maximum mass of an SMBH, and the amount of scatter in the produced relations.

Models with instant SMBH mergers produce relations with somewhat lower scatter, especially at higher masses, and generated higher maximum black hole mass than models with distance and velocity checks for mergers. For "prox" models, larger halos may contain several unmerged SMBHs, and spurious halo mergers do not lead to mergers of the black holes. These cause even the most massive halos to host relatively small black holes. Additionally, the difference in

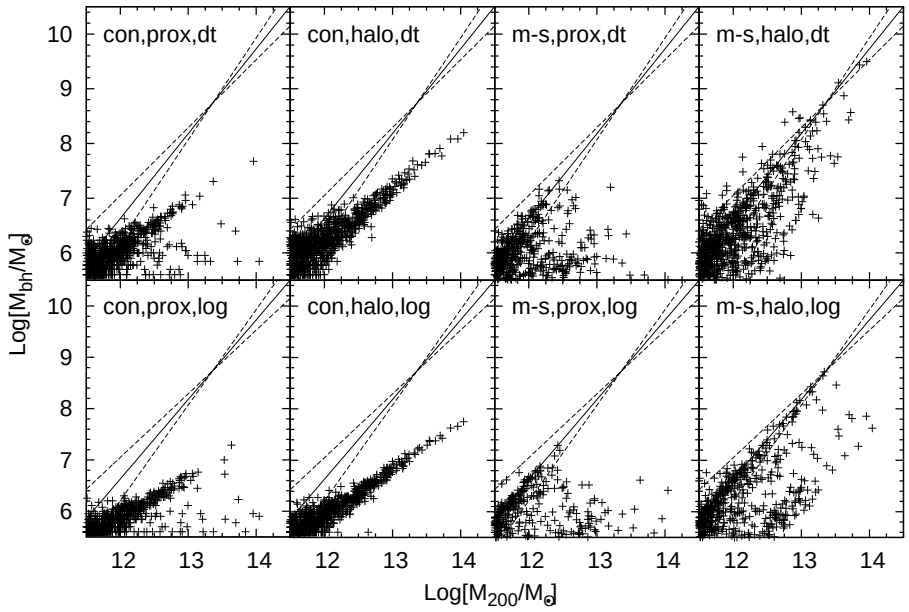

Figure 4.8: Comparison of models (shown as points) against the observed $M_{\rm bh} - M_{\rm tot}$ relation at $z = 0.2$ (solid line). Uncertainties are not shown but are included in later analysis. Dashed lines indicate 1σ uncertainty bounds in the observed relation.

the total merger rate can be very dramatic, as shown in Figure 4.9. The merger rate is defined as

$$\frac{d^2N}{dzdt} \approx \frac{\Delta N}{\Delta z \Delta V} 4\pi c (1+z)^2 d_A^2(z), \tag{4.8}$$

where ΔN is the number of mergers in the redshift interval Δz, ΔV is our simulated volume, $d_A(z)$ is the angular diameter distance, and c is the speed of light. The difference between models is especially significant at low redshift, where "prox" models can reduce the peak merger rate by a factor of two. The difference is negligible at high redshift, since the merger rate here is driven mostly by collisions of smaller halos, and the differences between "prox"- and "halo"-based merging are the smallest. For all cases, our measured merger rate is less than rates found by merger trees (e.g., Micic et al. (2008); Menou et al. (2001)) since those works can include SMBH masses below those which we can resolve.

The frequency of merger checks can have a moderate impact on the slope of the final relations and a significant impact on the maximum black hole mass. However, changing this portion of the model does not significantly alter the scatter for models with constant initial mass. Checking for mergers every time step raises the maximum SMBH mass by roughly half an order of magnitude and allows smaller halos ($< 10^{12}\ M_\odot$) to host black holes fitting the observed relations. We can explain these results by studying the merger rate in Figure 4.9. Here, we see that merger checks at every time step can increase the merger

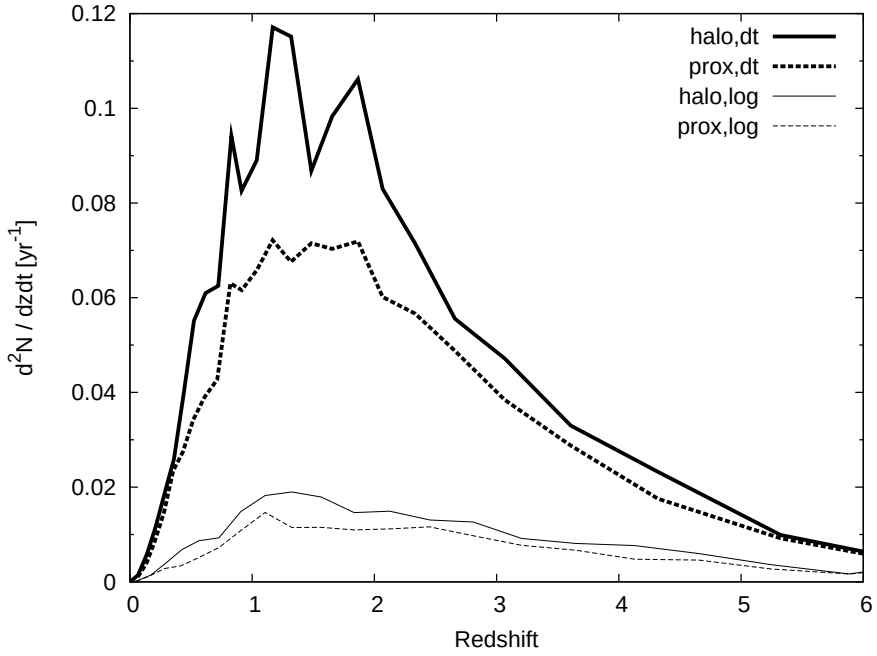

Figure 4.9: Merger rate of all SMBHs in the simulation volume as a function of redshift. We only show models with constant initial mass. Models with instant halo-based merging are shown with solid lines, and models with merging tests are shown with dotted lines. Bold lines describe models with merger checks at every time step; thin lines show models with infrequent checks.

rate by an order of magnitude relative to merger checks evenly spaced in $\log a$. This is largely due to an increased number of seed black holes: by checking at every time step, we may capture halos as soon as they become resolvable, and before they encounter their first merger event. Indeed, we seed roughly twice as many SMBHs in the "dt" models relative to the "log" models, even though they both end up with roughly the same number of black holes at $z = 0$. Also, we capture more mergers at late times: in "log" models, we may skip the formation of small halos and their merging onto an already-formed larger neighbor, missing the SMBH mass associated with the smaller halo. This occurs regardless of seeding method. Spurious re-seeding also contributes somewhat, but this does not dominate because we see the same relative numbers of seeded and final black holes in both the "prox" and "halo" models.

Using an initial seed based on early $M_{\rm bh} - \sigma$ relations produces broad scatter in the final relations. This is especially evident in the "m-s,halo,log" combination, in which there appear to be two distinct populations of SMBHs: one population along the observed relation and another at lower mass. This behavior is due to the fact that halos are seeded in two scenarios: when the halo first becomes resolvable in the simulation, and if the halo merges with another halo, loses its black hole, and later separates. Figure 4.10 illustrates this by showing the initial seed mass as a function of redshift. Note that seed black holes are

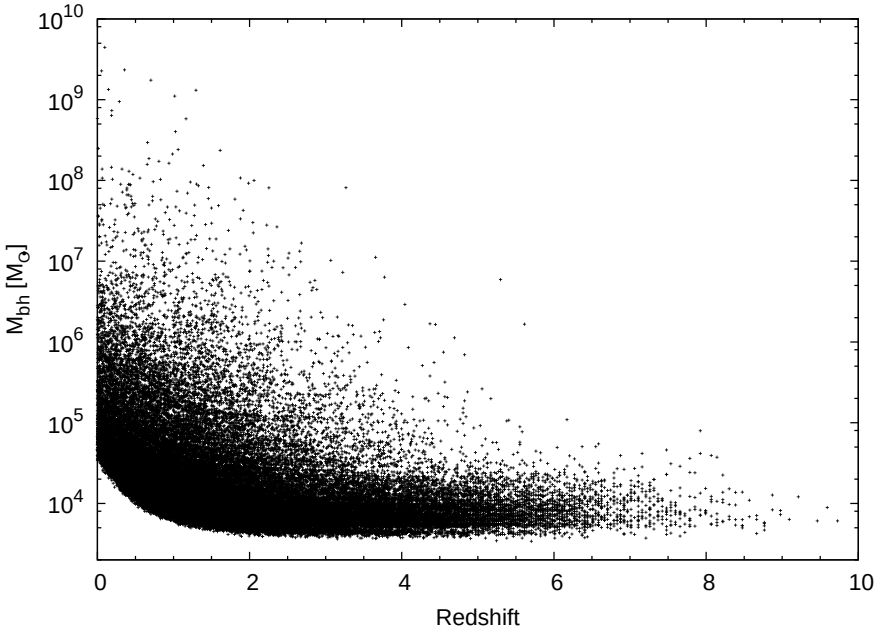

Figure 4.10: Initial SMBH mass for seed black holes as a function of redshift for the "m-s,halo,dt" run.

never larger than $\sim 10^{-5}$ of the host halo mass. Small halos continue to appear throughout the evolution of the simulation and are seeded with $\sim 10^4\ M_\odot$ black holes. However, occasionally a larger halo loses its black hole and must be re-seeded with a correspondingly larger SMBH. Thus we may be left with two populations: halos with their original SMBHs that evolve to relations similar to halos with constant initial mass, and halos that are re-seeded at lower redshifts with black hole masses closer to the observed relation. This distinction is largely eliminated by applying the merger tests at every time step and merging black holes instantly on halo mergers. This results both in higher mass due to increased mergers and in increased low-redshift re-seeding of high-mass halos. This implies that re-seeding selects a few high-mass halos and places them on the observed relation at late times. Indeed, we find that all of the SMBHs with $M_{\rm bh} > 10^9\ M_\odot$ and those black holes that lie at or above the observed relations (roughly half of the population at intermediate masses) are the product of low-redshift re-seeding. However, the majority of black holes evolve without re-seeding at late times, so that the differences between "m-s,dt" and "m-s,log" models at intermediate masses are largely due to the increased merger rate promoting the masses of all black holes. Note that the earlier discovery of halos by checking at every time step does not play a significant role here, since halos discovered later are simply initialized with larger black holes (which was one of the objects of this model).

We may also understand these results by examining the cosmic SMBH mass density, as in Figure 4.11. Note that following Shankar et al. (2004)

Table 4.3: Best-fit Slope and Normalization with 1σ Uncertainty, Compared to Observed $M_{\rm bh} - \sigma$ Relation at $z = 0$ (Eq. 4.6).

Model	Slope	Error	Normalization	Error
con,halo,log	2.2 ± 0.1	-4.4	6.9 ± 0.3	-3.2
con,halo,dt	1.9 ± 0.1	-5.1	7.3 ± 0.4	-2.0
m-s,halo,log	4.6 ± 0.3	0.6	8.0 ± 1.0	-0.2
m-s,halo,dt	4.1 ± 0.2	-0.3	8.1 ± 0.5	-0.1

we only count black holes that are matched to a halo and have masses $10^6 < M_{\rm bh}/\ M_\odot < 5 \times 10^9$ when computing the mass density. All the SMBH densities produced by our models are well below the observed $z = 0$ density of $4.3 \times 10^5\ M_\odot{\rm Mpc}^{-3}$ (Shankar et al. 2004). Despite the fact that the smallest halos in the "m-s" runs started with $10^4\ M_\odot$ seed black holes, re-seeding and merging at low redshift causes the largest black holes to reach $\sim 10^9\ M_\odot$ and the cosmic mass density to reach nearly 1/10 of the observed value.

Even though the re-seeding artificially creates all the SMBHs larger than $10^9\ M_\odot$, and half the black holes above $10^7\ M_\odot$, the majority of black holes are not re-seeded and have masses lower than that of the relation. Thus, even though we can reproduce the m-sigma relation at high masses (albeit with high scatter) there are not enough black holes with sufficient mass to reach the observed cosmic mass density. Similarly, the higher merger rates produced by instant merging models promote more black holes above the minimum mass threshold for inclusion in the density calculation. The frequency of merger checks has a dramatic impact on the $z = 0$ density: here there is up to a factor of five difference between models. This is largely due to the increased rate of discovering early halos in models with constant initial mass, thereby adding more SMBH mass to the simulation at early times. However, the extra mass added when checking "m-s" models at every time step is largely due to increased re-seeding.

We quantify our comparisons by fitting our resulting $M_{\rm bh}-\sigma$ and $M_{\rm bh}-M_{\rm tot}$ relations to a straight line in log space. Since the "prox" models are obviously poor fits to power laws, we will not include them. To mimic observations, we only include black holes with masses greater than $10^6\ M_\odot$. Table 4.3 and Table 4.4 describe the differences between fits to our models and the observed relations. We assume the halo mass uncertainty of Eq. 4.3; however, since it is difficult to quantify all the uncertainties for σ generated in cosmological simulations, we will ignore them in computing fits. While this is an admittedly crude procedure, it does give us some estimate of the ability to distinguish these models from observations and from each other. We define the error in the tables to be the difference between the result of the model in the simulation and the observed quantity divided by the sum of their respective 1σ uncertainties.

We see that, in general, models with constant initial mass are indistinguishable from each other, while these models are, as a group, significantly different from models with varying initial mass. None of the constant-mass models pro-

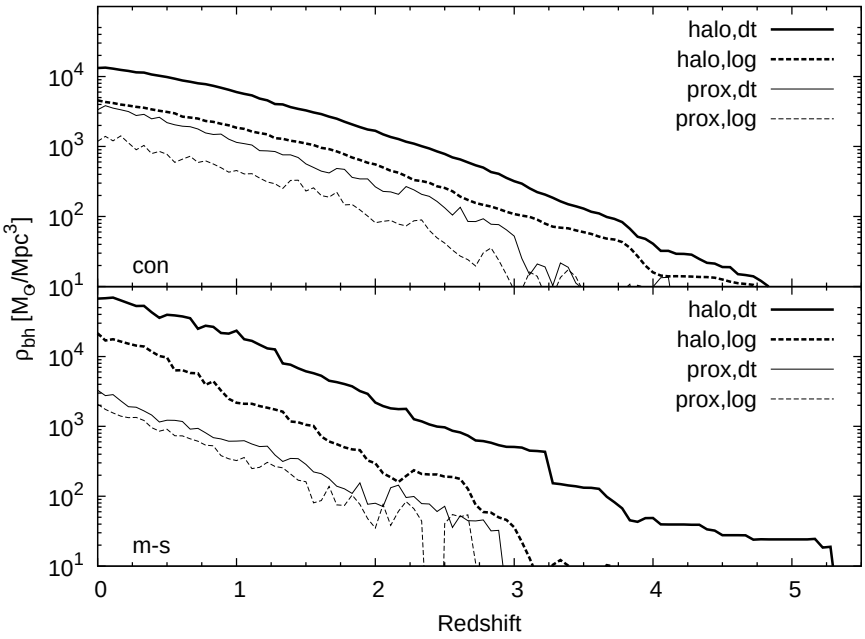

Figure 4.11: Cosmic density of SMBHs with masses $10^6\ M_\odot < M_{\rm bh} < 5 \times 10^9\ M_\odot$ as a function of redshift. The top panel shows all models with constant initial seed mass, while the bottom panel shows models with seed masses based on the $M_{\rm bh} - \sigma$ relation. Models with instant merging are shown with bold lines; those with distance and velocity tests for merging are shown with thin lines. Finally, solid lines describe models with merger checks at every time step, and dashed lines indicate models with checks evenly spaced in $\log a$.

Table 4.4: Best-fit Slope and Normalization with 1σ Uncertainty, Compared to Observed $M_{\rm bh} - M_{\rm tot}$ Relation at $z = 0.2$ (Eq. 4.5).

Model	Slope	Error	Normalization	Error
con,halo,log	0.89 ± 0.01	-2.0	6.8 ± 0.2	-4.9
con,halo,dt	0.87 ± 0.01	-2.1	7.2 ± 0.2	-3.4
m-s,halo,log	2.1 ± 0.2	1.0	7.0 ± 1.0	-1.0
m-s,halo,dt	1.70 ± 0.05	0.4	7.9 ± 0.4	-0.6

duce enough black hole mass to match the observed relations, as seen in the low normalization values, and they do not produce enough high-mass SMBHs in the largest halos, as seen in the low slope.

In contrast, seeding halos with black holes with masses from an early $M_{\rm bh}-\sigma$ relation matches observations well at low redshift. While these models fit the observed relations well, the total mass density of SMBHs is still well below the observed value.

Surprisingly, we see marginally steeper slopes in the "log" models than in the "dt" models. Even though "dt" models have higher merger rates and produce more massive black holes, they also generate a large population of moderate-mass black holes hosted in small halos. This skews the fits to flatter slopes despite the higher maximum black hole mass. However, these differences are not statistically significant, except for the constant initial mass combined with instant merging scenarios, where the low scatter produces small uncertainties.

Generally, the difference between a particular model and the $M_{\rm bh}-\sigma$ relation is matched by the difference between that same model and the $M_{\rm bh} - M_{\rm tot}$ relation. However, the models are more indistinguishable from the $M_{\rm bh} - M_{\rm tot}$ relation, mostly due to the larger uncertainties in the observed relation.

4.5 Conclusion

We have developed a new fast, parallel halo finder for inclusion in cosmological simulations with the simulation code FLASH. Using SO halo finding techniques, we are able to produce halo catalogs in good agreement with traditional post-processing halo finders. Since our halo finder is designed to be fast, we are able to perform halo finding operations at every time step in the simulation, allowing us to perform a detailed analysis of SMBH subgrid models.

While merging alone cannot generate enough total mass in SMBHs to match the observed cosmic mass density or generate high enough maximum black hole mass in the largest halos to match the observed $M_{\rm bh} - \sigma$ and $M_{\rm bh} - M_{\rm tot}$ relations, it can play a large role in developing the slope of the relations, especially at intermediate mass ranges. Thus, merging should not be totally discounted in considering the processes that provide the correlations between black hole mass and bulge, galaxy, and halo properties. However, since none of our considered models can account for the observed cosmic mass density, there is still a significant role for accretion and feedback processes in the evolution of SMBHs. Also, since the choice of models can greatly affect the cosmic SMBH mass density, accretion and feedback models must be chosen carefully to match observations.

The choice of subgrid models can dramatically impact the merging rate of black holes. Since the merger rate has a large influence on the performance of upcoming gravitational wave detectors, halo finding operations in simulations should be done as frequently as possible in order to accurately capture this rate. We do not believe that the inclusion of gas will significantly affect these relative

differences, since they are largely driven by the ability to find more black holes at early times. However, the choice of merging test does not greatly affect the predicted rate, except at low redshift.

While we have bracketed the possible subgrid models with "optimistic" and "pessimistic" scenarios, models best matching insights from theory and observations are usually in between those extremes. While seeding black holes with a uniform initial mass for black holes may well model high-redshift behavior, it is not clear that this is a useful strategy for re-seeding low-redshift halos. Most re-seeding is certainly an artifact of the halo finder and the lack of an in-code merger tree to determine when halos have truly merged. However, there are some plausible scenarios where re-seeding may be needed: for example, when three-body or gas interactions strip an SMBH from a central galaxy. Also, when this approach is coupled with infrequent halo finding operations, it may deposit too little mass in the seed SMBHs. While instant merging is too optimistic, our current lack of understanding of SMBH mergers implies that we cannot entirely specify this portion of the subgrid model, and we must rely on a bracketing procedure.

Future examination of these subgrid models must be done in a cosmological simulation involving gas evolution, accretion onto the black holes, and feedback from active galactic nuclei. However, since models of these processes carry with them their own assumptions and adjustable parameters, care must be taken to fully separate the effects of black hole seeding and merging. It may be possible that due to the self-regulating nature of feedback that the differences among these models may disappear; however, the differences in merger rate and peak black hole mass suggest significant variances may remain. Only once all aspects of these subgrid models are analyzed, understood, and compared to our observational understanding can we confidently combine them into an integrated model.

Chapter 5

Towards a simulation of the origins of magnetic fields in clusters of galaxies

5.1 Introduction

Magnetic fields are apparently ubiquitous in clusters of galaxies, as suggested by observations of diffuse synchrotron emission (Brunetti et al. 2008; Ferrari et al. 2008; Brown et al. 2011; Keshet & Loeb 2010) and Faraday rotation measure (Dreher et al. 1987; Taylor & Perley 1993; Feretti et al. 1999; Carilli & Taylor 2002). These fields are dynamically important in clusters in a variety of ways, such as potentially suppressing thermal conduction (Ruszkowski & Oh 2010; Parrish et al. 2009) and modifying the turbulent properties of the cluster atmosphere (Narayan & Medvedev 2001; Chandran & Maron 2004; Shukurov et al. 2006). They are a necessary component for constraining the systematics of any future cosmological surveys since the fields themselves provide a source of non-thermal pressure support (Dolag & Schindler 2000) and accelerate a non-thermal population of cosmic rays (Miniati et al. 2001; Pfrommer et al. 2007; Brunetti et al. 2007; Skillman et al. 2008). These fields have strength $\sim \mu$G, potentially fill the entire cluster volume, and are tangled with auto-correlation lengths of 1-10 kpc (Carilli & Taylor 2002). However, the origins, evolution, and relationship to other cluster properties of these magnetic fields remain obscure.

These cluster-wide magnetic fields have a variety of potential sources. Exotic processes in the early universe are a natural choice since they can easily magnetize large volumes of the universe prior to the formation of structure (e.g., Baym et al. 1996; Bamba et al. 2008; Battefeld et al. 2008). However, astrophysical mechanisms are typically favored since they do not require exotic physics and are products of well-understood and common processes in typical galaxy and cluster and environments. Specifically, dynamo processes in stellar and active galactic nuclei (AGN) accretion disks can quickly amplify weak seed fields (Rees 1987). These seeds fields, of typical strength $\sim 10^{-18}$ G, can be formed by the Biermann battery mechanism (Widrow 2002), where baroclinic terms in the induction equation at oblique shocks naturally generate fields. However, these dynamo-amplified fields are centrally located in their respective accretion disks

systems and must be expelled into the surrounding medium and eventually into the entire cluster volume, either by AGN jets and bubbles (Daly & Loeb 1990) or galactic winds driven by supernova explosions (Bertone et al. 2006). The fields can then be further stretched and amplified by mergers (Roettiger et al. 1999; Dolag et al. 2002; King & Coles 2005; Dubois & Teyssier 2008; Takizawa 2008) and turbulent dynamos (Ruzmaikin et al. 1989; Subramanian et al. 2006; Xu et al. 2009) in the cluster formation process.

Outflows from AGN are highly favored for injecting magnetic fields into clusters since the outflows are more than energetic enough to account for the total magnetic energy in clusters (Colgate & Li 2000) and are natural carriers of magnetic flux (Daly & Loeb 1990). Indeed, rotation measure observations of jets indicate the presence of magnetic fields in them (Contopoulos et al. 2009). Additionally, the jet-launching mechanism requires the presence of magnetic fields to collimate the jet (Koide et al. 1999).

AGN-based magnetic fields are well-studied in the context of isolated mock clusters, but most studies focus on the evolution of pre-magnetized AGN-blown bubbles (e.g., Robinson et al. 2004; Jones & De Young 2005; Li et al. 2006; Ruszkowski et al. 2007; Gourgouliatos et al. 2010). Sutter et al. (2011b) examined both jet- and bubble-based magnetic field injection, and we will use the results of that survey to inform our simulation. Fewer authors have examined magnetic fields in the context of cosmological structure formation simulations. Donnert et al. (2009) examined the growth of fields via galactic outflows and Xu et al. (2010) followed the evolution of AGN-blown magnetized bubbles. However, these preliminary simulations of AGN outflows did not include accretion and feedback mechanisms; i.e., bubbles were injected into clusters only once at a fixed redshift.

Due to their small size relative to the typical resolution limits of cosmological simulations and their complicated physics, AGN accretion and feedback processes are treated as a subgrid model. Models are highly varied with many levels of sophistication, from various jet models (e.g., Cattaneo & Teyssier 2007; Sternberg et al. 2007; Morsony et al. 2010; Falceta-Gonçalves et al. 2010a; Gaspari et al. 2011) to models of already-inflated bubbles (e.g., Jones & De Young 2005; Sijacki et al. 2007; Gardini 2007; Liu et al. 2008b; Di Matteo et al. 2008; Booth & Schaye 2009). Whatever the model, in a cosmological context it must reproduce observed quantities and correlations, such as the $M_{\rm bh}-\sigma$ relation (Gültekin et al. 2009), the typical size of AGN-blown cavities (Colbert et al. 1996), and the high-redshift activity of quasars (Fan 2006). Furthermore, models of magnetic outflows must reproduce the observed magnetic properties of clusters.

In this paper, we discuss a plan for a full cosmological simulation including magnetized outflows from AGN. We use a fully-closed accretion-feedback loop where the energy available for magnetic injection is derived from an estimated accretion rate. We use the systematic model surveys of Sutter & Ricker (2010), Sutter et al. (2011b), and Yang et al. (2011) to inform our selections of

subgrid models and their associated parameters to ensure a high-quality simulation. In Section 5.2 we discuss our simulation and subgrid models, while in Section 5.3 we outline the expected results of the simulation.

5.2 Numerical approach

5.2.1 Simulation

We are preparing a simulation of cosmological structure formation in a ΛCDM framework within a periodic box spanning 50 h^{-1} comoving Mpc. We assume a Hubble constant $H_0 = 100h$ km s^{-1} Mpc^{-1} with $h = 0.719$, a present-day matter density parameter $\Omega_{m,0} = 0.262$, baryonic density parameter $\Omega_{b,0} = 0.0437$, and spatially flat geometry, as suggested by results from WMAP data (Komatsu et al. 2011). We will use a version of GRAFIC (Bertschinger 2001) modified to accept power spectra generated by CMBFAST (Seljak & Zaldarriaga 1996) to generate our initial conditions for the dark matter particles with an initial redshift of $z_i = 66$. We will normalized the power spectrum using $\sigma_8 = 0.74$. We will included adiabatic gasdynamics for the baryons using a perfect-gas equation of state with adiabatic index $\gamma = 5/3$ and mean particle mass determined from interpolation from collisional ionization equilibrium tables for primordial gas from Sutherland & Dopita (1993). We will initialize the gas temperature at z_i to a constant value of 9100 K, corresponding to a preheating entropy of 250 keV cm^2 at a redshift of 3. We will include radiative cooling using the prescription of Sutherland & Dopita (1993) assuming cosmological iron abundances.

We will use the FLASH code version 3.3 (Fryxell et al. 2000; Dubey et al. 2008), which uses a new direct multigrid Poisson solver (Ricker 2008) to solve for the evolution of the dark matter and an unsplit staggered-mesh MHD solver, which maintains explicit zero magnetic field divergence, to evolve the gas and magnetic fields (Lee 2006). Our simulation will use 1024^3 particles and begin with a uniform 1024^3 mesh. We will use the in-line pSO halo finder (Sutter & Ricker 2010) to identify dark matters halos as the simulation progresses and use the identified halos to trigger refinement, reaching a peak resolution of 6 kpc within the virial radius of all identified halos. There will be approximately $4,000$ resolvable halos within the simulated volume, and by running the code on the Cray XT5 machine at Oak Ridge National Laboratory, we expect the simulation to require approximately $10,000,000$ CPU-hours on $48,000$ cores.

We will output checkpoints files containing all gas and particle data as well as halo catalogs at several redshifts representing important epochs in the evolution of large-scale structure (e.g., 2.0, 1.0, 0.5, 0.25, and 0.0). We will also save AGN and SMBH histories and outflow properties at every timestep for analysis purposes.

Table 5.1: Parameters of the SMBH and AGN magnetic injection models.

Parameter	Description	Value
$M_{\rm bh}$	SMBH seed mass ($M_\odot$)	10^5
$R_{\rm merge}$	SMBH merging radius (zones)	1
$t_{\rm merge}$	SMBH merging time (Myr)	10
$f_{\rm merge}$	Seeding/merging frequency	dt
α	Bondi multiple	1
$\dot{M}_{\rm max}$	Maximum accretion rate	$\dot{M}_{\rm Edd}$
$R_{\rm acc}$	Accretion radius (zones)	4
$R_{\rm dep}$	Minimum depletion radius (zones)	4
$f_{\rm dep}$	Maximum gas depletion fraction	0.1
$r_{\rm inj}$	Maximum feedback extent (kpc)	100
$\Delta_{\rm bh}$	Minimum fraction BH mass increase	0.01%
$\epsilon_{\rm f}$	Feedback efficiency	0.1
$\epsilon_{\rm m}$	Mechanical heating efficiency	0.2
$\chi_{\rm radio}$	Two-mode feedback threshold	$0.1\dot{M}_{\rm Edd}$
$\epsilon_{\rm r}$	QSO heating efficiency	0.05
$R_{\rm radio}$	Feedback radius (zones)	4
r_0	Magnetic radial scale	$1/2r_{\rm inj}$
$\alpha_{\rm B}$	Poloidal/toroidal ratio	$\sqrt{10}$
$E_{\rm B}$	Fraction of total energy in B	1.0

5.2.2 Subgrid models

In Table 5.1 we summarize all the parameters inherent in our models, including the parameters governing SMBH seeding and merging, AGN accretion, feedback structure, and magnetic injection. Our full subgrid prescription combines several models. First, we must model the formation and merging properties of supermassive black holes (SMBHs). We choose a seed mass of 10^5 $M_\odot$, which is motivated by a desire not to violate constraints on the observed black hole mass density (Shankar et al. 2004). We will seed any halo identified in the simulation, and our minimum resolvable halo mass is $\sim 10^{10}$ $M_\odot$. We seed black holes in any resolvable halo by creating a black hole particle in the simulation with a dynamical mass equal to the mass of the black hole and velocity equal to the center-of-mass velocity of the parent halo. To merge two black holes, they must be within the same zone ($R_{\rm merge} = 1$) for at least $t > t_{\rm merge} = 10$ Myr (Dotti et al. 2007). To help avoid spurious mergers, we did not include satellite halos (halos that intersect a larger neighbor) in the halo catalog used by the seeding and merging models. When we merge black holes, we remove the smaller of the pair and add its mass to the larger of the pair. The larger SMBH maintains its position and velocity. We do not re-center black holes on halo potential minima. Finally, we will perform the seeding and merging test at every timestep during the simulation ($f_{\rm merge} = dt$).

We will estimate the accretion rate onto each black hole using a "boosted"

Bondi-Hoyle-Lyttleton (Bondi 1952) accretion rate:

$$\dot{M}_{\rm Bondi} = \alpha \; 4\pi G^2 M_{\rm bh}^2 \frac{\rho}{{c_{\rm s}}^3}, \tag{5.1}$$

where the sound speed $c_{\rm s}$ and the density ρ are measured on the simulation mesh, and $M_{\rm bh}$ is the black hole mass. The Bondi rate well approximated the observed accretion rate measured at parsec scales (Allen et al. 2006). However, simulations of clusters and larger structures cannot obtain sufficient resolution to reach these parsec scales, so most authors include some compensating factor, so they typically set $\alpha = 100$-300. However, our analysis in Sutter et al. (2011b) suggests that this value generates unreasonably large and frequent bubbles, so we will set $\alpha = 1$. We measure the accretion rate within a radius $R_{\rm acc} = 4$ zones, and deplete the accreted gas from the same region, unless the fraction of the gas to be removed in a cell exceeds $f_{\rm dep} = 0.1$, in which case we enlarge the depletion radius $R_{\rm dep}$ to lower the depleted gas fraction below this value. We impose an upper limit on the accretion rate corresponding to the Eddington rate,

$$\dot{M}_{\rm Edd} = \frac{4\pi G M_{\rm bh} m_{\rm p}}{\epsilon_{\rm f} \sigma_{\rm T} c}, \tag{5.2}$$

where $m_{\rm p}$ is the mass of the proton, $\sigma_{\rm T}$ is the Thompson cross-section, and $\epsilon_{\rm f}$ is the radiative efficiency.

Our feedback will take the form of a fully magnetized bubble centered on the black hole. The energy available for feedback is computed as

$$\dot{E} = \epsilon_{\rm m} \epsilon_{\rm f} c^2 \Delta M_{\rm bh}, \tag{5.3}$$

where $\Delta M_{\rm bh}$ is the increase in BH mass since the last bubble event, $\epsilon_{\rm f}$ is the feedback efficiency and and $\epsilon_{\rm m}$ is the mechanical heating efficiency. We will only form bubbles when the black hole has increased its mass since the previous bubble formation by $\Delta M_{\rm bh}/M_{\rm bh} > 0.01\%$. We distribute our magnetic fields within a sphere with radius $r_{\rm inj} = 40$ kpc fixed on the SMBH. The injected magnetic field has a structure (Li et al. 2006)

$$B_r(r', z') = 2B_0 z' r' \exp\left(-{r'}^2 - {z'}^2\right) \tag{5.4}$$

$$B_z(r', z') = 2B_0 \left(1 - {r'}^2\right) \exp\left(-{r'}^2 - {z'}^2\right) \tag{5.5}$$

$$B_\phi(r', z') = B_0 \alpha_{\rm B} r' \exp\left(-{r'}^2 - {z'}^2\right), \tag{5.6}$$

where $r' = \sqrt{x^2 + y^2}/r_0$ and $z' = z/r_0$. Here, we set the scale radius r_0 to be $0.5 r_{\rm inj}$ so that the entire injected magnetic structure fits inside the given feedback region. $\alpha_{\rm B}$ is the ratio of poloidal to toroidal flux, which we choose to be $\alpha_{\rm B} = \sqrt{10}$ for an initially relaxed field, as suggested by Li et al. (2006). Each SMBH is given a random jet orientation, which provides an axis for the injected magnetic field. Our analyses in Sutter et al. (2011a) and Yang et al. (2011)

revealed that these fixed bubbles produced cluster hydrodynamic properties that were consistent with observations and magnetic field structures that most resembled those of actual clusters.

Episodic bubble-based models can occasionally allow the accretion rate to reach large fractions of the Eddington rate. Indeed, observations indicate that the SMBH accretion rate is very high, at least at high redshift (Fan 2006). When the accretion rate, and hence the available feedback energy, reaches large values the feedback takes the form of pure radiation (Fender et al. 1999; Gallo et al. 2003). In this case, instead of mechanically inflating bubbles, the outflows from the AGN simply heat the nearby gas:

$$\dot{E} = \epsilon_{\rm f}\epsilon_{\rm r}c^2\dot{M}, \tag{5.7}$$

where $\epsilon_{\rm f}$ is the feedback efficiency and $\epsilon_{\rm r}$ is the QSO heating efficiency. We must choose a threshold to switch to this feedback mode, and we follow Sijacki et al. (2007) with a value of $\chi_{\rm radio} = 0.01\dot{M}_{\rm Edd}$. We are free here to choose our radius for depositing the energy, and for numerical stability we choose a feedback radius of 4 zones.

5.3 Future work

We have the machinery capable of running and analyzing the simulation described above. We will evaluate the ability of this magnetized feedback model to generate observed relations between black hole mass and bulge velocity dispersion (Gültekin et al. 2009) and halo mass (Bandara et al. 2009). We will investigate the initial redshift of significant magnetic field growth in clusters and follow the injection history and its relation to SMBH growth and merger activity. We will correlate the strength of the resulting magnetic fields with cluster properties such as mass and X-ray luminosity. We will produce synthetic rotation measure maps of the clusters to probe their observational topology. We will generate mock radio sky maps using the procedures outlined in (Sutter et al. 2011a). All the gathered statistics will help us to understand the role that AGN play in generating magnetic fields through cosmic time.

Chapter 6

Conclusions

The growth and evolution of magnetic fields in clusters of galaxies is an incredibly rich, deep, intricate, and difficult problem. Due to their complex nature, we can only understand their origins and evolution using large-scale cosmological simulations. Using the first set of radio halo statistics derived entirely from large-scale cosmological simulation, we have demonstrated that small changes in the magnetic field strength and correlation with cluster mass can dramatically affect many key observables, in this case the expected number counts of radio halos. This work has clearly demonstrated that a more detailed understanding of cluster magnetic fields is necessary in order to understand and predict future low-frequency radio observations.

However, the physical processes associated with the most promising candidate for generating large-scale magnetic fields in clusters, i.e. by ejecting them from AGN accretion disks systems where dynamo actions amplify them from weak seed fields, are difficult to capture in large-scale simulation, due to the small scales and rich physics involved. On the opposite scale, we must perform large simulations in order to capture many halos for a proper statistical analysis, and these clusters must be at high enough resolution to capture the complex nature of the magnetic fields in the intracluster medium. These necessities combined mean that in order to study the origins and evolution of magnetic fields we must include AGN-based magnetic feedback as a subgrid model. We must model not only the accretion and feedback properties of AGN, but also the seeding and merging characteristics of SMBHs.

We have conducted a systematic study of the growth and evolution of magnetic fields due to the self-regulated feedback of a central active galactic nuclei within an isolated mock cluster. We have implemented magnetic field injection using a representative model of continuous small-scale jets and sporadic large-scale bubbles. We found that in general, strong magnetic fields placed near the central black hole are very effective at pushing gas away from the core and preventing cooled gas from accreting. However, all models quickly permeate the entire cluster with weak fields and produce strong fields in the central core.

The jets and fixed bubbles maintain regular torus-like shapes in the magnetic field that persist over several billion years with strong fields concentrated in the core, although the fixed bubbles eventually disperse. We found the jet models to be relatively insensitive to many changes in the underlying model, while the bubble models were much more sensitive.

While the jets appears to be more robust, they have significant difficulties in quickly and efficiently magnetizing the cluster. They must require some additional mechanisms operating in the intracluster medium to spread and tangle the injected fields. On the other hand, the randomly-placed bubbles, which automatically generate rich, tangled magnetic field morphologies, are more sensitive to subgrid model choices. Since the fixed bubbles have a predetermined radius, they do not face this problem. While they also produce somewhat ordered fields, they spread these fields out to larger volumes, which makes these fields more susceptible to tangling from cluster mergers galaxy motions. They can also strongly magnetize the cluster very quickly - in less than 1 Gyr.

To investigate various aspects of supermassive black hole subgrid models, we have developed a new fast, parallel halo finder for inclusion in cosmological simulations with the simulation code FLASH. Since our halo finder is designed to be fast, we are able to perform halo finding operations at every time step in the simulation, allowing us to perform a detailed analysis of SMBH subgrid models. We found that the choice of subgrid models can dramatically impact the merging rate of black holes. While seeding black holes with a uniform initial mass for black holes may well model high-redshift behavior, it is not clear that this is a useful strategy for re-seeding low-redshift halos. Most re-seeding is certainly an artifact of the halo finder and the lack of an in-code merger tree to determine when halos have truly merged. However, there are some plausible scenarios where re-seeding may be needed: for example, when three-body or gas interactions strip an SMBH from a central galaxy. While instant merging is too optimistic, our current lack of understanding of SMBH mergers implies that we cannot entirely specify this portion of the subgrid model, and we must rely on a bracketing procedure.

Once all aspects of these subgrid models are analyzed, understood, and compared to our observational understanding can we confidently combine them into an integrated model. Using the above subgrid survey and analysis, we can confidently recommend a set of parameters to use for performing a large-scale cosmological simulation. This simulation will produce copious amounts of data, including relations between black hole mass and bulge velocity dispersion, the initial redshift of significant magnetic field growth in clusters, the injection history and its relation to SMBH growth and merger activity, correlations between the strength of the resulting magnetic fields and cluster properties such as mass and X-ray luminosity, synthetic rotation measure maps of the clusters to probe their observational topology, and mock radio sky maps. Only with such a large, detailed, and systematic study can we understand the role that active galactic

nuclei play in generating magnetic fields in clusters of galaxies.

Appendix A

Performance and parallel scalability of the pSO halo finder

In order to minimize communication among processors, we divide potential halos into two lists. For every potential halo, we compute the overdensity at the largest possible on-processor radius. If the next search radius is larger than this, the halo is added to a list that must be communicated. Thus, all on-processor halos are processed concurrently with no communication. Since the volume of communication is very small, we send all other halos to every processor. However, since this approach is not scalable to very large halo catalogs or numbers of processors, we switch to a buffered communication pattern if we cannot allocate a global halo catalog. In the buffered approach, halo lists are only communicated to the nearest processors one at a time. The list is communicated until all blocks within the volume of the processor's halos have been searched. While slower than the all-to-all approach, the amount of storage per processor required stays fixed as the number of processors and number of halos grow. In either case, communication continues until all halos are fully searched. For this study, we will use the all-to-all approach.

Figure A.1(a) shows the strong scaling of the pSO halo finder as a fraction of the total wall clock time in a single FLASH time step. We show three different uniform problem sizes: 256^3, 512^3, and 1024^3 particles and zones. We restarted each simulation at a representative redshift, $z = 0.25$, and ran for five time steps. These times do not include optional portions of the halo finder routine, such as writing the halo catalog to disk or tagging particles within halos. We performed these calculations on jaguar, a Cray XT5 system at Oak Ridge National Laboratory. Jaguar consists of 16,688 dual six-core AMD Opteron nodes with 16 GB of memory per node and has a peak performance of 2.332 petaflops. Our approach offers good strong scaling behavior: we are able to beat or match the scaling performance of FLASH at all problem sizes. At larger core counts, FLASH has difficulty scaling the Poisson solver, whereas the halo finder maintains good scalability. However, we can infer that we have poor weak scaling: the halo finding steps require ever larger wall clock time as the problem size grows.

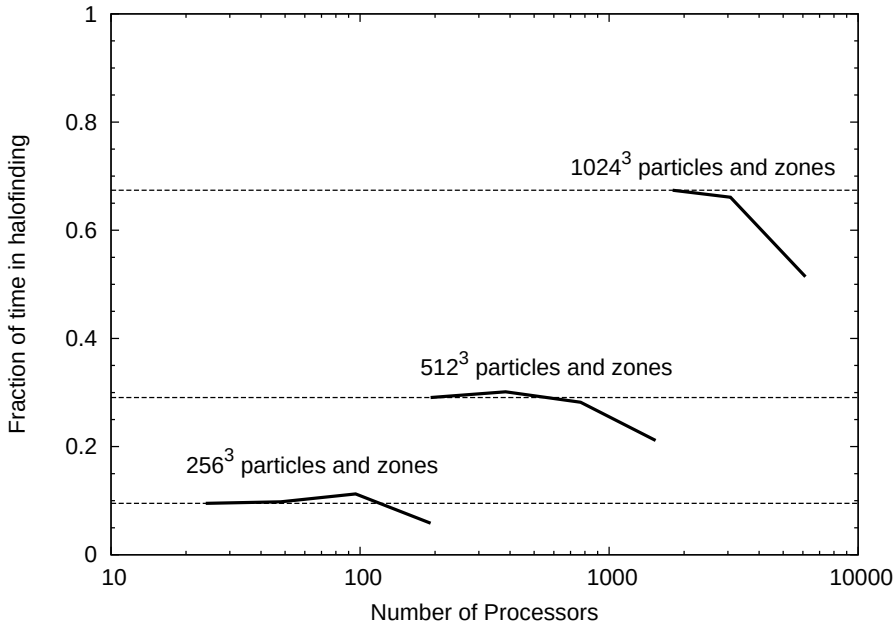

(a) Strong scaling of pSO halo finder at various problem sizes as a fraction of total wall clock time in a single FLASH time step.

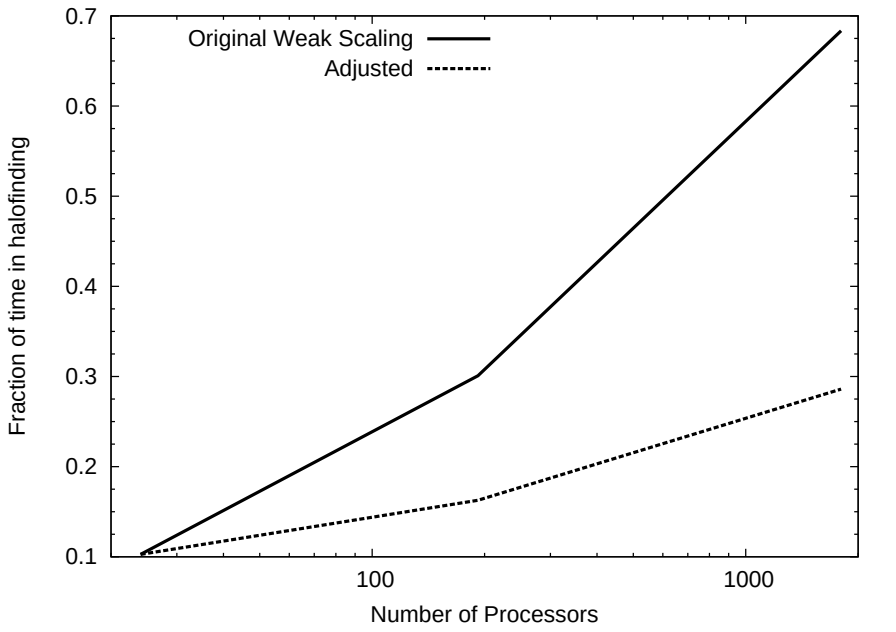

(b) Weak scaling at smallest number of processors for each problem size as a fraction of total wall clock time in a single FLASH time step. The dotted line indicates weak scaling after adjustments have been made to account for non-linear scaling of halo counts with problem size.

Figure A.1: Strong and weak scaling of the pSO halo finder.

The poor weak scaling is due to several factors. First, since these are uniform grid calculations, at low redshift the particle distribution among processors becomes highly unbalanced. FLASH is block based and uses a Morton curve the distribute these blocks among the processors. Thus, while each processor has roughly the same number of blocks, those blocks in highly dense regions will contain many more particles than those in voids. Since our halo finder scans through particles, there is a lack of concurrency due to this imbalance. At small problem sizes, this is not an issue, but with 1024^3 particles all processors must wait for the few heavily loaded processors to complete searching. There is an imbalance in halos as well, since highly overdense regions contain more halos than underdense regions. Note that this is a bigger problem for box sizes smaller than 200 Mpc. We found that the 256^3 run placed a maximum of 15 halos on a single processor, the 512^3 run had up to 33 halos on a single processor, and the 1024^3 run mapped up to 80 halos on a single processor. Figure A.1(b) shows the effects of the imbalanced load due to an increased maximum number of halos on the weak scaling behavior. We compute the effects by maintaining no more than 15 halos per processor no matter the problem size. We performed this test by ignoring halos past this limit. We see that halo imbalance explains a significant part of the weak scaling results.

Second, as we increase the resolution, we greatly increase the number of resolvable halos. Since smaller halos are much more numerous than larger ones (see Figure 4.5), for every doubling of the resolution we get roughly ten times the number of halos. However, the number of particles and zones only increases by a factor of eight. This means that even if we devote eight times the number of processors to the problem, we will spend a larger fraction of a time step finding all the halos.

Finally, as we increase the resolution, we require more steps in the binary search procedure to meet the stopping criterion. At 256^3 zones, we require roughly 35 steps to identify the halos. At 512^3 zones, we require 45 steps on average. Finally, for 1024^3 zones, we average 55 steps. This increases the serial runtime of the halo finder, regardless of the degree of concurrency.

These calculations were performed with only dark matter. As we perform runs with more included physics, such as hydrodynamics and radiative cooling, the fraction of time spent in halo finding will decrease, even for high-resolution runs. Also, we expect AMR runs to alleviate the problems of poor particle load balancing, since in cosmological simulations we typically refine on overdense regions. We are currently preparing a manuscript detailing the performance of the halo finder with different box sizes, combinations of resolutions of particles and zones, additional physics, and different AMR refinement schemes.

References

Abdo, A. A. & Collaboration. 2010, The Astrophysical Journal, 715, 429

Ackermann, M., Ajello, M., Allafort, A., Baldini, L., Ballet, J., Barbiellini, G., Bastieri, D., Bechtol, K., Bellazzini, R., Blandford, R. D., Blasi, P., Bloom, E. D., Bonamente, E., Borgland, A. W., Bouvier, A., Brandt, T. J., Bregeon, J., Brigida, M., Bruel, P., Buehler, R., Buson, S., Caliandro, G. A., Cameron, R. A., Caraveo, P. A., Carrigan, S., Casandjian, J. M., Cavazzuti, E., Cecchi, C., Çelik, O., Charles, E., Chekhtman, A., Cheung, C. C., Chiang, J., Ciprini, S., Claus, R., Cohen-Tanugi, J., Colafrancesco, S., Cominsky, L. R., Conrad, J., Dermer, C. D., de Palma, F., do Couto e Silva, E., Drell, P. S., Dubois, R., Dumora, D., Edmonds, Y., Farnier, C., Favuzzi, C., Frailis, M., Fukazawa, Y., Funk, S., Fusco, P., Gargano, F., Gasparrini, D., Gehrels, N., Germani, S., Giglietto, N., Giordano, F., Giroletti, M., Glanzman, T., Godfrey, G., Grenier, I. A., Grondin, M.-H., Guiriec, S., Hadasch, D., Harding, A. K., Hayashida, M., Hays, E., Horan, D., Hughes, R. E., Jeltema, T. E., Jóhannesson, G., Johnson, A. S., Johnson, T. J., Johnson, W. N., Kamae, T., Katagiri, H., Kataoka, J., Kerr, M., Knödlseder, J., Kuss, M., Lande, J., Latronico, L., Lee, S.-H., Lemoine-Goumard, M., Longo, F., Loparco, F., Lott, B., Lovellette, M. N., Lubrano, P., Madejski, G. M., Makeev, A., Mazziotta, M. N., Michelson, P. F., Mitthumsiri, W., Mizuno, T., Moiseev, A. A., Monte, C., Monzani, M. E., Morselli, A., Moskalenko, I. V., Murgia, S., Naumann-Godo, M., Nolan, P. L., Norris, J. P., Nuss, E., Ohsugi, T., Omodei, N., Orlando, E., Ormes, J. F., Ozaki, M., Paneque, D., Panetta, J. H., Pepe, M., Pesce-Rollins, M., Petrosian, V., Pfrommer, C., Piron, F., Porter, T. A., Profumo, S., Rainò, S., Rando, R., Razzano, M., Reimer, A., Reimer, O., Reposeur, T., Ripken, J., Ritz, S., Rodriguez, A. Y., Romani, R. W., Roth, M., Sadrozinski, H. F.-W., Sander, A., Parkinson, P. M. S., Scargle, J. D., Sgrò, C., Siskind, E. J., Smith, P. D., Spandre, G., Spinelli, P., Starck, J.-L., Stawarz, ., Strickman, M. S., Strong, A. W., Suson, D. J., Tajima, H., Takahashi, H., Takahashi, T., Tanaka, T., Thayer, J. B., Thayer, J. G., Tibaldo, L., Tibolla, O., Torres, D. F., Tosti, G., Tramacere, A., Uchiyama, Y., Usher, T. L., Vandenbroucke, J., Vasileiou, V., Vilchez, N., Vitale, V., Waite, A. P., Wang, P., Winer, B. L., Wood, K. S., Yang, Z., Ylinen, T., & Ziegler, M. 2010, The Astrophysical Journal, 717, L71

Adams, J. 1996, Physics Letters B, 388, 253

Agertz, O., Moore, B., Stadel, J., Potter, D., Miniati, F., Read, J., Mayer, L., Gawryszczak, A., Kravtsov, A., Nordlund, A. k., Pearce, F., Quilis, V., Rudd,

D., Springel, V., Stone, J., Tasker, E., Teyssier, R., Wadsley, J., & Walder, R. 2007, Monthly Notices of the Royal Astronomical Society, 380, 963

Albrecht, A., Bernstein, G., Cahn, R., Freedman, W. L., Hewitt, J., Hu, W., Huth, J., Kamionkowski, M., Kolb, E. W., Knox, L., Mather, J. C., Staggs, S., & Suntzeff, N. B. 2006

Albrecht, A., Steinhardt, P., Turner, M., & Wilczek, F. 1982, Physical Review Letters, 48, 1437

Allen, S. W., Dunn, R. J. H., Fabian, A. C., Taylor, G. B., & Reynolds, C. S. 2006, Monthly Notices of the Royal Astronomical Society, 372, 21

Amaro-Seoane, P., Gair, J. R., Freitag, M., Miller, M. C., Mandel, I., Cutler, C. J., & Babak, S. 2007, Class. Quantum Grav., 24, 113

Anninos, P., Norman, M. L., & Clarke, D. A. 1994, The Astrophysical Journal, 436, 11

Annis, J., Castander, F. J., Evrard, A. E., Frieman, J. A., Gaztanaga, E., Jain, B., Kravtsov, A. V., Lahav, O., Lin, H., Mohr, J., Ricker, P. M., Stebbins, A., Wechsler, R. H., Weinberg, D. H., & Weller, J. 2005, 5

Arnaud, K. A. 1996, Astronomical Data Analysis Software and Systems V, 101

Athreya, R. M., Kapahi, V. K., McCarthy, P. J., & van Breugel, W. 1998, Astronomy and Astrophysics

Bacchi, M., Feretti, L., Giovannini, G., & Govoni, F. 2003, Astronomy and Astrophysics, 400, 465

Baes, M., Buyle, P., Hau, G. K. T., & Dejonghe, H. 2003, astro-ph/0303628

Bahcall, N. A. 1977, Annual Review of Astronomy and Astrophysics, 15, 505

Baker, J. G., Boggs, W. D., Centrella, J., Kelly, B. J., McWilliams, S. T., Miller, M. C., & van Meter, J. R. 2008, Astrophys. J., 682, L29

Bamba, K., Ohta, N., & Tsujikawa, S. 2008, Physical Review D, 78

Bandara, K., Crampton, D., & Simard, L. 2009, Astrophys. J., 704, 1135

Barnes, J. E. & Hut, P. 1989, The Astrophysical Journal Supplement Series, 70, 389

Barrow, J., Ferreira, P., & Silk, J. 1997, Physical Review Letters, 78, 3610

Bartelmann, M. 2003, Matter and Energy in Clusters of Galaxies, 301

Bartelmann, M. & Schneider, P. 2001, Physics Reports, 340, 291

Battaglia, N., Bond, J. R., Pfrommer, C., Sievers, J. L., & Sijacki, D. 2010, The Astrophysical Journal, 725, 91

Battefeld, D., Battefeld, T., Wesley, D. H., & Wyman, M. 2008, Journal of Cosmology and Astroparticle Physics, 2008, 001

Baugh, C. M. 2006, Reports on Progress in Physics, 69, 3101

Baym, G., Bödeker, D., & McLerran, L. 1996, Physical Review D, 53, 662

Beck, R. 2009, To be published in SKADS Conference 2009 "Widefield Science and Technology for the SKA", eds. S.A. Torchinsky, A. van Ardenne, T. van den Brink-Havinga, A. van Es, A.J. Faulkner;

Begelman, M. C., Volonteri, M., & Rees, M. J. 2006, Mon. Not. R. Astro. Soc., 370, 289

Berczik, P., Merritt, D., Spurzem, R., & Bischof, H. P. 2006, Astrophys. J., 642, L21

Berger, M. & Colella, P. 1989, Journal of Computational Physics, 82, 64

Berger, M. & Oliger, J. 1984, Journal of Computational Physics, 53, 484

Bertone, S., Vogt, C., & Ensslin, T. 2006, Monthly Notices of the Royal Astronomical Society

Bertschinger, E. 1998, Annual Review of Astronomy and Astrophysics, 36, 599

—. 2001, Astrophys. J. Suppl., 137, 1

Bhattacharya, S., Heitmann, K., White, M., Lukić, Z., Wagner, C., & Habib, S. 2010, arXiv e-prints

Bialek, J. J., Evrard, A. E., & Mohr, J. J. 2001, The Astrophysical Journal, 555, 597

Biermann, L. 1950, Zeitschrift Naturforschung Teil A, 5

Blasi, P. 1999, Astroparticle Physics, 12, 169

Blasi, P., Burles, S., & Olinto, A. V. 1999, The Astrophysical Journal, 514, L79

Bogdanović, T., Reynolds, C. S., Balbus, S. A., & Parrish, I. J. 2009, The Astrophysical Journal, 704, 211

Bogdanovic, T., Reynolds, C. S., & Miller, M. C. 2007, Astrophys. J. Lett., 661, L147

Bohringer, H., Matsushita, K., Churazov, E., Ikebe, Y., & Chen, Y. 2002, Astronomy and Astrophysics, 382, 804

Bohringer, H., Schuecker, P., Guzzo, L., Collins, C. A., Voges, W., Cruddace, R. G., Ortiz-Gil, A., Chincarini, G., De Grandi, S., Edge, A. C., MacGillivray, H. T., Neumann, D. M., Schindler, S., & Shaver, P. 2004, Astronomy and Astrophysics, 425, 367

Bonafede, A., Govoni, F., Feretti, L., Murgia, M., Giovannini, G., & Brueggen, M. 2011

Bondi, H. 1952, Monthly Notices of the Royal Astronomical Society, 112

Booth, C. M. & Schaye, J. 2009, Mon. Not. R. Astro. Soc., 398, 53

Brackbill, J. & Barnes, D. 1980, Journal of Computational Physics, 35, 426

Bregman, J. N. & David, L. P. 1988, The Astrophysical Journal, 326, 639

Brown, S., Duesterhoeft, J., & Rudnick, L. 2011, The Astrophysical Journal, 727, L25

Brüggen, M., Ruszkowski, M., Simionescu, A., Hoeft, M., & Dalla Vecchia, C. 2005, The Astrophysical Journal, 631, L21

Brüggen, M. & Scannapieco, E. 2009, Mon. Not. R. Astro. Soc., 398, 548

Brunetti, G. 2009, Magnetic Fields in the Universe II: From Laboratory and Stars to the Primordial Universe (Eds. A. Esquivel, 36, 201

Brunetti, G., Cassano, R., Dolag, K., & Setti, G. 2009, Astronomy and Astrophysics, 507, 661

Brunetti, G., Giacintucci, S., Cassano, R., Lane, W., Dallacasa, D., Venturi, T., Kassim, N. E., Setti, G., Cotton, W. D., & Markevitch, M. 2008, Nature, 455, 944

Brunetti, G. & Lazarian, A. 2011, Monthly Notices of the Royal Astronomical Society, 410, 127

Brunetti, G., Venturi, T., Dallacasa, D., Cassano, R., Dolag, K., Giacintucci, S., & Setti, G. 2007, The Astrophysical Journal, 670, L5

Buote, D. A. 2001, The Astrophysical Journal, 553, L15

Carilli, C. L. & Taylor, G. B. 2002, Annual Review of Astronomy and Astrophysics, 40, 319

Cassano, R. 2010, Astronomy and Astrophysics, 517, A10

Cassano, R. & Brunetti, G. 2005, Monthly Notices of the Royal Astronomical Society, 357, 1313

Cassano, R., Brunetti, G., Röttgering, H. J. A., & Brüggen, M. 2009, Astronomy and Astrophysics, 509, A68

Cassano, R., Brunetti, G., & Setti, G. 2006, astro-ph/0604103

Cassano, R., Brunetti, G., Setti, G., Govoni, F., & Dolag, K. 2007, Monthly Notices of the Royal Astronomical Society, 378, 1565

Cassano, R., Brunetti, G., Venturi, T., Setti, G., Dallacasa, D., Giacintucci, S., & Bardelli, S. 2008, Astronomy and Astrophysics, 480, 687

Cattaneo, A. & Teyssier, R. 2007, Monthly Notices of the Royal Astronomical Society, 376, 1547

Chandran, B. D. G. & Maron, J. L. 2004, The Astrophysical Journal, 602, 170

Ciotti, L. & Ostriker, J. P. 2007, The Astrophysical Journal, 665, 1038

Clarke, T. E. 2004, To appear in a dedicated issue of the Journal of the Korean Astronomical Society (JKAS). Proceedings of the "International conference on Cosmic Rays and Magnetic Fields in Large Scale Structure", 6

—. 2005, From Clark Lake to the Long Wavelength Array: Bill Erickson's Radio Science ASP Conference Series, 345

Clarke, T. E., Kronberg, P. P., & Böhringer, H. 2001, The Astrophysical Journal, 547, L111

Cohen, A. S., Lane, W. M., Cotton, W. D., Kassim, N. E., Lazio, T. J. W., Perley, R. A., Condon, J. J., & Erickson, W. C. 2007, The Astronomical Journal, 134, 1245

Colbert, E. J. M., Baum, S. A., Gallimore, J. F., O'Dea, C. P., & Christensen, J. A. 1996, The Astrophysical Journal, 467, 551

Colella, P. & Woodward, P. 1984, Journal of Computational Physics, 54, 174

Colgate, S. A. & Li, H. 2000, Highly Energetic Physical Processes and Mechanisms for Emission from Astrophysical Plasmas

Collins, C. A., Stott, J. P., Hilton, M., Kay, S. T., Stanford, S. A., Davidson, M., Hosmer, M., Hoyle, B., Liddle, A., Lloyd-Davies, E., Mann, R. G., Mehrtens, N., Miller, C. J., Nichol, R. C., Romer, A. K., Sahlén, M., Viana, P. T. P., & West, M. J. 2009, Nature, 458, 603

Collins, D. C., Xu, H., Norman, M. L., Li, H., & Li, S. 2010, The Astrophysical Journal Supplement Series, 186, 308

Contopoulos, I., Christodoulou, D. M., Kazanas, D., & Gabuzda, D. C. 2009, The Astrophysical Journal, 702, L148

Couchman, H. M. P. 1991, The Astrophysical Journal, 368, L23

Croton, D. J. 2009, Mon. Not. R. Astro. Soc., 394, 1109

Dahle, H., Hannestad, S., & Sommer-Larsen, J. 2003, The Astrophysical Journal, 588, L73

Daly, R. A. & Loeb, A. 1990, The Astrophysical Journal, 364, 451

David, L. P., Nulsen, P. E. J., McNamara, B. R., Forman, W., Jones, C., Ponman, T., Robertson, B., & Wise, M. 2001, The Astrophysical Journal, 557, 546

Deiss, B. M., Reich, W., Lesch, H., & Wielebinski, R. 1997, Astronomy and Astrophysics

Dennison, B. 1980, The Astrophysical Journal, 239, L93

Di Matteo, T., Colberg, J., Springel, V., Hernquist, L., & Sijacki, D. 2008, Astrophys. J., 676, 33

Díaz-Gil, A., García-Bellido, J., Pérez, M. G., & González-Arroyo, A. 2008, Journal of High Energy Physics, 2008, 043

Diemand, J., Zemp, M., Moore, B., Stadel, J., & Carollo, M. 2005, Monthly Notices of the Royal Astronomical Society, 364, 051025032210001

Dolag, K., Bartelmann, M., & Lesch, H. 2002, Astronomy and Astrophysics, 387, 383

Dolag, K., Meneghetti, M., Moscardini, L., Rasia, E., & Bonaldi, A. 2006, Monthly Notices of the Royal Astronomical Society, 370, 060608030310010

Dolag, K. & Schindler, S. 2000, Astronomy and Astrophysics

Dolag, K. & Stasyszyn, F. A. 2008, Mon. Not. R. Astro. Soc., 398, 1678

Dolag,K. & Schindler,S. 2000, Astronomy and Astrophysics

Donnert, J., Dolag, K., Brunetti, G., Cassano, R., & Bonafede, A. 2010a, Monthly Notices of the Royal Astronomical Society, 401, 47

Donnert, J., Dolag, K., Cassano, R., & Brunetti, G. 2010b, Monthly Notices of the Royal Astronomical Society, 407, 1565

Donnert, J., Dolag, K., Lesch, H., & Müller, E. 2009, Monthly Notices of the Royal Astronomical Society, 392, 1008

Dotti, M., Colpi, M., Haardt, F., & Mayer, L. 2007, Mon. Not. R. Astro. Soc., 379, 956

Dougherty, S. M. & Perley, R. 2011, Bulletin de la Societe Royale des Sciences de Liege, 80, 491

Dreher, J. W., Carilli, C. L., & Perley, R. A. 1987, The Astrophysical Journal, 316, 611

Dubey, A., Reid, L. B., & Fisher, R. 2008, Physica Scripta, T132, 014046

Dubois, Y., Devriendt, J., Slyz, A., & Teyssier, R. 2010, Monthly Notices of the Royal Astronomical Society, 409, 985

Dubois, Y. & Teyssier, R. 2008, Astronomy and Astrophysics, 482, 13

Dunn, R. J. H. & Fabian, A. C. 2006, Monthly Notices of the Royal Astronomical Society, 373, 959

Efstathiou, G., Davis, M., White, S. D. M., & Frenk, C. S. 1985, The Astrophysical Journal Supplement Series, 57, 241

Enß lin, T., Pfrommer, C., Miniati, F., & Subramanian, K. 2011, Astronomy & Astrophysics, 527, A99

Enß lin, T. A., Biermann, P., Klein, U., & Kohle, S. 1998, Astronomy and Astrophysics

Enß lin, T. A., Pfrommer, C., Springel, V., & Jubelgas, M. 2007, Astronomy and Astrophysics, 473, 41

Enß lin, T. A. & Roettgering, H. 2002, astro-ph/0209218

et al. Alexander Knebe. 2011, Monthly Notices of the Royal Astronomical Society, (in press)

Evrard, A. E., Bialek, J., Busha, M., White, M., Habib, S., Heitmann, K., Warren, M., Rasia, E., Tormen, G., Moscardini, L., Power, C., Jenkins, A. R., Gao, L., Frenk, C. S., Springel, V., White, S. D. M., & Diemand, J. 2008, Astrophys. J., 672, 122

Evrard, A. E., Metzler, C. A., & Navarro, J. F. 1996, Astrophys. J., 469, 494

Falceta-Gonçalves, D., Caproni, A., Abraham, Z., Teixeira, D. M., & de Gouveia Dal Pino, E. M. 2010a, The Astrophysical Journal, 713, L74

Falceta-Gonçalves, D., de Gouveia Dal Pino, E. M., Gallagher, J. S., & Lazarian, A. 2010b, The Astrophysical Journal, 708, L57

Fan, X. 2006, New Astronomy Reviews, 50, 665

Fender, R., Corbel, S., Tzioumis, T., McIntyre, V., Campbell-Wilson, D., Nowak, M., Sood, R., Hunstead, R., Harmon, A., Durouchoux, P., & Heindl, W. 1999, The Astrophysical Journal, 519, L165

Feretti, L., Brunetti, G., Giovannini, G., Kassim, N., Orrú, E., & Setti, G. 2004, Journal of Korean Astronomical Society, 37, 315

Feretti, L., Dallacasa, D., Giovannini, G., & Tagliani, A. 1995, Astronomy and Astrophysics, 302, 8

Feretti, L., Dallacasa, D., Govoni, F., Giovannini, G., Taylor, G. B., & Klein, U. 1999, Astronomy and Astrophysics

Ferrarese, L. 2002, Astrophys. J., 578, 90

Ferrari, C., Govoni, F., Schindler, S., Bykov, A. M., & Rephaeli, Y. 2008, Space Science Reviews, 134, 93

Frenk, C. S., White, S. D. M., Bode, P., Bond, J. R., Bryan, G. L., Cen, R., Couchman, H. M. P., Evrard, A. E., Gnedin, N., Jenkins, A., Khokhlov, A. M., Klypin, A., Navarro, J. F., Norman, M. L., Ostriker, J. P., Owen, J. M., Pearce, F. R., Pen, U., Steinmetz, M., Thomas, P. A., Villumsen, J. V., Wadsley, J. W., Warren, M. S., Xu, G., & Yepes, G. 1999, The Astrophysical Journal, 525, 554

Fryxell, B., Olson, K., Ricker, P., Timmes, F. X., Zingale, M., Lamb, D. Q., MacNeice, P., Rosner, R., Truran, J. W., & Tufo, H. 2000, Astrophys. J. Suppl., 131, 273

Fukushige, T. & Makino, J. 1997, The Astrophysical Journal, 477, L9

Furlanetto, S. R. & Loeb, A. 2001, The Astrophysical Journal, 556, 619

Gallo, E., Fender, R. P., & Pooley, G. G. 2003, Monthly Notices of the Royal Astronomical Society, 344, 60

Gardini, A. 2007, Astronomy and Astrophysics, 464, 143

Gaspari, M., Melioli, C., Brighenti, F., & D'Ercole, A. 2011, Monthly Notices of the Royal Astronomical Society, 411, 349

Giacintucci, S., Venturi, T., Macario, G., Dallacasa, D., Brunetti, G., Markevitch, M., Cassano, R., Bardelli, S., & Athreya, R. 2008, Astronomy and Astrophysics, 486, 347

Giovannini, G. 1999, New Astronomy, 4, 141

Giovannini, G., Bonafede, A., Feretti, L., Govoni, F., Murgia, M., Ferrari, F., & Monti, G. 2009, Astronomy and Astrophysics, 507, 1257

Giovannini, M. 2009, Physical Review D, 79

Gitti, M., Brunetti, G., & Setti, G. 2002, Astronomy and Astrophysics, 386, 456

Gnedin, N. Y., Ferrara, A., & Zweibel, E. G. 2000, The Astrophysical Journal, 539, 505

Gourgouliatos, K. N., Braithwaite, J., & Lyutikov, M. 2010, Monthly Notices of the Royal Astronomical Society, 409, 1660

Govoni, F., Markevitch, M., Vikhlinin, A., VanSpeybroeck, L., Feretti, L., & Giovannini, G. 2004, The Astrophysical Journal, 605, 695

Graham, A. W. 2007, Mon. Not. R. Astro. Soc., 379, 711

Grasso, D. & Rubinstein, H. 1995, Nuclear Physics B - Proceedings Supplements, 43, 303

Gu, M., Cao, X., & Jiang, D. R. 2009, Mon. Not. R. Astro. Soc., 396, 984

Gültekin, K., Richstone, D. O., Gebhardt, K., Lauer, T. R., Tremaine, S., Aller, M. C., Bender, R., Dressler, A., Faber, S. M., Filippenko, A. V., Green, R., Ho, L. C., Kormendy, J., Magorrian, J., Pinkney, J., & Siopis, C. 2009, Astrophys. J., 698, 198

Guth, A. H. 1981, Physical Review D, 23, 347

Hawley, J. & Stone, J. M. 1995, Computer Physics Communications, 89, 127

Heitmann, K., Lukić, Z., Fasel, P., Habib, S., Warren, M. S., White, M., Ahrens, J., Ankeny, L., Armstrong, R., O'Shea, B., Ricker, P. M., Springel, V., Stadel, J., & Trac, H. 2008, Computational Science & Discovery, 1, 015003

Heitmann, K., Ricker, P. M., Warren, M. S., & Habib, S. 2005, The Astrophysical Journal Supplement Series, 160, 28

Ho, L. 1999, Observational Evidence for the Black Holes in the Universe

Hockney, R. W. & Eastwood, J. W. 1988, Bristol: Hilger, 1988

Hopkins, P. F., Hernquist, L., Cox, T. J., Di Matteo, T., Martini, P., Robertson, B., & Springel, V. 2005a, Astrophys. J., 630, 705

—. 2005b, The Astrophysical Journal, 630, 705

Hopkins, P. F., Narayan, R., & Hernquist, L. 2006, The Astrophysical Journal, 643, 641

Hopkins, P. F., Younger, J. D., Hayward, C. C., Narayanan, D., & Hernquist, L. 2010, Mon. Not. R. Astro. Soc., 402, 1693

Huang, J. & Greengard, L. 2000, SIAM Journal of Scientific Computing, 21, 1551

Islam, R. R., Taylor, J. E., & Silk, J. 2004, Mon. Not. R. Astro. Soc., 354, 427

Jaffe, W. J. 1977, The Astrophysical Journal, 212, 1

Jarvis, M. J. 2007, At the Edge of the Universe: Latest Results from the Deepest Astronomical Surveys ASP Conference Series, 380

Jones, C. & Forman, W. 1984, The Astrophysical Journal, 276, 38

Jones, T. W. & De Young, D. S. 2005, The Astrophysical Journal, 624, 586

Kang, H., Ostriker, J. P., Cen, R., Ryu, D., Hernquist, L., Evrard, A. E., Bryan, G. L., & Norman, M. L. 1994, The Astrophysical Journal, 430, 83

Kapferer, W., Ferrari, C., Domainko, W., Mair, M., Kronberger, T., Schindler, S., Kimeswenger, S., van Kampen, E., Breitschwerdt, D., & Ruffert, M. 2006, Astronomy and Astrophysics, 447, 827

Kassim, N. E., Clarke, T. E., Cohen, A. S., Crane, P. C., Gaussiran, T., Gross, C., Henning, P. A., Hicks, B. C., Junor, W., Lane, W. M., Lazio, T. J. W., Paravastu, N., Pihlstrom, Y. M., Polisensky, E. J., Ray, P. S., Stewart, K. P., Taylor, G. B., & Weiler, K. W. 2006, Long Wavelength Astrophysics

Kempner, J. C., Blanton, E. L., Clarke, T. E., Enß lin, T. A., Johnston-Hollitt, M., & Rudnick, L. 2004, Proceedings of The Riddle of Cooling Flows in Galaxies and Clusters of Galaxies

Kempner, J. C. & Sarazin, C. L. 2001, The Astrophysical Journal, 548, 639

Keshet, U. & Loeb, A. 2010, The Astrophysical Journal, 722, 737

Khanna, R. & Camenzind, M. 1996, Astronomy and Astrophysics, 207, 665

Kim, W.-T. 2007, The Astrophysical Journal, 667, L5

King, A. R., Pringle, J. E., West, R. G., & Livio, M. 2004, Monthly Notices of the Royal Astronomical Society, 348, 111

King, E. J. & Coles, P. 2005, Monthly Notices of the Royal Astronomical Society, 365, 1288

Kirkpatrick, C. C., McNamara, B. R., & Cavagnolo, K. W. 2011, The Astrophysical Journal Letters (in press), 5

Kitayama, T. & Suto, Y. 1996, The Astrophysical Journal, 469, 480

Knebe, A., Knollmann, S. R., Muldrew, S. I., Pearce, F. R., Aragon-Calvo, M. A., Ascasibar, Y., Behroozi, P. S., Ceverino, D., Colombi, S., Diemand, J., Dolag, K., Falck, B. L., Fasel, P., Gardner, J., Gottloeber, S., Hsu, C.-H., Iannuzzi, F., Klypin, A., Lukic, Z., Maciejewski, M., McBride, C., Neyrinck, M. C., Planelles, S., Potter, D., Quilis, V., Rasera, Y., Read, J. I., Ricker, P. M., Roy, F., Springel, V., Stadel, J., Stinson, G., Sutter, P. M., Turchaninov, V., Tweed, D., Yepes, G., & Zemp, M. 2011, MNRAS (in press)

Koide, S., Shibata, K., & Kudoh, T. 1999, The Astrophysical Journal, 522, 727

Kollmeier, J. A., Onken, C. A., Kochanek, C. S., Gould, A., Weinberg, D. H., Dietrich, M., Cool, R., Dey, A., Eisenstein, D. J., Jannuzi, B. T., Le Floch, E., & Stern, D. 2006, The Astrophysical Journal, 648, 128

Komatsu, E., Smith, K. M., Dunkley, J., Bennett, C. L., Gold, B., Hinshaw, G., Jarosik, N., Larson, D., Nolta, M. R., Page, L., Spergel, D. N., Halpern, M., Hill, R. S., Kogut, A., Limon, M., Meyer, S. S., Odegard, N., Tucker, G. S., Weiland, J. L., Wollack, E., & Wright, E. L. 2011, The Astrophysical Journal Supplement Series, 192, 18

Koushiappas, S. M., Bullock, J. S., & Dekel, A. 2004, Mon. Not. R. Astro. Soc., 354, 292

Krause, M., Alexander, P., Bolton, R., Geisbsch, J., Green, D. A., & Riley, J. 2009, Monthly Notices of the Royal Astronomical Society, 400, 646

Kuchar, P. & Enß lin, T. A. 2011, Astronomy & Astrophysics, 529, A13

Kulsrud, R. M., Cen, R., Ostriker, J. P., & Ryu, D. 1997, The Astrophysical Journal, 480, 481

Kulsrud, R. M. & Zweibel, E. G. 2008, Reports on Progress in Physics, 71, 046901

Kuo, P.-H., Hwang, C.-Y., & Ip, W.-H. 2003, astro-ph/0312226

Langer, M., Aghanim, N., & Puget, J.-L. 2005, Astronomy and Astrophysics, 443, 367

Large, M. I., Mathewson, D. S., & Haslam, C. G. T. 1959, Nature, 183, 1663

Lee, D. 2006, Thesis (Ph.D.)–University of Maryland

LEE, D. & DEANE, A. 2009, Journal of Computational Physics, 228, 952

Lesch, H. & Birk, G. T. 1998, Physics of Plasmas, 5, 2773

Li, H., Lapenta, G., Finn, J. M., Li, S., & Colgate, S. A. 2006, The Astrophysical Journal, 643, 92

Liang, H., Hunstead, R. W., Birkinshaw, M., & Andreani, P. 2000, The Astrophysical Journal, 544, 686

Linde, A. 1982, Physics Letters B, 108, 389

Liu, W., Hsu, S. C., Li, H., Li, S., & Lynn, A. G. 2008a, Physics of Plasmas, 15, 072905

Liu, W., Li, H., Li, S., & Hsu, S. C. 2008b, The Astrophysical Journal, 684, L57

Lohner, R. 1987, Comp. Meth. App. Mech. Eng., 61, 323

Lucy, L. B. 1977, The Astronomical Journal, 82, 1013

Lukić, Z., Heitmann, K., Habib, S., Bashinsky, S., & Ricker, P. M. 2007, Astrophys. J., 671, 1160

Lukić, Z., Reed, D., Habib, S., & Heitmann, K. 2009, Astrophys. J., 692, 217

MacNeice, P., Olson, K., Mobarry, C., de Fainchtein, R., & Packer, C. 2000, CPC, 126, 330

Madau, P. & Rees, M. J. 2001, The Astrophysical Journal, 551, L27

Magorrian, J., Tremaine, S., Richstone, D., Bender, R., Bower, G., Dressler, A., Faber, S. M., Gebhardt, K., Green, R., Grillmair, C., Kormendy, J., & Lauer, T. 1998, Astro. J., 115, 2285

Mayer, L., Kazantzidis, S., Madau, P., Colpi, M., Quinn, T., & Wadsley, J. 2007, Science (New York, N.Y.), 316, 1874

McNamara, B. & Nulsen, P. 2007, Annual Review of Astronomy and Astrophysics, 45, 117

McNamara, B. R., Wise, M., Nulsen, P. E. J., David, L. P., Sarazin, C. L., Bautz, M., Markevitch, M., Vikhlinin, A., Forman, W. R., Jones, C., & Harris, D. E. 2000, The Astrophysical Journal, 534, L135

Medvedev, M. V., Silva, L. O., & Kamionkowski, M. 2006, The Astrophysical Journal, 642, L1

Menou, K., Haiman, Z., & Narayanan, V. K. 2001, Astrophys. J., 558, 535

Merloni, A., Bongiorno, A., Bolzonella, M., Brusa, M., Civano, F., Comastri, A., Elvis, M., Fiore, F., Gilli, R., Hao, H., Jahnke, K., Koekemoer, A. M., Lusso, E., Mainieri, V., Mignoli, M., Miyaji, T., Renzini, A., Salvato, M., Silverman, J., Trump, J., Vignali, C., Zamorani, G., Capak, P., Lilly, S. J., Sanders, D., Taniguchi, Y., Bardelli, S., Carollo, C. M., Caputi, K., Contini, T., Coppa, G., Cucciati, O., de la Torre, S., de Ravel, L., Franzetti, P., Garilli, B., Hasinger, G., Impey, C., Iovino, A., Iwasawa, K., Kampczyk, P., Kneib,

J. P., Knobel, C., Kova\v c, K., Lamareille, F., Le Borgne, J. F., Le Brun, V., Le Fèvre, O., Maier, C., Pello, R., Peng, Y., Perez Montero, E., Ricciardelli, E., Scodeggio, M., Tanaka, M., Tasca, L. A. M., Tresse, L., Vergani, D., & Zucca, E. 2010, Astrophys. J., 708, 137

Merritt, D. & Ferrarese, L. 2001, in Astronomical Society of the Pacific Conference Series, Vol. 249, The Central Kiloparsec of Starbursts and AGN: The La Palma Connection, ASP Conference Proceedings Vol. 249. Edited by J. H. Knapen, J. E. Beckman, I. Shlosman, and T. J. Mahoney., ed. J. E. B. J. H. Knapen, 335–+

Merritt, D. & Milosavljević, M. 2005, Living Reviews in Relativity, 8, 8

Micic, M., Holley-Bockelmann, K., & Sigurdsson, S. 2008, 0805.3154

Micic, M., Holley-Bockelmann, K., Sigurdsson, S., & Abel, T. 2007, Mon. Not. R. Astro. Soc., 380, 1533

Mikellides, I. G., Tassis, K., & Yorke, H. W. 2011, Monthly Notices of the Royal Astronomical Society, 410, 2602

Miniati, F. 2003, Monthly Notices of the Royal Astronomical Society, 342, 1009

Miniati, F., Jones, T. W., Kang, H., & Ryu, D. 2001, The Astrophysical Journal, 562, 233

Mitchell, N. L., McCarthy, I. G., Bower, R. G., Theuns, T., & Crain, R. A. 2009, Monthly Notices of the Royal Astronomical Society, 395, 180

Mittal, R., Hudson, D. S., Reiprich, T. H., & Clarke, T. 2009, Astronomy and Astrophysics, 501, 835

Moore, B., Ghigna, S., Governato, F., Lake, G., Quinn, T., Stadel, J., & Tozzi, P. 1999, The Astrophysical Journal, 524, L19

Morsony, B. J., Heinz, S., Brüggen, M., & Ruszkowski, M. 2010, Monthly Notices of the Royal Astronomical Society, 407, 1277

Narayan, R. & Medvedev, M. V. 2001, The Astrophysical Journal, 562, L129

Navarro, J. F., Frenk, C. S., & White, S. D. M. 1996, The Astrophysical Journal, 462, 563

Osterbrock, D. 1989, Research supported by the University of California

Parrish, I. J., Quataert, E., & Sharma, P. 2009, The Astrophysical Journal, 703, 96

Paul, S., Iapichino, L., Miniati, F., Bagchi, J., & Mannheim, K. 2011, The Astrophysical Journal, 726, 17

Peacock, J. A. 1999, Cosmological Physics

Peebles, P. J. E. 1993, Principles of Physical Cosmology by P.J.E. Peebles. Princeton University Press

Percival, W. J., Baugh, C. M., Bland-Hawthorn, J., Bridges, T., Cannon, R., Cole, S., Colless, M., Collins, C., Couch, W., Dalton, G., De Propris, R., Driver, S. P., Efstathiou, G., Ellis, R. S., Frenk, C. S., Glazebrook, K., Jackson, C., Lahav, O., Lewis, I., Lumsden, S., Maddox, S., Moody, S., Norberg, P., Peacock, J. A., Peterson, B. A., Sutherland, W., & Taylor, K. 2001, Monthly Notices of the Royal Astronomical Society, 327, 1297

Perley, R. A., Dreher, J. W., & Cowan, J. J. 1984, The Astrophysical Journal, 285, L35

Perlmutter, S., Aldering, G., Goldhaber, G., Knop, R. A., Nugent, P., Castro, P. G., Deustua, S., Fabbro, S., Goobar, A., Groom, D. E., Hook, I. M., Kim, A. G., Kim, M. Y., Lee, J. C., Nunes, N. J., Pain, R., Pennypacker, C. R., Quimby, R., Lidman, C., Ellis, R. S., Irwin, M., McMahon, R. G., RuizLapuente, P., Walton, N., Schaefer, B., Boyle, B. J., Filippenko, A. V., Matheson, T., Fruchter, A. S., Panagia, N., Newberg, H. J. M., Couch, W. J., & Project, T. S. C. 1999, The Astrophysical Journal, 517, 565

Peterson, J. & Fabian, A. 2006, Physics Reports, 427, 1

Peterson, J. R., Kahn, S. M., Paerels, F. B. S., Kaastra, J. S., Tamura, T., Bleeker, J. A. M., Ferrigno, C., & Jernigan, J. G. 2003, The Astrophysical Journal, 590, 207

Petrosian, V. 2001, The Astrophysical Journal, 557, 560

Pfrommer, C. & Enß lin, T. A. 2004, Monthly Notices of the Royal Astronomical Society, 352, 76

Pfrommer, C., Enß lin, T. A., & Springel, V. 2008, Monthly Notices of the Royal Astronomical Society, 385, 1211

Pfrommer, C., Enß lin, T. A., Springel, V., Jubelgas, M., & Dolag, K. 2007, Monthly Notices of the Royal Astronomical Society, 378, 385

Pope, E. C. D. 2007, Monthly Notices of the Royal Astronomical Society, 381, 741

Powell, K. 1999, Journal of Computational Physics, 154, 284

Press, W. H. & Schechter, P. 1974, The Astrophysical Journal, 187, 425

Ratkiewicz, R., Axford, W. I., & McKenzie, J. F. 1994, Astronomy and Astrophysics (ISSN 0004-6361), 291, 935

Rees, M. J. 1987, Royal Astronomical Society, 28, 197

Reiprich, T. & Boehringer, H. 2002, ApJ, 567, 716

Ricker, P. M. 2008, The Astrophysical Journal Supplement Series, 176, 293

Ricker, P. M. & Sarazin, C. L. 2001, The Astrophysical Journal, 561, 621

Riess, A. G., Filippenko, A. V., Challis, P., Clocchiatti, A., Diercks, A., Garnavich, P. M., Gilliland, R. L., Hogan, C. J., Jha, S., Kirshner, R. P., Leibundgut, B., Phillips, M. M., Reiss, D., Schmidt, B. P., Schommer, R. A., Smith, R. C., Spyromilio, J., Stubbs, C., Suntzeff, N. B., & Tonry, J. 1998, The Astronomical Journal, 116, 1009

Ritchie, B. W. & Thomas, P. A. 2002, Monthly Notices of the Royal Astronomical Society, 329, 675

Ritchmyer, R. D. & Morton, K. W. 1967, Interscience Tracts in Pure and Applied Mathematics, New York: Interscience, 1967, 2nd ed., -

Robinson, K., Dursi, L. J., Ricker, P. M., Rosner, R., Calder, A. C., Zingale, M., Truran, J. W., Linde, T., Caceres, A., Fryxell, B., Olson, K., Riley, K., Siegel, A., & Vladimirova, N. 2004, The Astrophysical Journal, 601, 621

Roettiger, K., Stone, J. M., & Burns, J. O. 1999, The Astrophysical Journal, 518, 594

Rottgering, H. 2003, New Astronomy Reviews, 47, 405

Rottgering, H. J. A., Braun, R., Barthel, P. D., van Haarlem, M. P., Miley, G. K., Morganti, R., Snellen, I., Falcke, H., de Bruyn, A. G., Stappers, R. B., Boland, W. H. W. M., Butcher, H. R., de Geus, E. J., Koopmans, L., Fender, R., Kuijpers, J., Schilizzi, R. T., Vogt, C., Wijers, R. A. M. J., Wise, M., Brouw, W. N., Hamaker, J. P., Noordam, J. E., Oosterloo, T., Bahren, L., Brentjens, M. A., Wijnholds, S. J., Bregman, J. D., van Cappellen, W. A., Gunst, A. W., Kant, G. W., Reitsma, J., van der Schaaf, K., & de Vos, C. M. 2006, eprint arXiv:astro-ph/0610596

Russell, H. R., van Weeren, R. J., Edge, A. C., McNamara, B. R., Sanders, J. S., Fabian, A. C., Baum, S. A., Canning, R. E. A., Donahue, M., & O'Dea, C. P. 2011

Ruszkowski, M., En\sslin, T. A., Brüggen, M., Heinz, S., & Pfrommer, C. 2007, Mon. Not. R. Astro. Soc., 378, 662

Ruszkowski, M., Lee, D., Bruggen, M., Parrish, I., & Oh, S. P. 2010, The Astrophysical Journal (submitted)

Ruszkowski, M. & Oh, S. P. 2010, Monthly Notices of the Royal Astronomical Society (submitted)

Ruzmaikin, A., Sokolov, D., & Shukurov, A. 1989, Royal Astronomical Society, 241, 1

Ryu, D., Kang, H., & Biermann, P. L. 1998, Astronomy and Astrophysics

Ryu, D., Kang, H., Hallman, E., & Jones, T. W. 2003, The Astrophysical Journal, 593, 599

Ryu, D., Ostriker, J. P., Kang, H., & Cen, R. 1993, The Astrophysical Journal, 414, 1

Sarazin, C. L. 1988, Cambridge Astrophysics Series

Schindler, S., Kapferer, W., Domainko, W., Mair, M., van Kampen, E., Kronberger, T., Kimeswenger, S., Ruffert, M., Mangete, O., & Breitschwerdt, D. 2005, Astronomy and Astrophysics, 435, L25

Schlickeiser, R., Sievers, A., & Thiemann, H. 1987, Astronomy and Astrophysics (ISSN 0004-6361), 182, 21

Scoville, N., Abraham, R. G., Aussel, H., Barnes, J. E., Benson, A., Blain, A. W., Calzetti, D., Comastri, A., Capak, P., Carilli, C., Carlstrom, J. E., Carollo, C. M., Colbert, J., Daddi, E., Ellis, R. S., Elvis, M., Ewald, S. P., Fall, M., Franceschini, A., Giavalisco, M., Green, W., Griffiths, R. E., Guzzo, L., Hasinger, G., Impey, C., Kneib, J., Koda, J., Koekemoer, A., Lefevre, O., Lilly, S., Liu, C. T., McCracken, H. J., Massey, R., Mellier, Y., Miyazaki, S., Mobasher, B., Mould, J., Norman, C., Refregier, A., Renzini, A., Rhodes, J., Rich, M., Sanders, D. B., Schiminovich, D., Schinnerer, E., Scodeggio, M., Sheth, K., Shopbell, P. L., Taniguchi, Y., Tyson, N. D., Urry, C. M., Van Waerbeke, L., Vettolani, P., White, S. D. M., & Yan, L. 2007, The Astrophysical Journal Supplement Series, 172, 38

Seljak, U. & Zaldarriaga, M. 1996, The Astrophysical Journal, 469, 437

Sesana, A., Haardt, F., Madau, P., & Volonteri, M. 2004, Astrophys. J., 611, 623

Shankar, F. 2009, New Astronomy Reviews, 53, 57

Shankar, F., Salucci, P., Granato, G. L., De Zotti, G., & Danese, L. 2004, Mon. Not. R. Astro. Soc., 354, 1020

Shukurov, A., Subramanian, K., & Haugen, N. E. L. 2006, Astronomische Nachrichten, 327, 583

Sijacki, D., Springel, V., Di Matteo, T., & Hernquist, L. 2007, Monthly Notices of the Royal Astronomical Society, 380, 877

Simard-Normandin, M., Kronberg, P. P., & Button, S. 1981, The Astrophysical Journal Supplement Series, 45, 97

Skillman, S. W., OShea, B. W., Hallman, E. J., Burns, J. O., & Norman, M. L. 2008, The Astrophysical Journal, 689, 1063

Somerville, R. S., Hopkins, P. F., Cox, T. J., Robertson, B. E., & Hernquist, L. 2008, Monthly Notices of the Royal Astronomical Society, 391, 481

Stanek, R., Rasia, E., Evrard, A. E., Pearce, F., & Gazzola, L. 2010, The Astrophysical Journal, 715, 1508

Sternberg, A., Pizzolato, F., & Soker, N. 2007, The Astrophysical Journal, 656, L5

Subramanian, K., Shukurov, A., & Haugen, N. E. L. 2006, Monthly Notices of the Royal Astronomical Society, 366, 060119013534002

Sutherland, R. S. & Dopita, M. A. 1993, The Astrophysical Journal Supplement Series, 88, 253

Sutter, P. M. & Ricker, P. M. 2010, The Astrophysical Journal, 723, 1308

Sutter, P. M., Ricker, P. M., & Yang, H.-Y. 2011a, The Astrophysical Journal (submitted)

Sutter, P. M., Yang, H.-Y., Ricker, P. M., Foreman, G., & Pugmire, D. 2011b, The Astrophysical Journal (submitted)

Takizawa, M. 2008, The Astrophysical Journal, 687, 951

Taylor, G. B. & Perley, R. A. 1993, The Astrophysical Journal, 416, 554

Teyssier, R. 2002, Astronomy and Astrophysics, 385, 337

Treister, E., Natarajan, P., Sanders, D. B., Urry, C. M., Schawinski, K., & Kartaltepe, J. 2010, Science (New York, N.Y.), 328, 600

Tremaine, S., Gebhardt, K., Bender, R., Bower, G., Dressler, A., Faber, S. M., Filippenko, A. V., Green, R., Grillmair, C., Ho, L. C., Kormendy, J., Lauer, T. R., Magorrian, J., Pinkney, J., & Richstone, D. 2002, The Astrophysical Journal, 574, 740

Trottenberg, U., Oosterlee, C. W., & Schuller, A. 2000, Multigrid (London: Academic Press)

Tsagas, C. G. 2009, Plasma Physics and Controlled Fusion, 51, 124013

Umetsu, K., Broadhurst, T., Zitrin, A., Medezinski, E., & Hsu, L.-Y. 2011, The Astrophysical Journal, 729, 127

van Weeren, R. J., Hoeft, M., Rottgering, H. J. A., Bruggen, M., Intema, H. T., & van Velzen, S. 2011, The Astronomical Journal, 13

Vazza, F., Brunetti, G., Gheller, C., Brunino, R., & Brüggen, M. 2010, eprint arXiv:1010.5950

Venturi, T., INAF, & di Radioastronomia, I. 2011, 8

Vernaleo, J. C. & Reynolds, C. S. 2006, Astrophys. J., 645, 83

Vikhlinin, A., Burenin, R. A., Ebeling, H., Forman, W. R., Hornstrup, A., Jones, C., Kravtsov, A. V., Murray, S. S., Nagai, D., Quintana, H., & Voevodkin, A. 2009, The Astrophysical Journal, 692, 1033

Voit, G. 2005, Reviews of Modern Physics, 77, 207

Voit, G. M. & Donahue, M. 2005, The Astrophysical Journal, 634, 955

Volonteri, M., Haardt, F., & Madau, P. 2003, Astrophys. J., 582, 559

Volonteri, M., Lodato, G., & Natarajan, P. 2008, Mon. Not. R. Astro. Soc., 383, 1079

Warren, M. S., Abazajian, K., Holz, D. E., & Teodoro, L. 2006, Astrophys. J., 646, 881

Weisskopf, M. C., Brinkman, B., Canizares, C., Garmire, G., Murray, S., & Van Speybroeck, L. P. 2002, Publications of the Astronomical Society of the Pacific, 114, 1

White, M. 2002, Astrophys. J. Suppl., 143, 241

Widrow, L. 2002, Reviews of Modern Physics, 74, 775

Wise, J. H. & Abel, T. 2005, Astrophys. J., 629, 615

Xu, H., Li, H., Collins, D., Li, S., & Norman, M. L. 2008a, The Astrophysical Journal, 681, L61

Xu, H., Li, H., Collins, D. C., Li, S., & Norman, M. L. 2009, The Astrophysical Journal, 698, L14

—. 2010, The Astrophysical Journal, 725, 2152

Xu, H., O'Shea, B. W., Collins, D. C., Norman, M. L., Li, H., & Li, S. 2008b, The Astrophysical Journal, 688, L57

Yang, H.-Y., Sutter, P., & Ricker, P. 2011, The Astrophysical Journal (submitted)

Zel'Dovich, Y. B. 1970, Astron. Astrophys., 5

Zhang, Q.-C., Wang, Z., & Chen, Y. 1996, The Astrophysical Journal, 466, 808

ZuHone, J. A., Markevitch, M., & Johnson, R. E. 2010, The Astrophysical Journal, 717, 908

Zweibel, E. G. 1988, The Astrophysical Journal, 329, L1

Zwicky, F. 1933, Helvetica Physica Acta, 6, 110